UC San Diego

UC San Diego Electronic Theses and Dissertations

Title

A Duality-based Cosserat Crystal Plasticity and Neural Network Enriched Phase Field for Modeling Grain Refinement

Permalink

https://escholarship.org/uc/item/8b2200x1

Author

Baek, Jonghyuk

Publication Date

2021

Peer reviewed|Thesis/dissertation

eScholarship.org Powered by the California Digital Library
University of California

UNIVERSITY OF CALIFORNIA SAN DIEGO

A Duality-based Cosserat Crystal Plasticity and Neural Network Enriched Phase Field for Modeling Grain Refinement

A Dissertation submitted in partial satisfaction of the requirements
for the degree of Doctor of Philosophy

in

Structural Engineering

by

Jonghyuk Baek

Committee in charge:

Professor Jiun-Shyan Chen, Chair
Professor Shengqiang Cai
Professor Gilbert A. Hegemier
Professor Marc Andre Meyers
Professor Shabnam J. Semnani

2021

Copyright

Jonghyuk Baek, 2021

All rights reserved.

The dissertation of Jonghyuk Baek is approved, and it is acceptable in quality and form for publication on microfilm and electronically.

University of California San Diego

2021

DEDICATION

To my family

TABLE OF CONTENTS

LIST OF FIGURES

LIST OF TABLES

ACKNOWLEGEMENTS

First, I would like to thank Professor J. S. Chen for his advice, insights, support, and encouragement he gave me. He never loses his passion for research and education, having me keep going. He is an inspiring person, having me keep thinking. I am happy that I have grown a lot as an independent researcher in his group.

I would also like to thank my defense and candidacy committee members Professor Shengqiang Cai, Professor Gilbert Hegemier, Professor Marc Meyers, Professor Shabnam Semnani, and Professor Petr Krysl for their insightful questions and valuable suggestions that have added depth to my research.

I want to deliver many thanks to my colleagues and friends. To Dr. Kevin Arnett, it was my great pleasure to have my early years at UCSD with you working together on the explosive welding project and getting to know you and your family personally. To Dr. Marco Pasetto, I will never forget the moments of TA-ing SE 276B and writing a paper with you. I learned a lot from these moments. Also, the friendship and support from you are really appreciated. To Dr. Haoyan Wei, thank you for the help you gave me when I just joined our group and learned meshfree. I enjoyed many discussions with you. To Prof. Alex Huang, thanks for being a great colleague from the beginning of my years at UCSD. To Xiaolong He and Karan Taneja, I very much enjoyed having a coffee break with you guys and thanks for leading me to the world of machine learning. Another big portion of thanks should go to Dr. Jake Koester, Dr. Frank Beckwith, Prof. Qizhi He, Prof. Shigeki Kaneko, Dr. Guohua Zhou, Ryan Schlinkman, Kristen Susuki, Hooseok Lee, Dr.

Hanjoo Lee, Dr. Rodrigo Chavez Morales, Dr. Mat Reynolds, Prof. Mike Hillman, Dr. Mike Tupek, and many others.

I truly thank my dad, mom, sister, father-in-law, mother-in-law, and brother-in-law. I will never forget the love and support they constantly showed me.

Lastly but most importantly, I love you, Youngeun. I love all the moments I have had with you. Thank you so much for going through each other's tough journey together.

The support by Sandia National Laboratories and National Science Foundation is greatly appreciated.

A portion of Chapter 1 has been published in Baek, J., Chen, J. S., Zhou, G., Arnett, K., Hillman, M., Hegemier., G., & Hardesty, S. (2021) "A semi-Lagrangian reproducing kernel particle method with particle-based shock algorithm for explosive welding simulation". Computational Mechanics, 67,1601-1627. The dissertation author was the primary investigator of this material.

A portion of Chapters 2-6, 8-9 has been accepted for publication in Baek, J., Chen, J. S., Tupek, M., Beckwith, F., & Fang, H. E. "A Duality-based Coupling of Cosserat Crystal Plasticity and Phase Field Theories for Modeling Grain Refinement", International Journal for Numerical Methods in Engineering. The dissertation author was the primary investigator of this material.

A portion of Chapters 7 and 9 is currently being prepared for submission for publication in Baek, J., Chen, J. S., & Susuki, K. "Neural Network-enhanced Reproducing Kernel Particle Method for Modeling Localizations". The dissertation author was the primary investigator of this material.

A portion of Chapters 7, 8, and 9 is currently being prepared for submission for publication in Baek, J. & Chen, J. S. “Neural Network-enhanced Reproducing Kernel Particle Method for Modeling Grain Refinement”. The dissertation author was the primary investigator of this material.

VITA

2021	Ph.D. in Structural Engineering, University of California San Diego
2010-2014	Instructor in Civil Engineering, Korea Military Academy
2010	M.S. in Civil and Environmental Engineering, Seoul National University
2008	B.S. in Civil and Environmental Engineering, Seoul National University

PUBLICATIONS

JOURNAL ARTICLES

- Baek, J., Chen, J. S., Tupek, M., Beckwith, F., & Fang, H. E. (2021) A Duality-based Coupling of Cosserat Crystal Plasticity and Phase Field Theories for Modeling Grain Refinement, International Journal for Numerical Methods in Engineering (Accepted). https://doi.org/10.1002/nme.6884

- Morales, R. C., Baek, J., Sharp, D., Aderounmu, A., Wei, H., Chen, J. S., & Eliasson, V. (2021) Mode-II Fracture Response of PMMA Under Dynamic Loading Conditions, Journal of Dynamic Behavior of Materials. Advance online publication. https://doi.org/10.1007/s40870-021-00320-9

- Baek, J., Chen, J. S., Zhou, G., Arnett, K., Hillman, M., Hegemier., G., & Hardesty, S. (2021) A semi-Lagrangian reproducing kernel particle method with particle-based shock algorithm for explosive welding simulation. Computational Mechanics, 67,1601-1627. https://doi.org/10.1007/s00466-021-02008-2

- Pasetto, M., Baek, J., Chen, J. S., Wei, H., Sherburn, J. A., & Roth, M. J. (2021) A Lagrangian/semi-Lagrangian Coupling Approach for Meshfree Modeling of Extremely Large Deformation Problems. Computer Methods in Applied Mechanics and Engineering, 381, 113827. https://doi.org/10.1016/j.cma.2021.113827

- Wei, H., Chen, J. S., Beckwith, F., & Baek, J. (2020). A naturally stabilized semi-Lagrangian meshfree formulation for multiphase porous media with application to landslide modeling. Journal of Engineering Mechanics, 146(4), 04020012. https://doi.org/10.1061/(ASCE)EM.1943-7889.0001729

- Park, Y. J., Baek, J., & Son, K. (2016). A Study on the Calculation of the Design Loads for Blast Doors of Underground Ammunition Facilities Using M&S. Journal of the Korea Institute of Military Science and Technology, 19(3), 302-310. https://doi.org/10.9766/KIMST.2016.19.3.302

- Park, J. K., Lim, C. W., Ryu, D. W., Son, K. Y., Baek, J. H., & Park, Y. J. (2014). The design and protective capacity assessment of the prefabricated PC arch ammo magazines. Journal of the Korea Institute of Building Construction, 14(6), 615-621. https://doi.org/10.5345/JKIBC.2014.14.6.615

- Baek, J., Kim, S. B., Son, K., & Park, Y. J. (2014). The study on assessment of protective capacity of the reinforced concrete box-type artillery positions. Journal of the Korea Institute of Military Science and Technology, 17(2), 275-281. https://doi.org/10.9766/KIMST.2014.17.2.275

PROCEEDINGS

- Reedlunn, B., Moutsanidis, G., Baek, J., Huang, T., Koester, J., He, X., Wei, H., Taneja, K., Bazilevs, Y., & Chen, J. S. (2020, June) Initial Simulations of Empty Room Collapse and Reconsolidation at the Waste Isolation Pilot Plant. In 54th U.S. Rock Mechanics/Geomechanics Symposium, physical event cancelled.

- Chen, J. S., Baek, J., Huang, T. H., & Hillman, M. C. (2020, April). Accelerated and Stabilized Meshfree Method for Impact-Blast Modeling. In Structures Congress 2020 (pp. 92-104). Reston, VA: American Society of Civil Engineers.

ABASTRACT OF THE DISSERTATION

A Duality-based Cosserat Crystal Plasticity and Neural Network Enriched Phase Field for Modeling Grain Refinement

by

Jonghyuk Baek

Doctor of Philosophy in Structural Engineering

University of California, San Diego, 2021

Professor Jiun-Shyan Chen, Chair

High-rate deformation processes of metals such as explosive welding and cold spray additive manufacturing entail intense grain refinement. The multi-field variational formulation and the associated computational method capable of modeling the evolution of microstructures with sharp solution transition near the grain boundaries remain challenging in achieving high accuracy, stability, and computational efficiency. In this work, a new computational formulation for coupling Cosserat crystal plasticity and phase field is developed. The conventional approach by penalizing the kinematic incompatibility between lattice orientation and displacement-based elastic rotation leads to significant solution sensitivity to the penalty parameter, resulting in low accuracy and convergence rates. To address these issues, a duality-based formulation is developed under a multi-

field variational framework. The associated Galerkin formulation incorporated with a weak inf-sup-based skew-symmetric stress projection is introduced to ensure coercivity for stability in the dual formulation. An additional least squares stabilization is introduced to suppress the spurious lattice rotation with a suitable parameter range derived analytically and validated numerically. It is shown that under this formulation, the equal order displacement-rotation-phase field approximations are stable, which allows efficient construction of approximation functions for all independent variables. The proposed formulation is shown to yield superior accuracy and convergence with marginal parameter sensitivity compared to the conventional penalty-based approach and successfully captures the dominant rotational recrystallization mechanisms that exist in the block dislocation structures and grain boundary migration.

Modeling the sharp transition in the phase field near the grain boundaries associated with the lattice orientation often requires highly refined discretization for sufficient accuracy, which significantly increases the computational cost. While adaptive model refinement can be employed for enhanced effectiveness, it is cumbersome for the traditional mesh-based methods to perform adaptive model refinement. In this work, neural network-enhanced reproducing kernel particle method (NN-RKPM) is proposed, where the location, orientation, and the shape of the solution transition is automatically captured by the NN approximation by the minimization of total potential energy. The standard RK approximation is then utilized to approximate the smooth part of the solution to permit a much coarser discretization than the high-resolution discretization needed to capture sharp solution transition with the conventional methods. The proposed NN-RKPM is first verified by solving the standard damage evolution problems. The proposed computational framework is then applied to modeling grain refinement mechanisms, including the migration of grain boundaries at a triple junction, for validating the effectiveness of the proposed methods.

Chapter 1

Introduction

1.1. Motivation

High strain rate deformation processes of metals, such as cold spray additive manufacturing and explosive welding, entail intense grain refinement as well as extreme deformation and fragmentation. The latter phenomena are presented in the form of interfacial wave and jetting [1–8] observed in macro scale. While these macro-scale phenomena are challenging for traditional mesh-based approaches to capture [9, 10], meshfree methods has been proven to effective in the prediction of both jetting and interfacial wave in recent studies [11–15]. Baek et al. (2021) [11] addressed the difficulties in accurate modeling of strong shock, extreme deformation, and material separation by introducing node-based shock algorithm and adaptive integration domain adjustment technique into semi-Lagrangian reproducing kernel particle method [16–18], and accurately predicted the explosion and impact-induced shock, gradual evolution of interfacial wave, morphology of interfacial wave, and jetting (Figure 1.1). In [15], expected material phase states were indirectly predicted and the traditional welding windows were evaluated based on macro-scale numerical observations using combined meshfree and finite difference simulations.

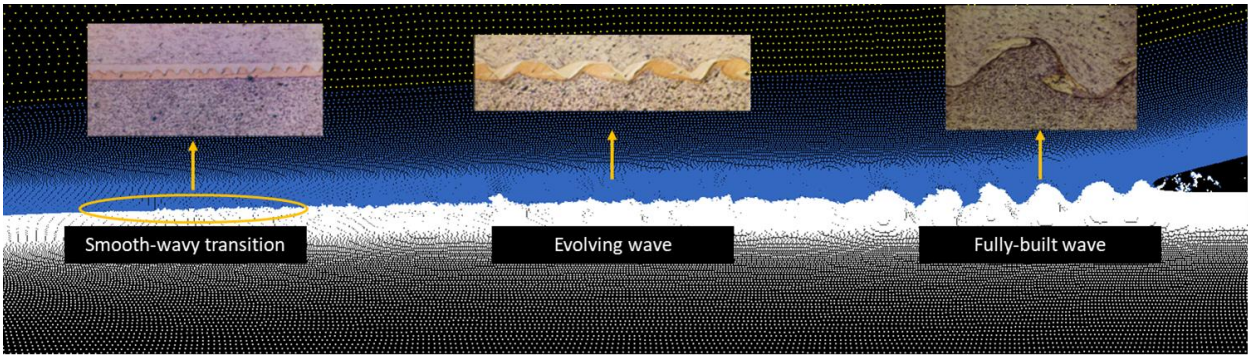

(a) Metal jet and gradually built interfacial wave

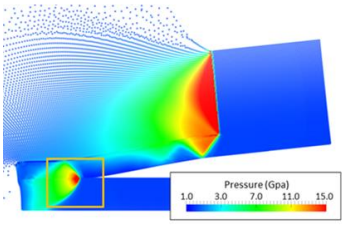

(b) Pressure field

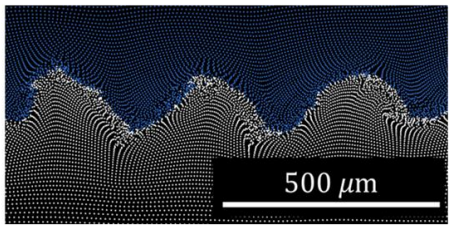

(c) Interfacial wave (numerical)

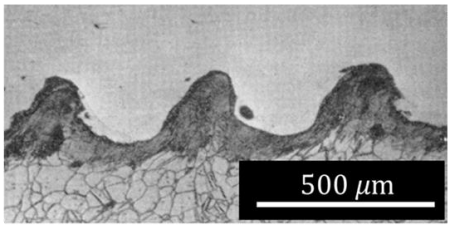

(d) Interfacial wave (experiment, Bahrani et al., 1964)

Figure 1.1. Numerical prediction of explosive welding (Baek el al., 2021): (a) gradually-built interfacial wave compared to an experimental result [5], (b) strong shock produced by explosion and plate impact, (c) interfacial wave captured by the numerical simulation, and (d) the corresponding experimental result [4]

Although these research works provide valuable findings at the macro scale, it remains unresolved in establishing the linkage among the process parameters, microstructure evolution, and resulting material properties due to the high degree of microstructural evolution caused by the high rate manufacturing processes, particularly, the intense grain refinement observed in a large volume of experimental studies [19–24]. Meyers et al. [25, 26] proposed the rotational recrystallization mechanism that explains the grain refinement induced by extreme shear localization under high strain rate. This mechanism is supported by experimental works [27, 28] on the cold spray technique.

Numerical modeling of the aforementioned recrystallization mechanism is challenging as it entails extreme material deformations, nonlocal effects of GNDs, discontinuities in lattice orientation (localizations of lattice curvature), and moving grain boundaries. The multi-field variational formulation and the associated computational method capable of modeling the evolution of microstructures with sharp solution transition near the grain boundaries remain challenging in achieving high accuracy, stability, and computational efficiency. While numerical modeling in very small length scales such as atomic scale and dislocation scale can be considered, it is computationally intractable despite of its predictive capability. Mesoscale approaches such as crystal plasticity treat dislocations with a continuous dislocation density field and describe the anisotropic viscoplastic deformations by considering plastic slips and applied shear stresses on individual slip systems. However, the nonlocal effects associated with GNDs has limitations on local continuum models. As a remedy, the strain gradient-typed crystal plasticity introduces nonlocal effects by including additional plastic slip degrees of freedom on all slip system but requires increased computational costs. The Cosserat crystal plasticity reduces the number of degrees freedom by corelating GND with the lattice curvature. In Cosserat crystal plasticity, lattice rotations are introduced as independent variables, which is computationally less extensive than strain gradient-typed formulations due to fewer additional degrees of freedom. However, when penalty method is used to corelate elastic rotation with the lattice curvature, solution sensitivity to the penalty parameter can be an issue in the widely used penalty-based Cosserat crystal plasticity.

Moreover, the modeling of grain boundary migration brings additional challenges related to correct representation of grain boundary energy, discretization sensitivity, and coupling with crystal plasticity. In general, if the discretization sensitivity is not properly addressed for a problem involving localization, numerical results including energy, force, and localization patterns can be

strongly mesh-dependent due to the loss of ellipticity in the mathematical formulation. For example, the grain growth kinetics tends to be strongly influenced by the resolution and shape of grid in cellular automation. The phase field methods are regularization techniques where the discontinuous fields are approximated by the diffusive phase fields, and the coupling of the phase field and other degrees of freedom is attained in the free energy. The length scales introduced in the phase field methods serve as localization limiters. In the widely used multi-phase field method, multiple phase fields are introduced and each phase is associated with a specific grain orientation, in which the grain orientations are represented by discrete variables. An advantage of this method is the straightforward implementation and easy calibration of model parameters. However, the problem size can easily grow as the number of phase fields increase proportionally to the number of grain orientations. Robust coupling between phase field functions and crystal plasticity is another challenge in this type of methods.

Modeling the sharp transition in the phase field near the grain boundaries associated with the lattice orientation often requires highly refined discretization for sufficient accuracy, which significantly increases the computational cost. While adaptive model refinement can be employed for enhanced effectiveness, it is cumbersome for the traditional mesh-based methods to perform adaptive model refinement. While the deep neural network (DNN) has been applied to the solution of partial differential equations, the employment of a fully connected NN layers results in a tremendously large number of unknown parameters. Systematic analysis on the interpretability of the weights and biases in DNN for approximation space construction is still lacking for an effective application to strain localization problems.

1.2. Objectives

The objective of this work is to develop a mathematical and computational framework for accurate, stable, and computationally efficient modeling of grain refinement processes. The major developments are summarized as follows:

- Development of duality-based Cosserat crystal plasticity coupled with phase field. In Cosserat crystal plasticity, lattice rotations are employed as independent variables, which introduces the GND-induced nonlocal effects into the plastic deformation of the media. This is computationally less demanding than strain gradient-typed formulations due to less additional degrees of freedom. However, the conventional approach by penalizing the kinematic incompatibility between lattice orientation and displacement-based elastic rotation leads to significant solution sensitivity to the penalty parameter, resulting in low accuracy and convergence rates. To address this issue, the rotational compatibility condition is introduced based on the dualization of the primal Cosserat crystal plasticity and the phase field formulation.
- Thorough stability analysis of the proposed duality-based formulation. Multi-field formulation can lead to instability if the approximation functions are not consistent in the sense of coercivity in the saddle-point problems, often referred to as the inf-sup condition. The first part of this work formulates the dual problems of the Cosserat crystal plasticity subject to compatibility between lattice rotation and displacement based elastic rotation. The second part of this work addresses the stability issue of the multi-field variation formulation of Cosserat crystal plasticity by introducing a weak inf-sup condition for coercivity via a skew-symmetric stress projection. An additional least squares stabilization is introduced to suppress the spurious lattice rotation modes

with the stability condition of the least-squares stabilization parameter derived analytically and validated numerically. The proposed formulation is shown to yield superior accuracy and convergence with marginal parameter sensitivity compared to the conventional penalty-based approach.

- Development of a neural network enhanced reproducing kernel particle method. The phase field method often requires highly refined discretization for accurate prediction, which significantly increases the computational cost. While adaptive model refinement can be employed for reduced computational effort, it is cumbersome for the traditional mesh-based methods to perform the adaptive model refinement. In this work, a neural network-enhanced reproducing kernel particle method (NN-RKPM) is proposed, where the location and orientation of strain localizations are automatically detected, and the distribution of the solution transition is formulated accordingly by the NN approximation via the minimization of total potential energy. The standard RK approximation is then utilized to approximate the smooth part of the solution to permit a much coarser discretization than the fine discretization needed to capture sharp solution transition in the conventional methods. The proposed NN-RKPM is verified by solving the several damage evolution verification problems.
- Application of the proposed computational methods to problems involving grain refinement mechanisms in the rotational recrystallization process. The proposed duality-based Cosserat crystal plasticity – phase field formulation is applied to problems of block dislocation structure formation and grain boundary rotation at a triple junction. Compared to the analytical solution and experimental results, the numerical results properly capture the key phenomena in the rotational recrystallization.

It is further demonstrated that the proposed NN-RKPM is capable of capturing the fine resolution in the solution transition with coarse RK discretization.

1.3. Outline

The remainder of this dissertation is organized as follows. In Chapter 2, an overview on the grain refinement mechanisms, crystal plasticity theories, numerical approaches for modeling grain boundaries, and physics-informed neural networks for solving partial differential equations are given. In Chapter 3, the physics and fundamentals of orientation phase field method and Cosserat crystal plasticity along with the advantages and disadvantages of the existing approaches are discussed. In Chapter 4, a duality-based mathematical and computational formulation with stabilizations is presented. In this chapter, the Cosserat energy functional of the primal problem is first dualized to introduce independent lattice orientation degrees of freedom, and the dual variable in the dual problem is derived. A least squares stabilization term is included in the augmented multi-field functional for suppression of the spurious lattice rotation modes. In Chapter 5, the proposed duality-based multi-field formulation is discretized by the reproducing kernel particle method (RKPM). In Chapter 6, stability analyses on the duality-based formulation are performed. A weak inf-sup analysis identifies conditions for the coercivity, and the stability condition is fulfilled by a skew-symmetric stress projection. Also, a mathematical deviation provides the stability range for the least-squares stabilization parameter. A series of verification problems were analyzed to demonstrate superior accuracy and stability of the proposed method, as well as its parameter insensitivity of the formulation with a justifiable computational cost. In Chapter 7, a neural network enhanced RKPM is proposed. Neural network architectures are developed with interpretable weights and biases to automatically detect the locations and orientations of strain

localization, and to construct the distribution of solution transitions near the grain boundaries in an efficient manner. Also, details of the network structure that incorporates the RK approximation are provided. The proposed NN-RKPM is first verified by solving several damage evolution problems. In Chapter 8, the proposed methods are applied to problems involving block dislocation structure formation and grain boundary rotation that are the key phenomena in the rotational recrystallization mechanism. Lastly, conclusion remarks are given with the suggestions of future work in Chapter 9.

Acknowledgments

A portion of this chapter has been published in Baek, J., Chen, J. S., Zhou, G., Arnett, K., Hillman, M., Hegemier., G., & Hardesty, S. (2021) "A semi-Lagrangian reproducing kernel particle method with particle-based shock algorithm for explosive welding simulation". Computational Mechanics, 67,1601-1627. The dissertation author was the primary investigator of this material.

A portion of this chapter has been accepted for publication in Baek, J., Chen, J. S., Tupek, M., Beckwith, F., & Fang, H. E. "A Duality-based Coupling of Cosserat Crystal Plasticity and Phase Field Theories for Modeling Grain Refinement", International Journal for Numerical Methods in Engineering. The dissertation author was the primary investigator of this material.

A portion of this chapter is currently being prepared for submission for publication in Baek, J., Chen, J. S., Susuki, K., Beckwith, F., Tupek, M., & Fang, H. E. "Neural Network-enhanced

Reproducing Kernel Particle Method for Modeling Localizations". The dissertation author was the primary investigator of this material.

A portion of this chapter is currently being prepared for submission for publication in Baek, J., Chen, J. S., Beckwith, F., Tupek, M., & Fang, H. E. "Neural Network-enhanced Reproducing Kernel Particle Method for Modeling Grain Refinement". The dissertation author was the primary investigator of this material.

Chapter 2

Literature Review

2.1. Grain Refinement in High-rate Manufacturing Processes and Grain Refinement Mechanisms

Grain refinement is frequently caused by extreme deformation processes of metallic materials. It has been observed that equiaxed, very fine grains are formed during adiabatic strain localizations in various metals [25, 29, 30]. Similar phenomena occur in high-rate manufacturing processes such as cold spray additive manufacturing [21] and high velocity impact welding [1, 5], and drastically change material properties in the manufactured products. Meyers et al. [25] attributed this localization-induced grain refinement to the rotational recrystallization mechanism illustrated in Figure 2.1. At the first stage of the rotational recrystallization, the grains are subjected to very large elongation due to shear localization. The deformations are highly anisotropic due to the presence of slip systems. Then, to accommodate such large deformations, geometrically necessary dislocations (GNDs) are locally accumulated (refer to [31] for more information on GNDs) and such self-organization of GNDs generates several isolated blocks of the original grains (block dislocation structures, see Figure 2.1(c)). Due to the large lattice curvature in the high density GNDs, each isolated block undergoes a lattice orientation that distinguishes itself from the surrounding blocks. Thin zones with high GND density divide into sub-grains with low-angle grain boundaries. As shown in Figure 2.1(c) – (d), the grain boundaries migrate to minimize the energy by evolving the angles at the triple junctions. Such slight migrations of the grain boundaries result

in refined equiaxed grains. Also, the crystalline lattice of the subgrains rotate and the low-angle grain boundaries gradually evolve into high-angle grain boundaries. This mechanism is often called continuous dynamic recrystallization with progressive accumulation of geometrically necessary dislocations (GNDs)[32]. Under high-temperature deformation, this recrystallization mechanism has been observed in various metals[33, 34].

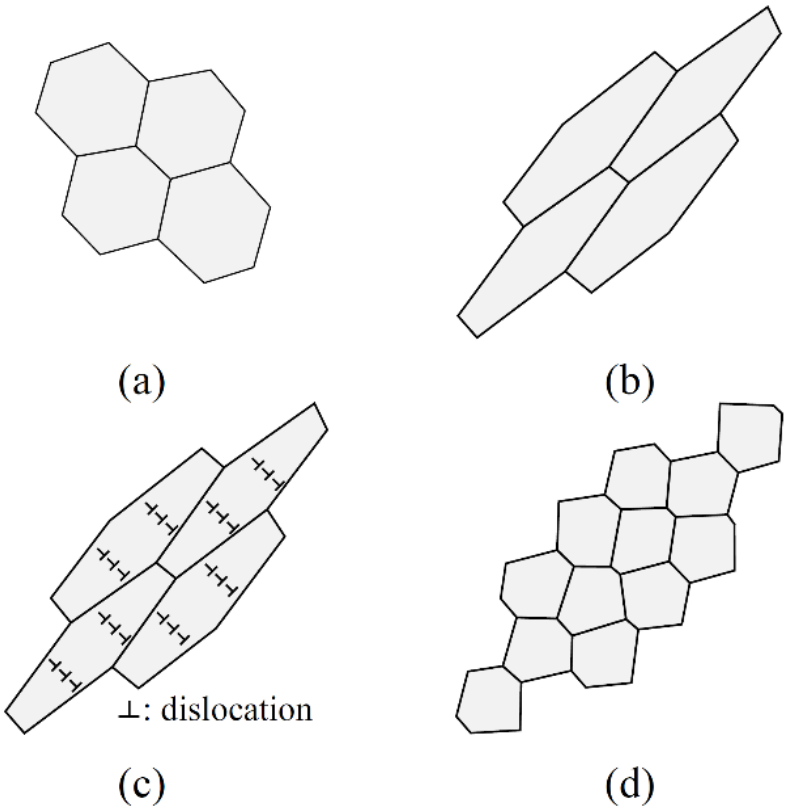

Figure 2.1. Mechanism of rotational recrystallization: (a) initial grains, (b) strain localization-induced extreme deformation, (c) geometrically necessary dislocations and block dislocation structures, and (d) equiaxed refined grains produced by grain boundary migrations

2.2. Overview of Numerical Methods for Grain Refinement Modeling

Numerical modeling of the aforementioned recrystallization mechanism is challenging as it entails extreme material deformations, nonlocal effects of GNDs, discontinuities in lattice orientation (localizations of lattice curvature), and moving grain boundaries. While numerical modeling in very small length scales such as atomic scale[35–37] and dislocation scale[38, 39] can be considered, it is computationally too expensive for such small-scale models to simulate polycrystalline structures despite of their predictive capability[40]. On the other hand, continuum meso-scale approaches such as crystal plasticity treat dislocations with a continuous dislocation density field, and it has been demonstrated that crystal plasticity theories can accurately capture the anisotropic viscoplastic deformations by considering plastic slips and applied shear stresses on individual slip systems. In order to model the nonlocal effects associated with GNDs, strain gradient-typed crystal plasticity has been proposed[41–45]. In this class of models, plastic slip on each slip system is introduced as additional degrees of freedom. While effective in modeling GND-induced deformations that are related to the gradient of plastic slip, the method is computationally costly as a significant number of independent variables are required. Forest[46] proposed a Cosserat crystal plasticity formulation by utilizing the close relation between GND and the lattice curvature established in earlier works[47, 48]. In Cosserat crystal plasticity[46, 49–51], lattice rotations are introduced as independent variables, which is computationally less extensive than strain gradient-typed formulations due to fewer additional degrees of freedom. However, solution sensitivity to the penalty parameter can be an issue in the widely used penalty-based Cosserat crystal plasticity. While both methods have been successfully applied to the modeling of deformation-induced localizations of GNDs and the resulting block dislocation structures[52, 53], these methods have limitations in capturing grain boundary migration which is an important

mechanism in the rotational recrystallization due to the complexities involved the evolution of grain topology during the grain boundary migrations.

Various methods have been proposed to model grain boundary migrations[54], including phase field methods[55–58], level-set methods[59–62], cellular automation[63–65], and double-grid reproducing kernel particle method[66, 67]. Phase field methods for modeling grain boundary migration are classified into two categories: multi-phase field method and orientation phase field method. In the multi-phase field method[55, 56], multiple phase fields are introduced and each phase is associated with a specific grain orientation, in which the grain orientations are represented by discrete variables. An advantage of this method is the straightforward implementation and easy calibration of model parameters. However, the problem size can easily grow as the number of phase fields are proportional to the number of grain orientations. Robust coupling between phase field functions and crystal plasticity is another challenge for this type of method. A second class of the phase field approach is the orientation phase field theory[57, 58] in which a scalar phase field is introduced in addition to the continuous lattice orientation field to capture regions with large lattice curvature and to correct the grain boundary (GB) energy. As the derivative of the orientation field (lattice curvature) and the GND density are closely related to each other[47, 48], a direct coupling of the orientation phase field theory with a crystal plasticity theory via the Helmholtz-free energy can be better formulated. In prior work[68, 69], the coupling of orientation phase field method and Cosserat crystal plasticity has been considered. Similarly, a coupled orientation phase field and strain gradient-type crystal plasticity theory has been introduced[70]. Also, the orientation phase field method has been coupled with elasto-plasticity[71]. The flexibility in a direct coupling with crystal plasticity is an attractive feature in the orientation phase field method compared to other methods[72].

Discretization sensitivity is a major computational challenge in modeling grain boundaries which are regions of localized lattice curvature. In general, if the discretization sensitivity is not properly addressed for a problem involving localization, numerical results including energy, force, and localization patterns can be strongly mesh-dependent due to the loss of ellipticity in the mathematical formulation[73]. For example, the grain growth kinetics tends to be strongly influenced by the type of grid in cellular automation[61]. There have been several numerical approaches proposed for regularization of the mesh-dependent numerical defects. Some localization problems have been successfully solved by, introducing nonlocal models with intrinsic length scales, such as quantity averaging[74] and high order gradient models[75–77]. While high order gradients are troublesome in C_0finite elements, it is noteworthy that an implicit gradient method in the form of convolution integral has been proposed to implicitly reproduce higher order gradient without taking direct derivatives[78, 79]. The phase field approach[80, 81] is another class of regularization technique where discontinuous fields are approximated by the diffusive phase fields, and the coupling of the phase field and other degrees of freedom is attained within the free energy. Similar to the nonlocal methods, length scales are introduced in the phase field methods and they serve as localization limiters. The regularization property is a unique feature in the aforementioned multi-phase method and orientation phase field method for modeling strain localization problems.

2.3. Physics-informed Neural Network for Solving Partial Differential Equations

The deep artificial neural network has demonstrated its impressive ability in information processing such as image recognition, and more recently, is rapidly extending its regime into various fields including mechanistic machine learning. Its successful adoption is mainly attributed

to the adaptive nature of manipulating the function space based on data in the frame of minimization of the loss function. Such flexibility brings a computational model the capability to capture certain information that is hard to be detected by conventional approaches. For example, He et al. (2021) [82] introduced the deep autoencoder to discover the latent low-dimensional data pattern embedded in noisy material datasets and significantly enhanced the effectiveness of the physics-constrained data-driven approach developed by He and Chen (2020) [83]. Lee and Carlberg (2020) [84] proposed a model order reduction technique based on low-dimensional nonlinear manifolds constructed by the deep convolutional autoencoder and demonstrated the outperformance over linear subspace-based reduce order modeling techniques.

Recently, the utilization of neural networks (NNs) for solving partial differential equations (PDE) in physics and mechanics has been drawing increasing attention. In this class of studies, the potential of NN used as an approximation is explored, considering its flexible function space construction. Raissi et al. (2019) [85] introduced the terminology physics-informed neural network (PINN) which serves as an approximation of the solution of a PDE in the framework of collocation method and show the effectiveness of the method on one-dimensional Burgers equation using densely connected deep neural networks with the hyperbolic tangent activation function. As the solution of Burgers equation is a typical hyperbolic tangent-type function, the solution was accurately captured. Haghighat and Juanes (2021) [86] introduced a Python package SciANN for scientific computing using PINN and showed that the method captured strain and stress localization produced in a perfectly plastic material. However, they used 4 densely connected layers with 100 neurons per layer, which involves 100 million unknowns, to obtain the results. Samaniego et al. (2020) [87] established that the potential-based loss functions leads to better results with significantly less unknowns than the collocation-based loss function widely used in

PINN. However, the aforementioned studies employed a fully connected multiple hidden layers, which may not be an optimal choice to describe behaviors of materials. Zhang et al. (2020) [88] devised the deep neural networks to represent standard approximations such as finite elements and reproducing kernel particles, and treated the nodal positions as unknown network parameters. This element or particle-wise network is a sparse network showing a potential of designing more efficient network. Lee et al. (2021) [89] introduced a partition of unity network which possesses the properties of optimal convergence and showed how NN partitions the domain and approximates smooth and piecewise smooth functions. Although NN for solving PDEs in physics and mechanics draws increasing attention, the volume of research and discussion on development of NN for modeling discontinuities and localizations remains very limited and deserves further investigation.

Acknowledgments

A portion of this chapter has been accepted for publication in Baek, J., Chen, J. S., Tupek, M., Beckwith, F., & Fang, H. E. "A Duality-based Coupling of Cosserat Crystal Plasticity and Phase Field Theories for Modeling Grain Refinement", International Journal for Numerical Methods in Engineering. The dissertation author was the primary investigator of this material.

A portion of this chapter is currently being prepared for submission for publication in Baek, J., Chen, J. S., & Susuki, K. "Neural Network-enhanced Reproducing Kernel Particle Method for Modeling Localizations". The dissertation author was the primary investigator of this material.

A portion of this chapter is currently being prepared for submission for publication in Baek, J. & Chen, J. S. “Neural Network-enhanced Reproducing Kernel Particle Method for Modeling Grain Refinement”. The dissertation author was the primary investigator of this material.

Chapter 3

Physics and Fundamentals of Orientation Phase Field Method and Cosserat Crystal Plasticity

In this chapter, the Cosserat crystal plasticity theory and its coupling with the phase field method are reviewed. The coupling of Cosserat crystal plasticity and the orientation phase field method is formulated naturally as the internal energy associated with lattice curvature has contribution from both models. Also, the regularization properties in the orientation phase field method ensure consistent grain boundary energy independent of the choice of discretization. Penalty method in the conventional approach is used to impose kinematic constraints on the displacement-based and lattice orientation-based lattice curvatures.

3.1. Primal problem

3.1.1. Kinematics

Let the displacement $\mathbf{u} \in \mathbb{R}^d$ with space dimension d be defined as $\mathbf{u} = \mathbf{x}(\mathbf{X}, t) - \mathbf{X}$ where $\mathbf{X} \in \mathbb{R}^d$ and $\mathbf{x}(\mathbf{X}, t) \in \mathbb{R}^d$ are the material coordinates and the current coordinates, respectively, as shown in Figure 3.1.

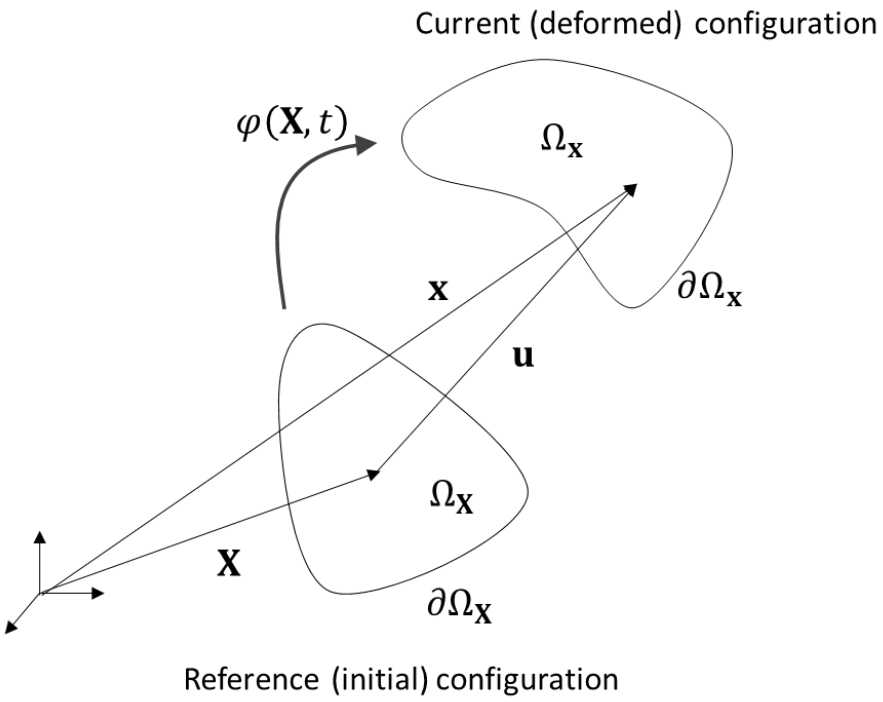

Figure 3.1. Deformation of a material body

The deformation gradient is defined as

$$\mathbf{F} = \frac{\partial \mathbf{x}}{\partial \mathbf{X}} = \mathbf{I} + \mathbf{e}, \qquad F_{ij} = x_{i,j} = \delta_{ij} + e_{i,j}, \tag{3.1}$$

with $(\cdot)_{i,j} \equiv \partial(\cdot)_i / \partial X_j$, and the displacement gradient is additionally defined as follows:

$$e_{ij} = u_{i,j} \tag{3.2}$$

As shown in Figure 3.2, the total deformation of the crystallographic lattice can be decomposed into three components: plastic slip, lattice deformation, and lattice rotation. In the continuum description of crystal plasticity, the lattice deformation and the lattice rotation are considered

identical to the elastic stretch and the elastic rotation, respectively, and the multiplicative decomposition is constructed as follows:

$$\mathbf{F} = \mathbf{F}^e\mathbf{F}^p = \mathbf{R}\mathbf{U}^e\mathbf{F}^p, \tag{3.3}$$

where $\mathbf{F}^e$, $\mathbf{F}^p$, $\mathbf{R}$, and $\mathbf{U}^e$ are elastic deformation gradient, plastic deformation gradient, elastic rotation tensor, and elastic stretch, respectively.

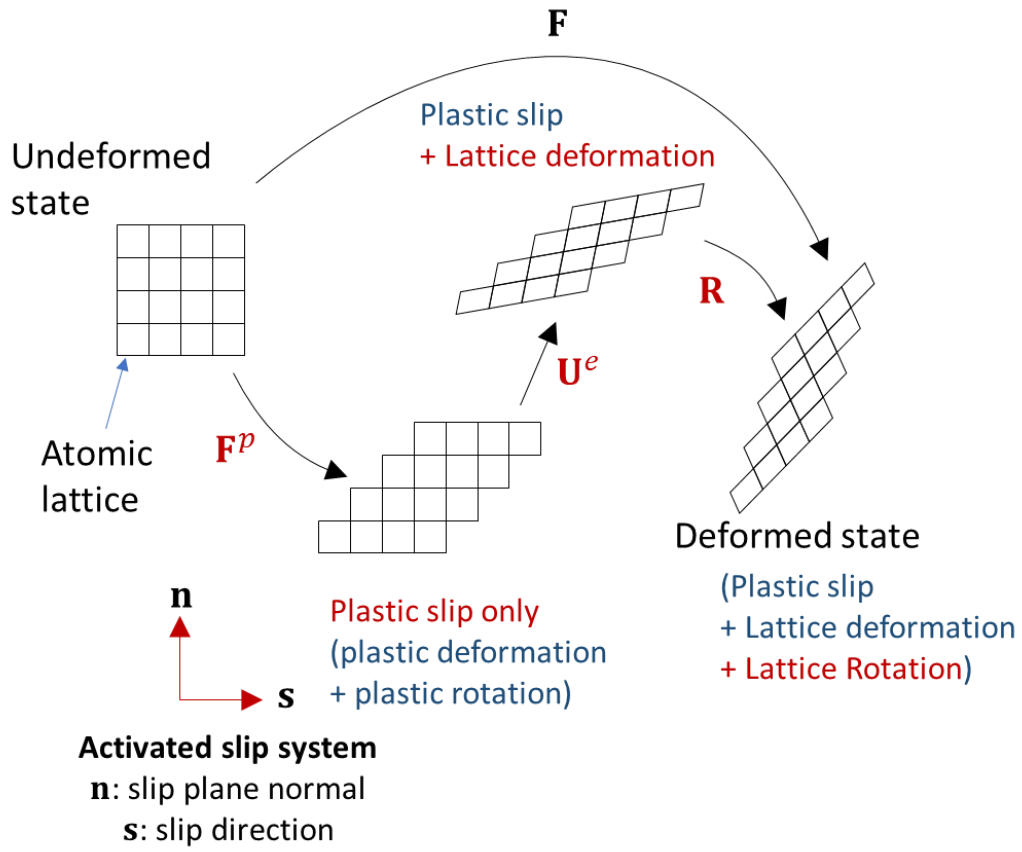

Figure 3.2. Multiplicative decomposition of deformation

Under the small strain assumption, strain $\boldsymbol{\varepsilon}$ and material rotation $\boldsymbol{\varphi}$ are defined as follows:

$$\varepsilon_{ij} = \frac{1}{2}\left(e_{ij} + e_{ji}\right), \tag{3.4}$$

and

$$\varphi_i = -\frac{1}{2}\epsilon_{ijk}e_{jk}, \tag{3.5}$$

where ϵ_{ijk} is the third-rank permutation tensor, and the decomposition described in Eq. (3.3) can be approximated as an additive decomposition:

$$e_{ij} = e_{ij}^{e} + e_{ij}^{p} = -\epsilon_{ijk}\varphi_k^{e} + \varepsilon_{ij}^{e} + e_{ij}^{p}, \tag{3.6}$$

where e_{ij}^{e}, e_{ij}^{p}, ε_{ij}^{e}, and φ_k^{e} are elastic displacement gradient, plastic displacement gradient, elastic strain, and elastic rotation, respectively. In (3.6), the elastic displacement gradient e_{ij}^{e} is decomposed into its symmetric and skew-symmetric parts using elastic strain ε_{ij}^{e} and elastic rotation φ_k^{e} as follows:

$$e_{ij}^{e} = \varepsilon_{ij}^{e} - \epsilon_{ijk}\varphi_k^{e}, \tag{3.7}$$

with

$$\varepsilon_{ij}^{e} = \frac{1}{2}\left(e_{ij}^{e} + e_{ji}^{e}\right), \tag{3.8}$$

and

$$\varphi_k^{\mathrm{e}} = -\frac{1}{2}\epsilon_{kmn}e_{mn}^{e}. \tag{3.9}$$

Similarly, the plastic displacement gradient can be decomposed as follows:

$$e_{ij}^{p} = \varepsilon_{ij}^{p} - \epsilon_{ijk}\varphi_k^{p}, \tag{3.10}$$

where the plastic strain ε_{ij}^{p} and the plastic rotation φ_k^{p} are defined as

$$\varepsilon_{ij}^{p} = \frac{1}{2}\left(e_{ij}^{p} + e_{ji}^{p}\right), \tag{3.11}$$

and

$$\varphi_k^{p} = -\frac{1}{2}\epsilon_{kmn}e_{mn}^{p}. \tag{3.12}$$

From Eqs. (3.6)-(3.12), e_{ij} and φ_i can also be described with the additive decomposition as follows:

$$\varepsilon_{ij} = \varepsilon_{ij}^{e} + \varepsilon_{ij}^{p} \tag{3.13}$$

and

$$\varphi_i = \varphi_i^{e} + \varphi_i^{p}. \tag{3.14}$$

3.1.2. Energy functional

In this work, we start with a framework in which the Cosserat crystal plasticity and the phase field theories are coupled via the Helmholtz free energy[68]. In the primal problem, two independent field variables are introduced: displacement $\mathbf{u} \in \mathbb{R}^d$ and phase field $\eta \in [0,1] \subset \mathbb{R}$. The Helmholtz free energy of the primal problem is defined as follows:

$$\psi(\mathbf{u}, \eta) = \frac{1}{2}\varepsilon^e_{ij}(\mathbf{u})C_{ijkl}\varepsilon^e_{kl}(\mathbf{u}) + \alpha f(\eta)\|\nabla\boldsymbol{\varphi}^e(\mathbf{u})\| + \frac{\beta}{2}g(\eta)\|\nabla\boldsymbol{\varphi}^e(\mathbf{u})\|^2 + pr(\eta) + \frac{q}{2}(\nabla\eta)^2, \tag{3.15}$$

where $\|\mathbf{A}\| = \sqrt{A_{ij}A_{ij}}$, C_{ijkl} is the elasticity tensor, $f(\eta)$ and $g(\eta)$ are coupling functions, and α, β, p, and q are material constants. Tensor notations are used herein, where repeated indices denote summation unless otherwise stated. The first term of the right-hand side of Eq. (3.15) is the Cauchy strain energy density. The second term, linear Cosserat energy density, represents the self-energy of geometric necessary dislocations (GNDs), which is the elastic energy that GNDs produce in the surrounding material. The third term, the quadratic Cosserat energy density, represents the interaction energy of GNDs, which is the energy produced when multiple GNDs interact with each other. The linear term is particularly important in modeling grain boundaries since, without the linear term, localized lattice curvature (i.e. presence of grain boundaries) cannot minimize energy in the absence of an external load[58]. The constants α and β contain the Cosserat length scales and can be written as

$$\alpha \equiv E_\theta \ell_\alpha, \qquad \beta \equiv E_\theta \ell_\beta^2, \tag{3.16}$$

where E_θ, ℓ_α, and ℓ_β are reference Cosserat energy density, length scale associated with the linear Cosserat energy, and length scale associated with the quadratic Cosserat energy, respectively. Typically, the reference Cosserat energy density is chosen to be $E_\theta = \mu$ with μ the shear modulus[46, 51]. Although closely related to smaller scale material behaviors, the length scales are usually calibrated through experimental data. As the linear Cosserat energy term tends to make a sharp transition of lattice orientation at a grain boundary and the quadratic Cosserat energy term tends to diffuse it[58], a larger ℓ_α/ℓ_β ratio leads to more localized grain boundaries.

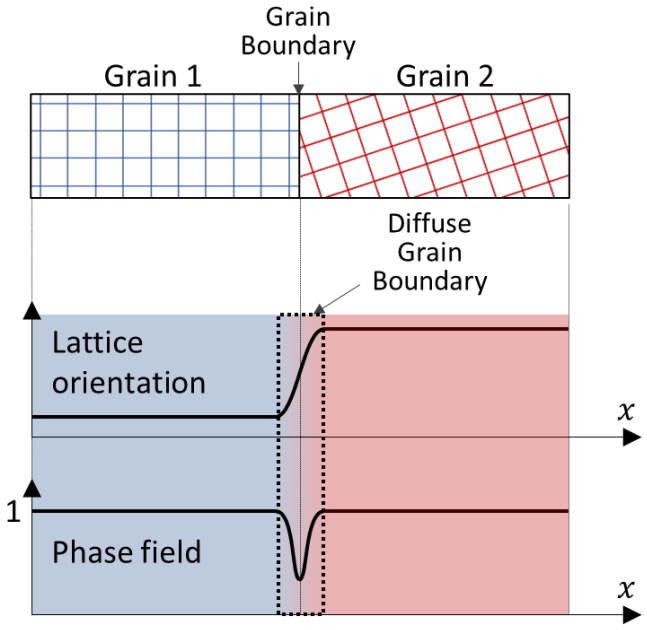

Figure 3.3. Diffuse grain boundary representation in the orientation phase field method

In the phase field method, the discontinuous lattice orientation field across a grain boundary is approximated by the diffuse grain boundary representation, which is schematically described in Figure 3.3. In the diffuse grain boundary region, the lattice orientation field $\boldsymbol{\varphi}^e$ smoothly changes and the phase field gradient captures the large lattice curvature so that the phase

field has a value $\eta \approx 1$ in the bulk grain and decreases to a smaller value in the diffuse grain boundary region.

The term $pr(\eta)$ in (3.15) is homogeneous phase field free energy density and various functional forms of $r(\eta)$ can be considered. In Appendix A, the effects of the following quadratic and linear phase field free energy functions on the diffusive behavior of phase field are discussed:

$$r(\eta) = \frac{1}{2}(1-\eta)^2, \tag{3.17}$$

$$r(\eta) = |1-\eta|. \tag{3.18}$$

The term last term in (3.15), $\frac{q}{2}(\nabla\eta)^2$, is a penalty term associated with the phase field gradient with positive constant q. The phase field η captures grain boundaries and corrects the GB energies. With positive p and q, and positive coupling functions $f(\eta)$ and $g(\eta)$, $\eta \approx 1$ in the region where $\|\nabla\boldsymbol{\varphi}^e\| \approx 0$, i.e., inside bulk grains, while $\eta < 1$ in the region where $\|\nabla\boldsymbol{\varphi}^e\| > 0$. The phase field model constants p and q can be expressed as

$$p = E_\eta, \qquad q = E_\eta \ell_\eta^2, \tag{3.19}$$

where E_η and ℓ_η are reference phase field energy density and phase field length scale, respectively, which should be calibrated such that the model accurately represents the experimentally observed GB energy. The functions $f(\eta)$ and $g(\eta)$ couple the Cosserat crystal plasticity and phase field theories. A common example is $f(\eta) = g(\eta) = \eta^2$. More generally, a polynomial form[90] can be taken as $f(\eta) = \sum_{m=0}^{N} A_m^f \eta^m$ and $g(\eta) = \sum_{m=0}^{N} A_m^g \eta^m$ or nonstandard forms, such as a quasi-

linear function[91]. The effects of several combinations of r, f, and g on the GB energy profiles and diffuse GB widths against misorientation are discussed in Section 3.3.

3.1.3. Governing equations and constitutive laws

By applying the principle of virtual power, the set of governing equations are obtained as follows.

$$\begin{aligned}
\sigma_{ij,j} + b_i = 0 \quad & \text{in} \quad \Omega \times]0,T[\\
m_{ij,j} - \epsilon_{ijk}\sigma_{ij} = 0 \quad & \text{in} \quad \Omega \times]0,T[\\
\pi_{i,i}^{\nabla\eta} - \pi^{\eta} = \mu^{\eta}\dot{\eta} \quad & \text{in} \quad \Omega \times]0,T[\\
u_i = \bar{u}_i \quad & \text{on} \quad \partial\Omega^{g_i} \times]0,T[\\
\sigma_{ij}n_j = h_i \quad & \text{on} \quad \partial\Omega^{h_i} \times]0,T[\\
\varphi_i^e = \bar{\varphi}_i \quad & \text{on} \quad \partial\Omega^{\bar{\varphi}_i} \times]0,T[\\
m_{ij}n_j = \bar{c}_i \quad & \text{on} \quad \partial\Omega^{\bar{c}_i} \times]0,T[\\
\eta = \bar{\eta} \quad & \text{on} \quad \partial\Omega^{\bar{\eta}} \times]0,T[\\
\pi_i^{\nabla\eta} n_i = \bar{\pi} \quad & \text{on} \quad \partial\Omega^{\bar{\pi}} \times]0,T[\\
\eta(t=0) = \eta_0 \quad & \text{in} \quad \Omega
\end{aligned} \tag{3.20}$$

where $\boldsymbol{\sigma}$, $\mathbf{m}$, π^{η}, $\boldsymbol{\pi}^{\nabla\eta}$, and $\mathbf{b}$ are generalized stress, couple stress, phase field microstress associated with η, phase field microstress associated with $\nabla\eta$, and body force, respectively, $\mathbf{n}$ denotes boundary surface normal, $\bar{\mathbf{u}}$, $\bar{\boldsymbol{\varphi}}$, and $\bar{\eta}$ are essential boundary values applied to the corresponding essential boundaries $\partial\Omega^{g_i}$, $\partial\Omega^{\bar{\varphi}_i}$, and $\partial\Omega^{\bar{\eta}}$, and $\mathbf{h}$, $\bar{\mathbf{c}}$, and $\bar{\pi}$ are natural boundary values applied to the corresponding natural boundaries $\partial\Omega^{h_i}$, $\partial\Omega^{\bar{c}_i}$, and $\partial\Omega^{\bar{\pi}}$, and their definitions are to be given below. The first, second, and third equations in (3.20) are the balance of linear momentum, balance of angular momentum, and balance of phase field micro-stresses, respectively. The generalized stress $\boldsymbol{\sigma}$ is defined as

$$\sigma_{ij} = \sigma_{ij}^{c} + \sigma_{ij}^{a}, \tag{3.21}$$

where σ_{ij}^{c} is the standard symmetric Cauchy stress and σ_{ij}^{a} is a nonstandard skew-symmetric stress. Note that the balance of angular momentum is exactly satisfied in the primal problem where $\varphi_{ij}^{e}(\mathbf{u})$ is a displacement-based quantity and σ_{ij}^{a} is defined accordingly as

$$\sigma_{ij}^{a} = \frac{1}{2}\epsilon_{ijk} m_{kl,l}. \tag{3.22}$$

The constitutive relations can be motivated by the Clausius-Duhem inequality under the isothermal condition:

$$-\dot{\psi} + \mathscr{p}^{int} \geq 0, \tag{3.23}$$

where $\mathscr{p}^{int}$ is the internal virtual power density:

$$\mathscr{p}^{int} = \sigma_{ij}\dot{e}_{ij} + \epsilon_{ijk}\sigma_{jk}\dot{\varphi}_{i}^{e} + m_{ij}\dot{\varphi}_{i,j}^{e} + \pi^{\eta}\dot{\eta} + \pi_{i}^{\nabla\eta}\dot{\eta}_{,i}. \tag{3.24}$$

By utilizing $\dot{\varphi}_{i}^{e} = -\frac{1}{2}\epsilon_{ijk}\dot{e}_{jk}^{e}$ and $\epsilon_{ijk}\epsilon_{imn}\sigma_{jk} = \left(\delta_{jm}\delta_{kn} - \delta_{jn}\delta_{km}\right)\sigma_{jk} = 2\sigma_{mn}^{a}$, Eq. (3.24) becomes

$$\mathscr{p}^{int} = \sigma_{ij}\dot{e}_{ij}^{p} + \sigma_{ij}^{c}\dot{e}_{ij}^{e} + m_{ij}\dot{\varphi}_{i,j}^{e} + \pi^{\eta}\dot{\eta} + \pi_{i}^{\nabla\eta}\dot{\eta}_{,i}, \tag{3.25}$$

which leads to

$$\left(\sigma_{ij}^{c}-\frac{\partial\psi}{\partial e_{ij}^{e}}\right)\dot{e}_{ij}^{e}+\left(m_{ij}-\frac{\partial\psi}{\partial\varphi_{i,j}^{e}}\right)\dot{\varphi}_{i,j}^{e}+\left(\pi^{\eta}-\frac{\partial\psi}{\partial\eta}\right)\dot{\eta}+\left(\pi_{i}^{\nabla\eta}-\frac{\partial\psi}{\partial\eta_{,i}}\right)\dot{\eta}_{,i}+\sigma_{ij}\dot{e}_{ij}^{p}\geq 0. \tag{3.26}$$

Consequently, Cauchy stress is obtained as

$$\sigma_{ij}^{c}=C_{ijkl}\varepsilon_{kl}^{e}, \tag{3.27}$$

the couple stress **m** is obtained as

$$m_{kl}=\left(\frac{\alpha f(\eta)}{\|\nabla\boldsymbol{\varphi}^{e}\|}+\beta g(\eta)\right)\varphi_{k,l}^{e}, \tag{3.28}$$

and the phase field micro-stresses are defined as

$$\pi^{\eta}=pr_{,\eta}+\alpha f_{,\eta}\|\nabla\boldsymbol{\varphi}^{e}\|+\frac{\beta g_{,\eta}}{2}\|\nabla\boldsymbol{\varphi}^{e}\|^{2}, \tag{3.29}$$

$$\pi_{i}^{\nabla\eta}=q\eta_{,i}. \tag{3.30}$$

The plastic behavior is determined by introducing a plastic dissipation potential W^{p}. For example[92, 93],

$$W^{p}=\sum_{I=1}^{N_{S}}\frac{K_{v}}{n+1}\langle\frac{\left|\tau^{(I)}\right|-R^{(I)}}{K_{v}}\rangle^{n+1}+\frac{1}{2}\mu_{*}^{-1}(\eta,\nabla\boldsymbol{\varphi}^{e})\sigma_{ij}^{a}\sigma_{ij}^{a}, \tag{3.31}$$

where $\langle\cdot\rangle=\max(\cdot,0)$. The first term on the right-hand side of Eq. (3.31) represents the contribution of plastic slip on each slip system to the global plastic potential. $R^{(I)}$ is the critical

resolved shear stress on slip system I, N_s is the number of slip systems, and K_v and n are model constants. The critical resolved shear stress can evolve under consideration of generation and annihilation of dislocations. The resolved shear stress $\tau^{(I)}$ acting on slip system I is defined as

$$\tau^{(I)} = s_i^{(I)} \sigma_{ij} n_j^{(I)}, \tag{3.32}$$

where $\mathbf{s}^{(I)}$ and $\mathbf{n}^{(I)}$ are the slip direction and the slip plane normal vectors of the slip system I, respectively. Further, the second term of Eq. (3.31) represents the diffusive behavior of grain boundary. The function $\mu_*(\eta, \nabla\boldsymbol{\varphi}^e)$ is grain boundary inverse mobility, of which the value is small inside grain boundaries and large in bulk grains so that the second term is only activated in the grain boundary regions. For example, $\mu_* = \hat{\mu}_*\big(1 - \big(1 - \mu_p\big)\exp(-\beta_P \|\nabla\boldsymbol{\varphi}^{\mathrm{e}}\|)\big)$ can be considered with the reference inverse mobility $\hat{\mu}_*$ and model constants μ_p and β_p.

The velocity gradient is derived from Eq. (3.31) $\dot{e}_{ij}^p = \partial W^p / \partial \sigma_{ij}$ as follows:

$$\dot{e}_{ij}^p = \sum_{I=1}^{N_s} \dot{\gamma}^{(I)} s_i^{(I)} n_j^{(I)} + \mu_*^{-1}(\eta, \nabla\boldsymbol{\varphi}^e)\sigma_{ij}^a, \tag{3.33}$$

where the plastic slip $\dot{\gamma}^{(I)}$ of slip system I is

$$\dot{\gamma}^{(I)} = \langle \frac{\left|\tau^{(I)}\right| - R^{(I)}}{K_v} \rangle^n \operatorname{sign}(\tau^I). \tag{3.34}$$

The above-mentioned displacement-based lattice orientation computational formulation often exhibits low accuracy since the displacement-based material rotation $\boldsymbol{\varphi}$ is approximated one order lower than that of $\mathbf{u}$ (see Eqs. (3.2) and (3.5)) and the plastic rotation $\boldsymbol{\varphi}^p$ is approximated

three orders lower than that of **u** (see Eqs. (3.22), (3.28), and (3.33)). This motivates the development of a mixed formulation. Also, note that the computation of $\boldsymbol{\sigma}^a$ in Eq. (3.22) requires the computation of high gradients of the plastic displacement gradient $\mathbf{e}^p$ ($e_i^e = e_i - e_i^p$), which leads to a numerically challenging PDE in Eq. (3.33). A duality-based mixed formulation to be introduced in Section 3 avoids computation of high order gradients of $\mathbf{e}^p$.

3.2. Penalty-based approach

Due to its simple numerical implementation, the penalty-based approach has been widely used for pure Cosserat crystal plasticity[46, 51] and its coupling with phase field methods[68, 93]. In the penalty approach, an independent lattice orientation field $\boldsymbol{\theta} \in \mathbb{R}^{\bar{d}}$ is introduced where $\bar{d} = 3$ when $d = 3$ and $\bar{d} = 1$ when $d = 2$ by imposing the kinematic constraint $\boldsymbol{\theta} = \boldsymbol{\varphi}^e$ with the penalty method as follows:

$$\begin{aligned}\psi(\mathbf{u}, \boldsymbol{\theta}, \eta) = \frac{1}{2}\varepsilon_{ij}^e \sigma_{ij}^c + \alpha f(\eta)\|\nabla\boldsymbol{\theta}\| + \frac{\beta}{2} g(\eta)\|\nabla\boldsymbol{\theta}\|^2 + 2\mu_c(\theta_i - \varphi_i^e)(\theta_i - \varphi_i^e) \\ + pr(\eta) + \frac{q}{2}(\nabla\eta)^2,\end{aligned} \tag{3.35}$$

where μ_c is penalty parameter and can be defined proportional to the shear modulus, $\mu_c = c\mu$, with normalized penalty parameter c. Then the Euler-Lagrange equations read

$$\begin{aligned} \sigma_{ij,j} + b_i = 0 \quad &\text{in} \quad \Omega \times]0, T[\\ m_{ij,j} - \epsilon_{ijk}\sigma_{jk}^a = 0 \quad &\text{in} \quad \Omega \times]0, T[\\ \pi_{i,i}^{\nabla\eta} - \pi^\eta = \mu^\eta \dot{\eta} \quad &\text{in} \quad \Omega \times]0, T[\end{aligned} \tag{3.36}$$

where

$$m_{ij} = \left(\frac{f(\eta)\alpha}{\|\nabla \boldsymbol{\theta}\|} + g(\eta)\beta \right) \theta_{i,j}, \tag{3.37}$$

$$\begin{aligned} \sigma_{ij} &= \sigma_{ij}^{c} + \sigma_{ij}^{a}, \\ \sigma_{ij}^{c} &= C_{ijkl}\varepsilon_{kl}^{e}, \\ \sigma_{ij}^{a} &= 2\mu_c \epsilon_{ijk}(\theta_k - \varphi_k^{e}). \end{aligned} \tag{3.38}$$

$$\pi^{\eta} = pr_{,\eta} + \alpha f_{,\eta}\|\nabla \boldsymbol{\theta}\| + \frac{\beta g_{,\eta}}{2}\|\nabla \boldsymbol{\theta}\|^2, \tag{3.39}$$

$$\pi_i^{\nabla \eta} = q\eta_{,i}. \tag{3.40}$$

The second equation in (3.36) represents the balance of angular momentum. In the derivation of the Euler-Lagrange equations, the penalty term in (3.35) leads to the specific form of $\boldsymbol{\sigma}^a$ in Eq. (3.38) which is different from $\boldsymbol{\sigma}^a$ in the primal problem. Note that $\boldsymbol{\sigma}^a$ does not contain high gradients of $\mathbf{e}^p$, which reduces the aforementioned complexity in solving the constitutive equation in (3.33). Also, the variational formulation of Eq. (3.35) only requires the independent field variables $\mathbf{u}$, $\boldsymbol{\theta}$, and η to be in H^1 spaces, which is another advantage for implementation in finite element methods. However, solutions of the penalty-based approach can be sensitive to the penalty parameter μ_c, and the convergence rate can be suboptimal if μ_c is not properly chosen. Low μ_c leads to large discrepancy between $\boldsymbol{\theta}$ and $\boldsymbol{\varphi}^e$ while large μ_c can result in locking unless functions spaces for $\boldsymbol{\theta}$ and $\boldsymbol{\varphi}^e$ are carefully selected. In this work, an alternative approach to introduce the lattice orientation field is proposed in Chapter 4 to overcome these drawbacks.

3.3. Phase Field Model Functions and Model Constants

The coupled Cosserat – phase field model involves three phase field model functions $r(\eta)$, $f(\eta)$, and $g(\eta)$, used in the orientation phase field formulations[58, 90]. Choosing proper functions is important to obtain a solution which is both physically meaningful and numerically well-regularized. A physically meaningful solution requires the correct nonlinear relationship between the GB energy and misorientation, e.g., a Read-Shockley type behavior, while a well-regularized solution must be insensitive to mesh discretization. Since the microstructure evolves and the level of misorientations can vary throughout a simulation, a given set of r, f, and g should provide well-behaved properties for a wide range of misorientations while avoiding overly-diffusive solutions.

For investigating the effects of the phase field model functions, we consider a one-dimensional version of Eq. (3.15) with the simplifying assumption $\varepsilon^e = 0$. Then, Eq. (3.15) is identical to the classical orientation phase field formulation [57] with the free energy functional

$$\psi = f(\eta)\alpha\left|\theta_{,x}\right| + g(\eta)\frac{\beta}{2}\left|\theta_{,x}\right|^2 + pr(\eta) + \frac{q}{2}\left|\eta_{,x}\right|^2. \tag{3.41}$$

The static problem is derived from $\min \Pi = \int_{-\infty}^{+\infty} \psi \, dx$ with boundary conditions $\theta(-\infty) = -\Delta\theta/2$, $\theta(\infty) = \Delta\theta/2$, and $\eta(-\infty) = \eta(\infty) = 1$, which leads to the following strong form problem [94, 95]:

$$\theta_{,x} = \begin{cases} \dfrac{\alpha}{\beta g(\eta)}\left(f(\bar{\eta}) - f(\eta)\right), & x \in [-\delta/2, +\delta/2] \\ 0, & \text{otherwise} \end{cases}, \tag{3.42}$$

$$\eta_{,x} = \begin{cases} \sqrt{p/q}\left(2r(\eta) - \dfrac{\alpha^2}{\beta p}\dfrac{1}{g(\eta)}\left(f(\bar{\eta}) - f(\eta)\right)^2\right)^{1/2}, & x \in [-\delta/2, +\delta/2] \\ \sqrt{p/q}\left(2r(\eta)\right)^{1/2}, & \text{otherwise} \end{cases} \tag{3.43}$$

where $\bar{\eta} \equiv \eta(x = \pm\delta/2)$ with the grain boundary width δ. The solution of this strong form problem can be obtained based on the following equations:

$$f(\bar{\eta}) = f(\eta_0) + \frac{\sqrt{2r(\eta_0)g(\eta_0)}}{\alpha/\sqrt{\beta p}}, \tag{3.44}$$

$$x = \int_{\eta_0}^{\eta} \frac{1}{\zeta(\eta)}\, \mathrm{d}\eta, \tag{3.45}$$

$$\theta = \int_{\eta_0}^{\eta} \frac{\chi(\eta)}{\zeta(\eta)}\, \mathrm{d}\eta, \tag{3.46}$$

where $\eta_0 \equiv \eta(x = 0)$, and ζ and χ are defined as

$$\zeta(\eta) = \begin{cases} \sqrt{p/q}\left(2r(\eta) - \dfrac{\alpha^2}{\beta p}\dfrac{1}{g(\eta)}\left(f(\bar{\eta}) - f(\eta)\right)^2\right)^{1/2}, & \eta_0 \le \eta \le \bar{\eta} \\ \sqrt{p/q}\left(2r(\eta)\right)^{1/2}, & \bar{\eta} < \eta \le 1 \end{cases}, \tag{3.47}$$

$$\chi(\eta) = \begin{cases} \dfrac{\alpha}{\beta g(\eta)}\left(f(\bar{\eta}) - f(\eta)\right), & \eta_0 \le \eta \le \bar{\eta} \\ 0, & \bar{\eta} < \eta \le 1 \end{cases}. \tag{3.48}$$

From (3.44) – (3.46), we obtain η_0, $\bar{\eta}$, and the grain boundary width $\delta = 2\int_{\eta_0}^{\bar{\eta}} 1/\zeta(\eta)\, \mathrm{d}\eta$, given the misorientation $\Delta\theta = 2\int_{\eta_0}^{\bar{\eta}} \chi(\eta)/\zeta(\eta)\, \mathrm{d}\eta$. Additionally, from (3.44), the condition $f(\bar{\eta}) \le f(1)$ leads to the following constraints on model constants:

$$\alpha/\sqrt{\beta p} \geq \max_{\eta_0 \in [0,1]} \frac{\sqrt{2r(\eta_0)g(\eta_0)}}{f(1) - f(\eta_0)}. \tag{3.49}$$

Table 3.1 lists the considered model functions and constants. The model constants are calibrated against the experimental data from[96, 97]. Set I is composed of typical model functions in quadratic form[68] and allows to fit the Read – Shockley type relation between GB energy and misorientation as shown in Figure 3.4(a). However, the width of the diffuse GB δ linearly decreases as the misorientation $\Delta\theta$ increases as shown in Figure 3.4(b) – (d). This indicates that the domain discretization should be much refined to ensure regularized solutions that contain an arbitrary level of misorientation. Also, note that Figure 3.4(c) and (d) show highly diffusive phase field compared to the GB width δ. In Set II, motivated by Abrivard et al.[90], $g(\eta)$ is modified such that $g \in [0.01, 1.0]$. As shown in Figure 3.5, this choice yields less decreasing GB width over $\Delta\theta$, which is more favorable in terms of regularization than Set I. However, η remains highly diffusive as $r(\eta)$ is unchanged.

To remedy the diffusive behavior of phase field, consider a linear form $r(\eta) = |1 - \eta|$ (Set III), motivated by Geelen et al.[91]. Also, the following nonstandard quasi-linear (QL) function (see Figure 3.6) introduced in Geelen et al.[91] is adopted for $f(\eta)$.

$$f(\eta) = \frac{\eta}{\eta + m(1 - \eta)}, \tag{3.50}$$

where $m \geq 1$ is a constant. The benefit of using QL function in the coupled Correrat-phase field approach is twofold. First, it leads to a similar $f(\eta)$ vs η profile to the function $f(\eta) = -2(\log(1 - \eta) + \eta)$ specifically designed to yield the Read-Shockley relation in Kobayashi et

al.[58], but the QL function maintains $f(\eta) \in [0,1]$ while the logarithmic function $f(\eta) \in [0,\infty]$ which requires a numerical treatment for implementation.

Second, the QL function has much less strict condition from Eq. (3.49) than polynomial $f(\eta)$. As described in (3.16) and (3.19), the model constants can be written as

$$\alpha \equiv E_\theta \ell_\alpha, \qquad \beta \equiv E_\theta \ell_\beta^2, \tag{3.51}$$

where E_θ, ℓ_α, and ℓ_β are reference Cosserat energy density, length scale associated with the linear Cosserat energy, and

$$p = E_\eta, \qquad q = E_\eta \ell_\eta^2, \tag{3.52}$$

where E_η and ℓ_η are reference Cosserat energy density and phase field length scale. Then, (3.49) becomes

$$\frac{\ell_\alpha}{\ell_\beta} \geq \bar{c} \max_{\eta_0 \in [0,1]} \mathcal{F}(\eta_0), \tag{3.53}$$

where $\bar{c} = \sqrt{E_\eta / E_\theta}$ and $\mathcal{F}(\eta_0) = \sqrt{2r(\eta_0)g(\eta_0)}/\big(f(1) - f(\eta_0)\big)$.

Note that a larger ℓ_α/ℓ_β ratio leads to a more localized grain boundary (see Section 3.1), so selecting a too large ℓ_α/ℓ_β ratio should be avoided in order to obtain a well-regularized solution. A quadratic $f(\eta)$ paired with the linear $r(\eta)$ requires $\ell_\alpha/\ell_\beta \geq 22\bar{c}$ as shown in Figure 3.7, limiting ℓ_α/ℓ_β to a large number. A quasi-linear $f(\eta)$ paired with the linear $r(\eta)$ as employed for Set III relieves the restriction to $\ell_\alpha/\ell_\beta \geq 1.8\bar{c}$ as shown in Figure 3.7 which is a more favorable

condition. Figure 3.8(c) and (d) show that the phase field from Set III is not as diffusive as the one from Set II (Figure 3.5(c) and(d)) while Figure 3.8(b) – (d) shows that Set III maintains relatively stable grain boundary widths for a wide range of $\Delta\theta$ compared to Set I (Figure 3.4 (b) – (d)). Also, as shown in Figure 3.8(a), a reasonable physical GB energy profile is obtained by Set III.

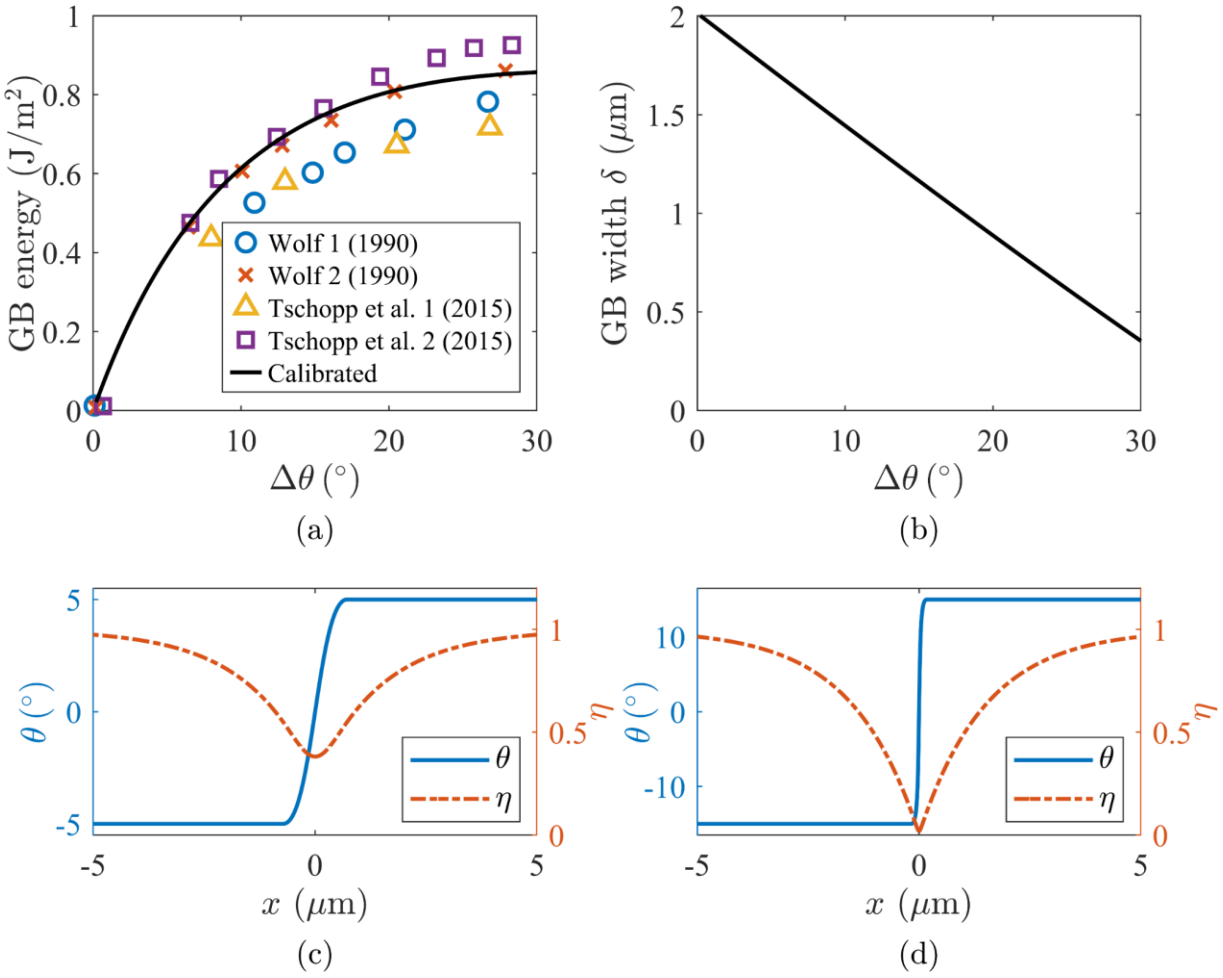

Figure 3.4. Grain boundary properties from Set I. (a) GB energy vs misorientation, (b) GB width vs misorientation, (c) θ and η distribution for $\Delta\theta = 10°$, (d) θ and η distribution for $\Delta\theta = 30°$.

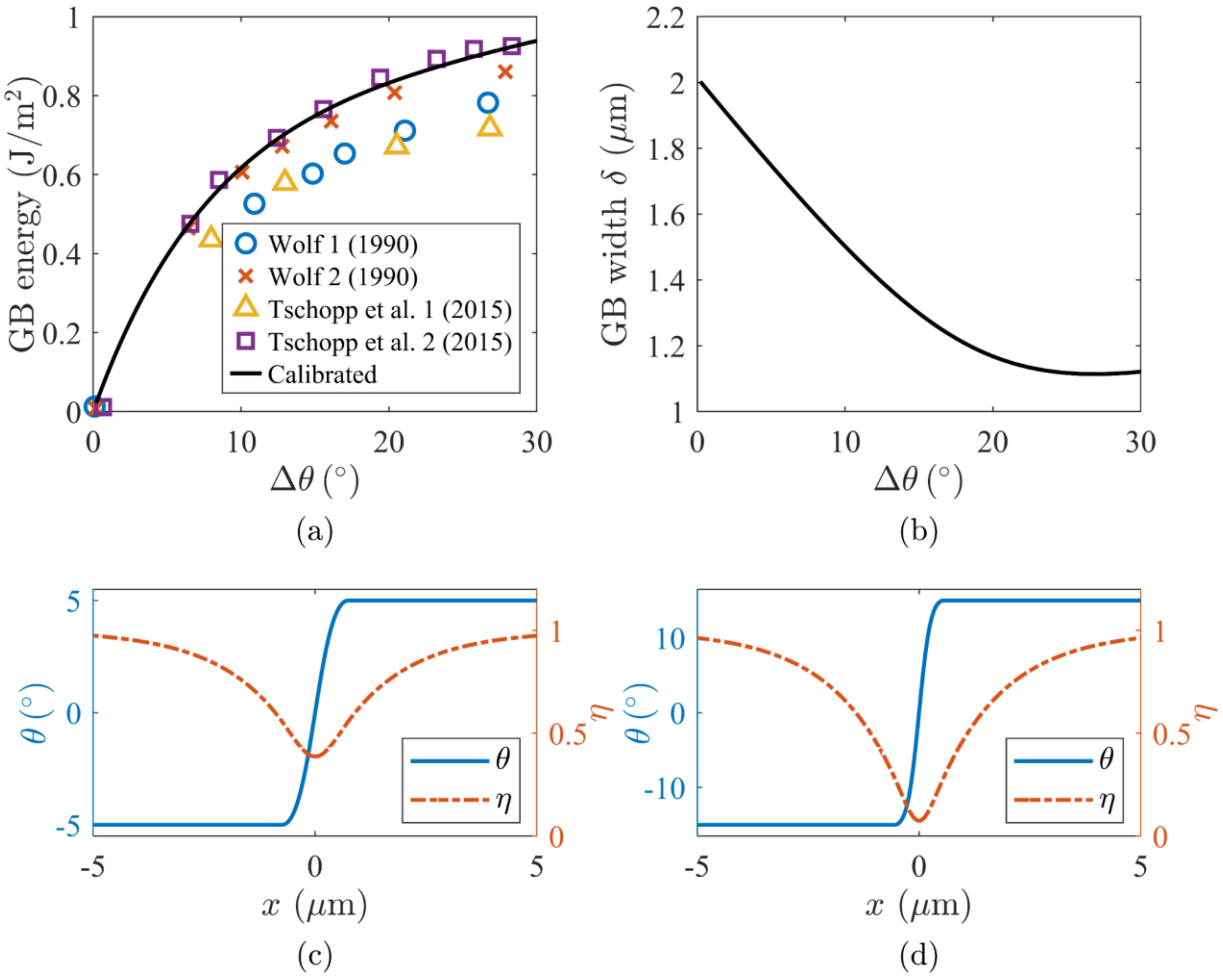

Figure 3.5. Grain boundary properties from Set II. (a) GB energy vs misorientation, (b) GB width vs misorientation, (c) θ and η distribution for $\Delta\theta = 10°$, (d) θ and η distribution for $\Delta\theta = 30°$.

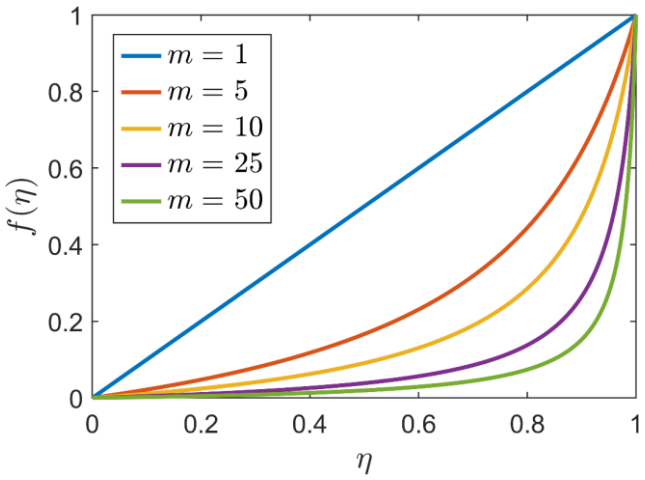

Figure 3.6. Quasi-linear energy correction functions

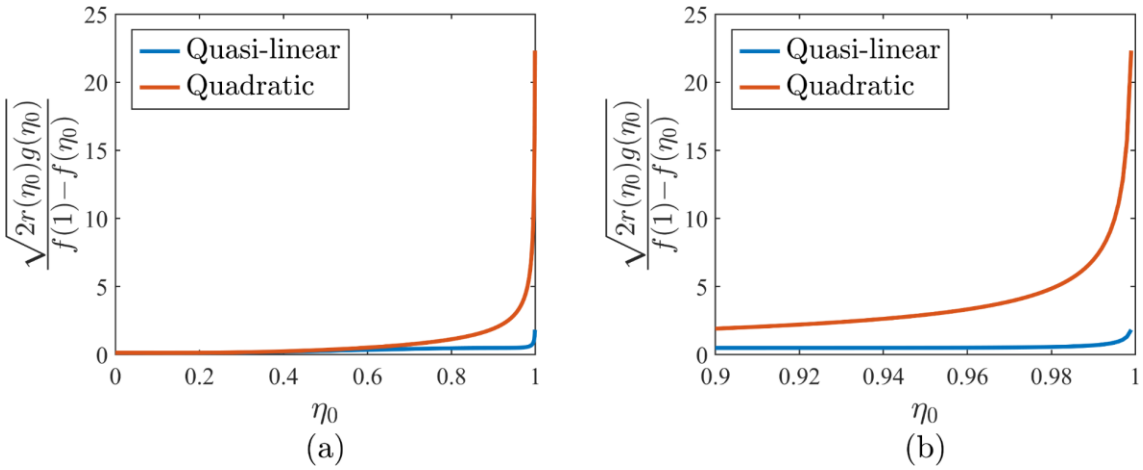

Figure 3.7. $\mathcal{F}(\eta_0)$ vs η_0 profiles for the quasi-linear and quadratic energy correction functions $f(\eta)$ in (a) and a magnified plot shown in (b).

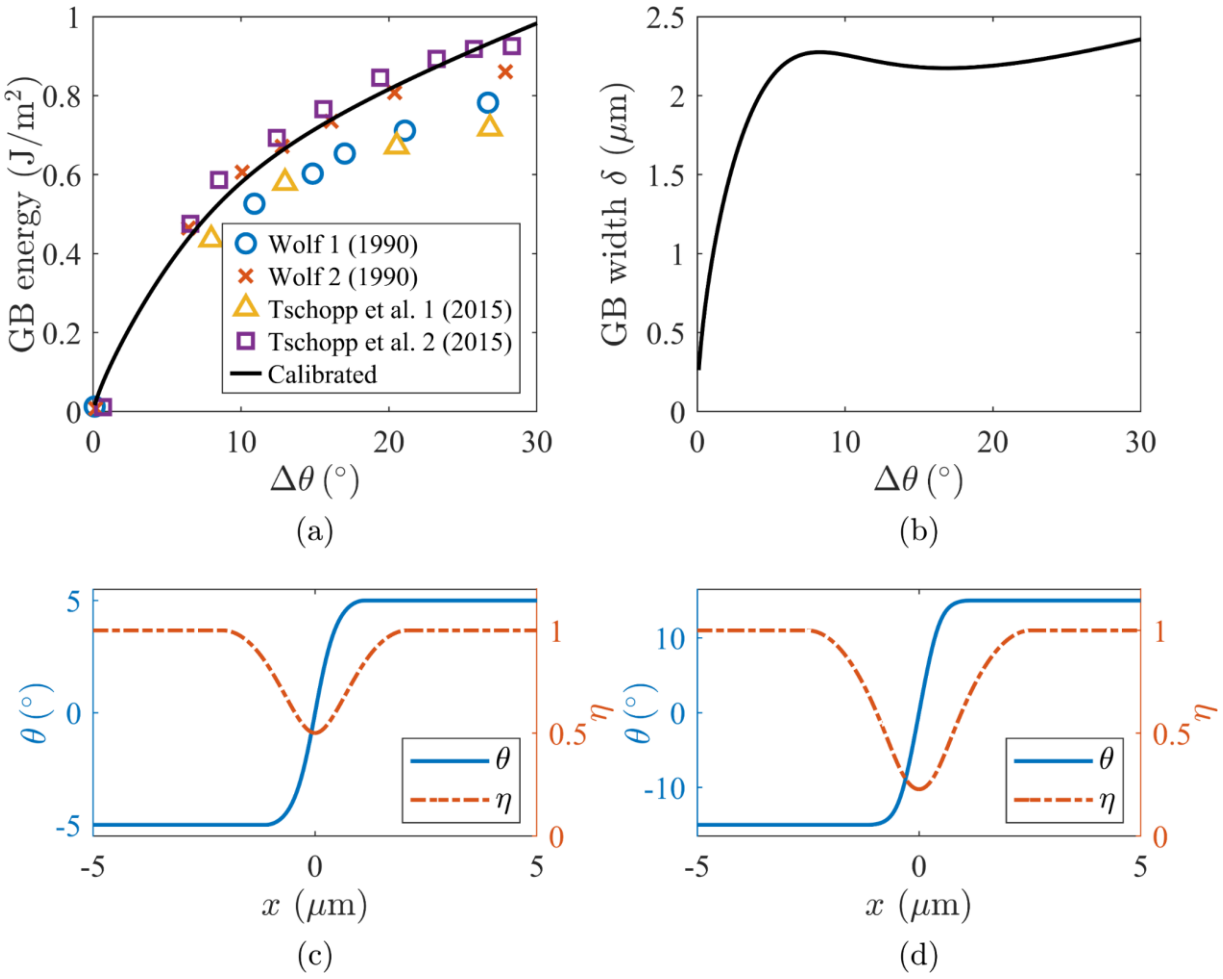

Figure 3.8. Grain boundary properties from Set III. (a) GB energy vs misorientation, (b) GB width vs misorientation, (c) θ and η distribution for $\Delta\theta = 10°$, (d) θ and η distribution for $\Delta\theta = 30°$.

Table 3.1. Lists of model functions and constants

Set I	Set II	Set III
Model functions	Model functions	Model functions
$r = (1-\eta)^2/2$	$r = (1-\eta)^2/2$	$r = \lvert 1-\eta \rvert$
$f = \eta^2$	$f = \eta^2$	$f = \eta/\big(\eta + 25(1-\eta)\big)$
$g = \eta^2$	$g = 0.99\eta^2 + 0.01$	$g = 0.99\eta^4 + 0.01$
Model constants	Model constants	Model constants
$\alpha = 1.5\sqrt{\beta p}$	$\alpha = 1.5\sqrt{\beta p}$	$\alpha = 1.85\sqrt{\beta p}$
$\beta = E_\theta \ell_\beta^2$	$\beta = E_\theta \ell_\beta^2$	$\beta = E_\theta \ell_\beta^2$
$p = E_\eta$	$p = E_\eta$	$p = E_\eta$
$q = E_\eta \ell_\eta^2$	$q = E_\eta \ell_\eta^2$	$q = E_\eta \ell_\eta^2$
$E_\theta = 114.8$ MPa	$E_\theta = 114.8$ MPa	$E_\theta = 27.5$ MPa
$E_\eta = 0.005 E_\theta$	$E_\eta = 0.005 E_\theta$	$E_\eta = 0.01 E_\theta$
$\ell_\beta = 0.5$ μm	$\ell_\beta = 0.5$ μm	$\ell_\beta = 2$ μm
$\ell_\eta = 1.5$ μm	$\ell_\eta = 1.5$ μm	$\ell_\eta = 1.75$ μm

Acknowledgments

A portion of this chapter has been accepted for publication in Baek, J., Chen, J. S., Tupek, M., Beckwith, F., & Fang, H. E. "A Duality-based Coupling of Cosserat Crystal Plasticity and Phase Field Theories for Modeling Grain Refinement", International Journal for Numerical Methods in Engineering. The dissertation author was the primary investigator of this material.

Chapter 4

A duality-based Formulation of Coupled Cosserat Crystal Plasticity – Phase Field

To address the issue of high parameter sensitivity in the classical penalty-based Cosserat crystal plasticity, a stabilized duality-based formulation in introduced. The kinematic constraints on the displacement-based and lattice orientation-based lattice curvatures were imposed with the energy conjugate couple stress derived in the dualization. An additional least squares stabilization is introduced with the parameter range estimated from the stability analysis to suppress spurious lattice rotation modes.

4.1. Duality-based introduction of the lattice orientation field

In this section, the independent lattice orientation field $\boldsymbol{\theta}$ is introduced based on the duality theory. Let us consider a primal problem that is in equilibrium.

$$\inf_{\substack{\mathbf{u}\in\mathcal{V}\\ \eta\in\mathcal{P}}} \Pi = \frac{1}{2}\int_{\Omega} \varepsilon_{ij}\sigma_{ij}^{c}\,\mathrm{d}\Omega + \underbrace{\int_{\Omega} f(\eta)\alpha\|\nabla\boldsymbol{\varphi}^{e}\| + g(\eta)\frac{\beta}{2}\|\nabla\boldsymbol{\varphi}^{e}\|^{2}\,\mathrm{d}\Omega}_{=A} + \int_{\Omega} pr(\eta) + \frac{q}{2}(\nabla\eta)^{2}\,\mathrm{d}\Omega - \Pi^{ext}(\mathbf{u},\eta), \tag{4.1}$$

where $\Pi^{ext}(\mathbf{u},\eta)$ is the external energy associated with body force and Neumann boundary conditions. The internal energy A associated with the lattice curvature can be represented by its convex conjugate A^{*} with dual variable $\boldsymbol{\lambda}$ as follows:

$$A = \sup_{\boldsymbol{\lambda}} \left\{ \int_{\Omega} \lambda_{ij} \varphi^{e}_{i,j} \, \mathrm{d}\Omega - A^{*} \right\}. \tag{4.2}$$

Also, A^{*} can be obtained by the following definition.

$$A^{*} = \sup_{\boldsymbol{\varphi}^{e}} \left\{ \int_{\Omega} \lambda_{ij} \varphi^{e}_{i,j} \, \mathrm{d}\Omega - A \right\} \tag{4.3}$$

Substituting A in (4.1) into (4.3),

$$A^{*} = \sup_{\boldsymbol{\varphi}^{e}} P = \left\{ \int_{\Omega} \lambda_{ij} \varphi_{i,j} \, \mathrm{d}\Omega - \int_{\Omega} f(\eta)\alpha \|\nabla \boldsymbol{\varphi}^{e}\| + g(\eta) \frac{\beta}{2} \|\nabla \boldsymbol{\varphi}^{e}\|^{2} \, \mathrm{d}\Omega \right\}. \tag{4.4}$$

To obtain the stationary point $\widehat{\boldsymbol{\varphi}}$, consider

$$\delta P = \int_{\Omega} \delta\varphi_{i,j} \lambda_{ij} \, \mathrm{d}\Omega - \int_{\Omega} \delta\varphi_{i,j} \left(\frac{f(\eta)\alpha}{\|\nabla \boldsymbol{\varphi}^{e}\|} + g(\eta)\beta \right) \varphi_{i,j} \, \mathrm{d}\Omega = 0, \tag{4.5}$$

which yields the dual variable $\boldsymbol{\lambda}$ identical to the couple stress $\mathbf{m}$ defined in Eq. (3.28):

$$\lambda_{ij} = m_{ij} = \left(\frac{f(\eta)\alpha}{\|\nabla \widehat{\boldsymbol{\varphi}}\|} + g(\eta)\beta \right) \widehat{\varphi}_{i,j}. \tag{4.6}$$

Let us introduce an independent lattice orientation field $\boldsymbol{\theta} \in \mathcal{T}$ such that it satisfies the following relation:

$$m_{ij} = \left(\frac{f(\eta)\alpha}{\|\nabla\boldsymbol{\theta}\|} + g(\eta)\beta\right)\theta_{i,j}. \tag{4.7}$$

Then, $\hat{\varphi}_{i,j} = \theta_{i,j}$ at the stationary point and Eq. (4.6) becomes

$$A^* = P(\nabla\boldsymbol{\varphi}^e = \nabla\hat{\boldsymbol{\varphi}} = \nabla\theta) = \int_\Omega m_{ij}\theta_{i,j}\,\mathrm{d}\Omega - \int_\Omega f(\eta)\alpha\|\nabla\boldsymbol{\theta}\| + g(\eta)\frac{\beta}{2}\|\nabla\boldsymbol{\theta}\|^2\,\mathrm{d}\Omega. \tag{4.8}$$

By substituting Eq. (4.8) into Eq. (4.2), A reads

$$\begin{aligned} A &= \sup_{\mathbf{m}}\left\{\int_\Omega m_{ij}\varphi_{i,j}\,\mathrm{d}\Omega - \int_\Omega m_{ij}\theta_{i,j}\,\mathrm{d}\Omega + \int_\Omega f(\eta)\alpha\|\nabla\boldsymbol{\theta}\| + g(\eta)\frac{\beta}{2}\|\nabla\boldsymbol{\theta}\|^2\,\mathrm{d}\Omega\right\} \\ &= \sup_{\mathbf{m}}\left\{\int_\Omega f(\eta)\alpha\|\nabla\boldsymbol{\theta}\| + g(\eta)\frac{\beta}{2}\|\nabla\boldsymbol{\theta}\|^2\,\mathrm{d}\Omega - \int_\Omega m_{ij}\left(\theta_{i,j} - \varphi^e_{i,j}\right)\mathrm{d}\Omega\right\} \\ &= \sup_{\boldsymbol{\theta}\in\mathcal{T}}\left\{\int_\Omega f(\eta)\alpha\|\nabla\boldsymbol{\theta}\| + g(\eta)\frac{\beta}{2}\|\nabla\boldsymbol{\theta}\|^2\,\mathrm{d}\Omega - \int_\Omega m_{ij}(\boldsymbol{\theta})\left(\theta_{i,j} - \varphi^e_{i,j}\right)\mathrm{d}\Omega\right\}. \end{aligned} \tag{4.9}$$

The Substitution of Eq. (4.9) into Eq. (4.1) ends the derivation.

$$\begin{aligned} &\inf_{\substack{\mathbf{u}\in\mathcal{V}\\ \eta\in\mathcal{P}}}\sup_{\boldsymbol{\theta}\in\mathcal{T}}\Pi(\mathbf{u},\boldsymbol{\theta},\eta) \\ &\qquad= \frac{1}{2}\int_\Omega \varepsilon_{ij}\sigma^c_{ij}\,\mathrm{d}\Omega + \int_\Omega f(\eta)\alpha\|\nabla\boldsymbol{\theta}\| + g(\eta)\frac{\beta}{2}\|\nabla\boldsymbol{\theta}\|^2\,\mathrm{d}\Omega \\ &\qquad- \int_\Omega m_{ij}(\boldsymbol{\theta})\left(\theta_{i,j} - \varphi^e_{i,j}\right)\mathrm{d}\Omega + \int_\Omega pr(\eta) + \frac{q}{2}(\nabla\eta)^2\,\mathrm{d}\Omega - \Pi^{ext}(\mathbf{u},\eta), \end{aligned} \tag{4.10}$$

with the energy conjugate stress $m_{ij}(\boldsymbol{\theta})$ defined in Eq. (4.7).

Note that Eq. (4.10) contains $\varphi^{\mathrm{e}}_{i,j} = -\frac{1}{2}\epsilon_{ikl}\left(e_{kl,j} - e^p_{kl,j}\right)$. To avoid taking gradients of $\mathbf{e}^p$, integration by parts is applied to $\int_\Omega m_{ij}\left(\theta_{i,j} - \varphi^e_{i,j}\right)\mathrm{d}\Omega$ as follows:

$$\Pi = \frac{1}{2}\int_{\Omega} \varepsilon_{ij}\sigma_{ij}^{c}\,\mathrm{d}\Omega + \int_{\Omega} f_{\alpha}(\eta)\alpha\|\nabla\boldsymbol{\theta}\| + f_{\beta}(\eta)\frac{\beta}{2}\|\nabla\boldsymbol{\theta}\|^{2}\,\mathrm{d}\Omega + \int_{\Omega} m_{ij,j}(\theta_i - \varphi_i^e)\,\mathrm{d}\Omega$$
$$- \int_{\partial\Omega} m_{ij}n_j(\theta_i - \varphi_i^e)\,\mathrm{d}\Gamma + \int_{\Omega} pr(\eta) + \frac{q}{2}(\nabla\eta)^2\,\mathrm{d}\Omega - \Pi^{ext}(\mathbf{u},\eta). \tag{4.11}$$

Remark 1. In (4.4), since the kinematic compatibility is imposed on the gradient of $\boldsymbol{\theta}$ and $\boldsymbol{\varphi}^e$, spurious rigid lattice rotation modes can exist in $\boldsymbol{\theta}$ field. That is, arbitrary constant field in θ_i does not contribute to Π unless Dirichlet BCs on lattice orientation are introduced. In general cases, a least-squares stabilization can be considered as follows:

$$\Pi = \frac{1}{2}\int_{\Omega} \varepsilon_{ij}\sigma_{ij}^{c}\,\mathrm{d}\Omega + \int_{\Omega} f_{\alpha}(\eta)\alpha\|\nabla\boldsymbol{\theta}\| + f_{\beta}(\eta)\frac{\beta}{2}\|\nabla\boldsymbol{\theta}\|^{2}\,\mathrm{d}\Omega + \int_{\Omega} m_{ij,j}(\theta_i - \varphi_i^e)\,\mathrm{d}\Omega$$
$$- \int_{\partial\Omega} m_{ij}n_j(\theta_i - \varphi_i^e)\,\mathrm{d}\Gamma + 2\mu_c\int_{\Omega}(\theta_i - \varphi_i^e)(\theta_i - \varphi_i^e)\,\mathrm{d}\Omega \tag{4.12}$$
$$+ \int_{\Omega} pr(\eta) + \frac{q}{2}(\nabla\eta)^2\,\mathrm{d}\Omega - \Pi^{ext}(\mathbf{u},\eta),$$

where μ_c is a stabilization parameter. The new term $2\mu_c\int_{\Omega}(\theta_i - \varphi_i^e)(\theta_i - \varphi_i^e)\,\mathrm{d}\Omega$ has the same form as the penalty term in Eq. (3.35), but the role is completely different. The term is used in (4.12) only to remove the spurious oscillation. Thus, the acceptable parameter range is much wider than the penalty-based approach (see Section 6.3.2 for an example). A stability analysis is performed in Section 6.2 to obtain the suitable range of the stabilization parameter μ_c. The spurious rigid lattice rotation modes can alternatively be suppressed by a strong imposition of the kinematic constraint $\boldsymbol{\theta} = \boldsymbol{\varphi}^e$ as a boundary condition. See Appendix B for details.

The set of Euler-Lagrangian equations derived from Eq. (4.11) is as follows:

$$\begin{aligned} \sigma_{ij,j} + b_i &= 0 \quad \text{in} \quad \Omega \times]0,T[\\ \pi_{i,i}^{\nabla\eta} - \hat{\pi}^{\eta} &= \mu^{\eta}\dot{\eta} \quad \text{in} \quad \Omega \times]0,T[\\ \theta_{i,j} &= \varphi_{i,j}^{e} \quad \text{in} \quad \Omega \times]0,T[\end{aligned} \tag{4.13}$$

with the boundary and initial conditions

$$\begin{aligned} u_i &= g_i \quad \text{on} \quad \partial\Omega^{g_i} \times]0,T[\\ \sigma_{ij}n_j &= h_i \quad \text{on} \quad \partial\Omega^{h_i} \times]0,T[\\ \varphi_i^e &= \bar{\varphi}_i \quad \text{on} \quad \partial\Omega^{\bar{\varphi}_i} \times]0,T[\\ m_{ij}n_j &= \bar{c}_i \quad \text{on} \quad \partial\Omega^{c_i} \times]0,T[\\ \eta &= \bar{\eta} \quad \text{on} \quad \partial\Omega^{\bar{\eta}} \times]0,T[\\ \pi_i^{\nabla\eta} n_i &= \bar{\pi} \quad \text{on} \quad \partial\Omega^{\bar{\pi}} \times]0,T[\\ \eta(t=0) &= \eta_0 \quad \text{in} \quad \Omega \end{aligned} \tag{4.14}$$

and the stresses

$$\begin{aligned} \sigma_{ij} &= \sigma_{ij}^c + \sigma_{ij}^a \\ \sigma_{ij}^c &= C_{ijkl}\varepsilon_{kl}^e \\ \sigma_{ij}^a &= \frac{1}{2}\epsilon_{ijk}m_{kl,l} \\ m_{ij} &= \left(\frac{f(\eta)\alpha}{\|\nabla\boldsymbol{\theta}\|} + g(\eta)\beta\right)\theta_{i,j} \\ \hat{\pi}^{\eta} &= pr_{,\eta} + \frac{\alpha f_{,\eta}}{\|\nabla\boldsymbol{\theta}\|}\theta_{i,j}\varphi_{i,j}^e + \frac{\beta g_{,\eta}}{2}\theta_{i,j}\left(2\varphi_{i,j}^e - \theta_{i,j}\right) \\ \pi_i^{\nabla\eta} &= q\eta_{,i}. \end{aligned} \tag{4.15}$$

The last equation in (4.13) is derived from

$$\int_{\Omega} \delta\theta_{k,l}\frac{\partial m_{ij}}{\partial\theta_{k,l}}\left(\theta_{i,j} - \varphi_{i,j}^e\right)\mathrm{d}\Omega = 0 \;\; \forall\, \delta\theta_{k,l}, \tag{4.16}$$

with $\partial m_{ij}/\partial\theta_{k,l} \neq 0$ for general cases.

4.2. Galerkin formulation

The weak form of Eq. (4.13) is to find $\mathbf{u} \in H^1$ with $u_i = g_i$ on $\partial\Omega^{g_i}$ and $\varphi_i^e = \bar{\varphi}_i$ on $\partial\Omega^{\bar{\varphi}_i}$, $\boldsymbol{\theta} \in H^2$ with $\theta_i = \bar{\varphi}_i$ on $\partial\Omega^{\bar{\varphi}_i}$, and $\eta \in H^1$ with $\eta = \bar{\eta}$ on $\partial\Omega^{\bar{\eta}}$, such that

$$\begin{aligned}
&\int_\Omega \delta u_{i,j}\sigma_{ij}^c \,\mathrm{d}\Omega + \int_\Omega \delta\theta_{i,j} m_{ij} \,\mathrm{d}\Omega + \int_\Omega \delta\theta_i m_{ij,j} \,\mathrm{d}\Omega + \int_\Omega \delta u_{i,j} \frac{1}{2}\epsilon_{ijk} m_{kl,l} \,\mathrm{d}\Omega \\
&\quad + \int_\Omega \delta m_{ij,j}(\theta_i - \varphi_i^e) \,\mathrm{d}\Omega - \int_{\partial\Omega^{c_i}} \delta\theta_i m_{ij} n_j \,\mathrm{d}\Gamma \\
&\quad - \int_{\partial\Omega^{c_i}} \delta u_{i,j} \frac{1}{2}\epsilon_{ijk} m_{kl} n_l \,\mathrm{d}\Gamma - \int_{\partial\Omega^{c_i}} \delta m_{ij} n_j (\theta_i - \varphi_i^e) \,\mathrm{d}\Gamma \\
&\quad + 4\mu_c \int_\Omega \delta\theta_i (\theta_i - \varphi_i^e) \,\mathrm{d}\Omega + 4\mu_c \int_\Omega \delta u_{i,j} \frac{1}{2}\epsilon_{ijk}(\theta_k - \varphi_k^e) \,\mathrm{d}\Omega \\
&\quad + \int_\Omega \delta\eta_{,i} \pi_i^{\nabla\eta} \,\mathrm{d}\Omega + \int_\Omega \delta\eta \pi^\eta \,\mathrm{d}\Omega + \int_\Omega \delta\eta \mu^\eta \dot{\eta} \,\mathrm{d}\Omega \\
&= \int_\Omega \delta u_i b_i \,\mathrm{d}\Omega + \int_{\partial\Omega^{h_i}} \delta u_i h_i \,\mathrm{d}\Gamma - \int_{\partial\Omega^{c_i}} \delta u_{i,j} \frac{1}{2}\epsilon_{ijk}\bar{c}_i \,\mathrm{d}\Gamma + \int_{\partial\Omega^{\bar{\pi}}} \delta\eta\bar{\pi} \,\mathrm{d}\Gamma,
\end{aligned} \tag{4.17}$$

for all $\delta\mathbf{u} \in H^1$ with $\delta u_i = 0$ on $\partial\Omega^{g_i}$ and $\delta\varphi_i^e = 0$ on $\partial\Omega^{\bar{\varphi}_i}$, $\delta\boldsymbol{\theta} \in H^2$ with $\delta\theta_i = 0$ on $\partial\Omega^{\bar{\varphi}_i}$, and $\delta\eta \in H^1$ with $\delta\eta = 0$ on $\partial\Omega^{\bar{\eta}}$.

Remark 2. In Eq. (4.17), the Dirichlet boundary condition is applied both to $\boldsymbol{\theta}$ and $\boldsymbol{\varphi}^e$ to remove the spurious rigid lattice rotation as discussed in Remark 1, Section 4.1. In case of $\partial\Omega^{\bar{\varphi}_i} \neq \emptyset$, $\mu_c = 0$ can be applied. Eq. (4.17) assumes that both $\boldsymbol{\theta}$ and $\boldsymbol{\varphi}^e$ are kinematically admissible, i.e., the function spaces are chosen such that $\boldsymbol{\theta} = \bar{\boldsymbol{\varphi}}$ and $\boldsymbol{\varphi}_e = \bar{\boldsymbol{\varphi}}$ on $\partial\Omega^{\bar{\varphi}_i}$ can be strongly imposed. However, kinematic admissibility can be difficult to achieve particularly in the approximation of displacement-based lattice orientation $\boldsymbol{\varphi}^e$, where it is hard to possess the Kronecker delta property in the function space due to $\boldsymbol{\varphi}^p$ in $\boldsymbol{\varphi}^e = \boldsymbol{\varphi} - \boldsymbol{\varphi}^p$. For kinematically *inadmissible* $\boldsymbol{\theta}$ and $\boldsymbol{\varphi}^e$, Nitsche's method can be implemented to impose these boundary conditions by considering additional terms in the potential energy functional of Eq. (4.11) with $\mu_c = 0$ as follows:

$$\begin{aligned}\overline{\Pi} = \Pi &+ \int_{\partial\Omega^{\bar{\varphi}_i}} m_{ij} n_j (\theta_i - \bar{\varphi}_i)\,\mathrm{d}\Gamma - \frac{\kappa^{\bar{\varphi}}}{2}\int_{\partial\Omega^{\bar{\varphi}_i}} (\theta_i - \bar{\varphi}_i)(\theta_i - \bar{\varphi}_i)\,\mathrm{d}\Gamma \\ &- \int_{\partial\Omega^{\bar{\varphi}_i}} m_{ij} n_j (\varphi_i^e - \bar{\varphi}_i)\,\mathrm{d}\Gamma + \frac{\kappa^{\bar{\varphi}}}{2}\int_{\partial\Omega^{\bar{\varphi}_i}} (\varphi_i^e - \bar{\varphi}_i)(\varphi_i^e - \bar{\varphi}_i)\,\mathrm{d}\Gamma \\ &= 0,\end{aligned} \tag{4.18}$$

where $\kappa^{\bar{\varphi}}$ is stabilization parameter. The third and fifth terms of Eq. (4.18) and the Dirichlet boundary portion of the sixth term of Eq. (4.11) are canceled, leading to the following modified weak form.

$$\begin{aligned}&\int_\Omega \delta u_{i,j}\sigma_{ij}^c\,\mathrm{d}\Omega + \int_\Omega \delta\theta_{i,j} m_{ij}\,\mathrm{d}\Omega + \int_\Omega \delta\theta_i m_{ij,j}\,\mathrm{d}\Omega + \int_\Omega \delta u_{i,j}\frac{1}{2}\epsilon_{ijk} m_{kl,l}\,\mathrm{d}\Omega \\ &\quad + \int_\Omega \delta m_{ij,j}(\theta_i - \varphi_i^e)\,\mathrm{d}\Omega - \int_{\partial\Omega^{c_i}} \delta\theta_i m_{ij} n_j\,\mathrm{d}\Gamma \\ &\quad - \int_{\partial\Omega^{c_i}} \delta u_{i,j}\frac{1}{2}\epsilon_{ijk} m_{kl} n_l\,\mathrm{d}\Gamma - \int_{\partial\Omega^{c_i}} \delta m_{ij} n_j(\theta_i - \varphi_i^e)\,\mathrm{d}\Gamma \\ &\quad - \kappa^{\bar{\varphi}}\int_{\partial\Omega^{\bar{\varphi}_i}} \delta u_{i,j}\frac{1}{2}\epsilon_{ijk}\varphi_k^e\,\mathrm{d}\Gamma - \kappa^{\bar{\varphi}}\int_{\partial\Omega^{\bar{\varphi}_i}} \delta\theta_i\theta_i\,\mathrm{d}\Gamma \\ &\quad + 4\mu_c\int_\Omega \delta\theta_i(\theta_i - \varphi_i^e)\,\mathrm{d}\Omega + 4\mu_c\int_\Omega \delta u_{i,j}\frac{1}{2}\epsilon_{ijk}(\theta_k - \varphi_k^e)\,\mathrm{d}\Omega \\ &\quad + \int_\Omega \delta\eta_{,i}\pi_i^{\nabla\eta}\,\mathrm{d}\Omega + \int_\Omega \delta\eta\pi^\eta\,\mathrm{d}\Omega + \int_\Omega \delta\eta\mu^\eta\dot{\eta}\,\mathrm{d}\Omega \\ &= \int_\Omega \delta u_i b_i\,\mathrm{d}\Omega + \int_{\partial\Omega^{h_i}} \delta u_i h_i\,\mathrm{d}\Gamma - \int_{\partial\Omega^{c_i}} \delta u_{i,j}\frac{1}{2}\epsilon_{ijk}\bar{c}_i\,\mathrm{d}\Gamma \\ &\quad - \kappa^{\bar{\varphi}}\int_{\partial\Omega^{\bar{\varphi}_i}} \delta u_{i,j}\frac{1}{2}\epsilon_{ijk}\bar{\varphi}_k\,\mathrm{d}\Gamma - \kappa^{\bar{\varphi}}\int_{\partial\Omega^{\bar{\varphi}_i}} \delta\theta_i\bar{\varphi}_i\,\mathrm{d}\Gamma + \int_{\partial\Omega^{\bar{\pi}}} \delta\eta\bar{\pi}\,\mathrm{d}\Gamma.\end{aligned} \tag{4.19}$$

In this work, the parameter $\kappa^{\bar{\varphi}} = 100\beta/h$ with nodal spacing h is used. Note that, although Nitsche's method is applied, the Lagrange multiplier portions of the method are canceled, which results in a pure penalty method for the imposition of $\bar{\varphi}_i$. Thus, $\kappa^{\bar{\varphi}}$ needs to be sufficiently large. However, it will be shown that this formulation still yields optimal convergence. Finding a more effective way to impose $\bar{\varphi}_i$ will be included in future work.

The corresponding Galerkin formulation corresponding to Eq. (4.17) is obtained by replacing $\mathbf{u}$, $\boldsymbol{\theta}$, and η with the approximations $\mathbf{u}^h$, $\boldsymbol{\theta}^h$, and η^h, respectively.

Acknowledgments

A portion of this chapter has been accepted for publication in Baek, J., Chen, J. S., Tupek, M., Beckwith, F., & Fang, H. E. "A Duality-based Coupling of Cosserat Crystal Plasticity and Phase Field Theories for Modeling Grain Refinement", International Journal for Numerical Methods in Engineering. The dissertation author was the primary investigator of this material.

Chapter 5

Reproducing Kernel Particle Method

A Reproducing Kernel Particle Method is introduced to construct the basic approximation functions for approximating the smooth solution in the kinematic valuables involved in the multi-field variational formulation derived in Chapter 4. The ability of using arbitrary order of monomial basis functions and arbitrary smoothness in the kernel functions is particularly effective in evaluating higher order derivative terms in the crystal plasticity equations.

5.1. Reproducing Kernel Approximation

As the proposed formulation requires $\boldsymbol{\theta}^h \in H^2$, C^1-continuity is also required. For this reason, the reproducing kernel (RK) approximation[98, 99] is used in this work. The RK approximation is particularly suitable since the order of continuity of the approximation is controlled by simply using a kernel function with a desired order of continuity and is independent of the order of basis.

Let us consider a domain Ω discretized by NP nodes with nodal coordinate $\mathbf{X}_I$ with $1 \leq J \leq NP$. The RK approximation $f^h(\mathbf{X})$ of a function $f(\mathbf{X})$ is

$$f^h(\mathbf{X}) = \sum_{J=1}^{NP} \Psi_J(\mathbf{X}) d_J, \tag{5.1}$$

where $\Psi_J(\mathbf{X})$ is RK shape function of node J and d_J is generalized nodal coefficient of node J. The RK shape function $\Psi_J(\mathbf{X})$ is a correction of a kernel function $\Phi_a(\mathbf{X}-\mathbf{X}_J)$ defined on the compact support of node J with support size of a:

$$\Psi_J(\mathbf{X}) = \left\{\sum_{|\boldsymbol{\alpha}|\leq n} (\mathbf{X}-\mathbf{X}_J)^{\boldsymbol{\alpha}} b_{\boldsymbol{\alpha}}(\mathbf{x})\right\}\Phi_a(\mathbf{X}-\mathbf{X}_J), \tag{5.2}$$

where $(\mathbf{X}-\mathbf{X}_J)^{\boldsymbol{\alpha}}$ is a basis function, $\boldsymbol{\alpha} = (\alpha_1, \alpha_2, \ldots, \alpha_d)$ with dimension d, and $|\boldsymbol{\alpha}| \equiv \sum_{i=1}^{d} \alpha_i$. $\mathbf{X}^{\alpha}$ is defined as

$$\mathbf{X}^{\boldsymbol{\alpha}} \equiv X_1^{\alpha_1} \cdot X_2^{\alpha_2} \cdot \ldots \cdot X_d^{\alpha_d} \tag{5.3}$$

The coefficients $b_{\boldsymbol{\alpha}}(\mathbf{X})$ for $|\boldsymbol{\alpha}| \leq n$ are the solutions of the following set of reproducing conditions:

$$\sum_{J=1}^{NP} \Psi_J(\mathbf{X})\mathbf{X}_J^{\boldsymbol{\alpha}} = \mathbf{X}^{\boldsymbol{\alpha}}, \qquad |\boldsymbol{\alpha}| \leq n \tag{5.4}$$

which leads to the explicit form of $\Psi_J(\mathbf{X})$ as follows.

$$\Psi_J(\mathbf{X}) = \mathbf{H}^T(\mathbf{0})\mathbf{M}^{-1}(\mathbf{X})\mathbf{H}(\mathbf{X}-\mathbf{X}_J)\Phi_a(\mathbf{X}-\mathbf{X}_J) \tag{5.5}$$

where $\mathbf{M}(\mathbf{X})$ is moment matrix and $\mathbf{H}(\mathbf{X}-\mathbf{X}_J)$ is the basis vector defined as

$$\mathbf{M}(\mathbf{X}) = \sum_{J=1}^{NP} \mathbf{H}(\mathbf{X}-\mathbf{X}_J)\mathbf{H}^T(\mathbf{X}-\mathbf{X}_J)\Phi_a(\mathbf{X}-\mathbf{X}_J), \tag{5.6}$$

$$\mathbf{H}(\mathbf{X}-\mathbf{X}_J)=\left[1,(X_1-X_{1J}),(X_2-X_{2J}),(X_3-X_{3J}),\cdots,(X_3-X_{3J})^n\right]^T. \tag{5.7}$$

The order of continuity of the RK approximation is determined by the kernel function $\Phi_a(\mathbf{X}-\mathbf{X}_J)$ while the polynomial completeness of the approximation is determined by the basis vector $\mathbf{H}(\mathbf{X}-\mathbf{X}_J)$. Thus, it is straightforward to introduce high order continuity into the approximation space, which makes the RK approximation more appealing to utilize for the formulation proposed in Chapter 4 than the C^0 interpolation-type approximations used in finite element methods.

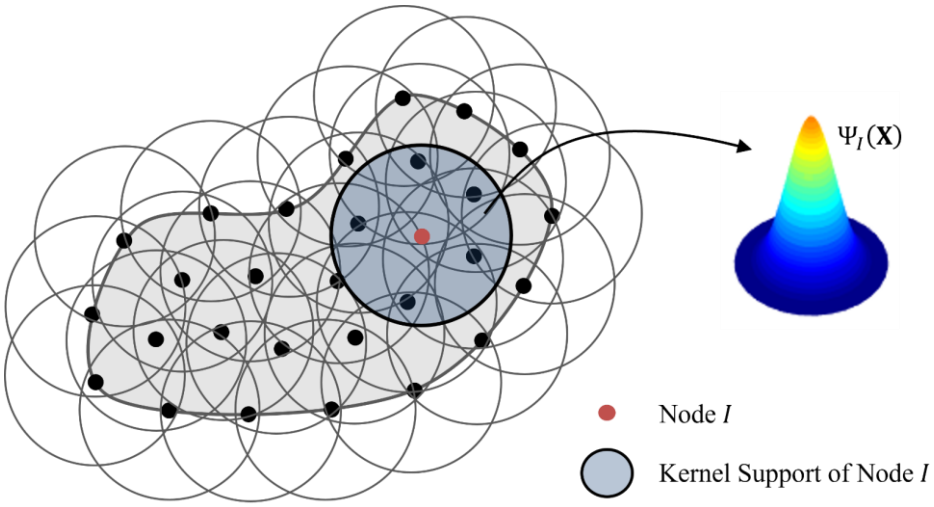

Figure 5.1. Illustration of RK discretization and shape function

Now, consider the following approximations:

$$\mathbf{u}^h(\mathbf{X})=\sum_{J=1}^{NP}\Psi_J^u(\mathbf{X})\mathbf{d}_J^u \tag{5.8}$$

$$\boldsymbol{\theta}^h(\mathbf{X}) = \sum_{J=1}^{NP} \Psi_J^{\theta}(\mathbf{X})\mathbf{d}_J^{\theta} \tag{5.9}$$

$$\eta^h(\mathbf{X}) = \sum_{J=1}^{NP} \Psi_J^{\eta}(\mathbf{X})d_J^{\eta} \tag{5.10}$$

where $\mathbf{d}_J^u = \left[d_{J1}^u \cdots d_{Jd}^u\right]^T$, $\mathbf{d}_J^{\theta} = \left[d_{J1}^{\theta} \cdots d_{J\bar{d}}^{\theta}\right]^T$, and d_J^{η} are the generalized coefficients. In general, it is recommended that a second order or higher basis vector is used for $\boldsymbol{\theta}^h$ to possess the zeroth order or higher polynomial completeness on $\boldsymbol{\theta}_{,ij}^h$ since the proposed formulation and general constitutive equations involve $\nabla^2\mathbf{m}$ which contains $\boldsymbol{\theta}_{,ij}^h$. For $\mathbf{u}^h$, a basis with an order equal to the order of basis for $\boldsymbol{\theta}^h$ could be chosen considering both accuracy and efficiency, since the weak inf-sup stabilization stabilizes an equal-order pair[100]. If higher accuracy of displacement and strain is of interest, a higher order basis can be considered for $\mathbf{u}^h$. For the phase field η^h, the basis order equal to the basis order of other independent variables has widely been used, e.g., an equal order displacement-phase field pair for phase field fracture simulations[91, 101, 102] and an equal order lattice rotation-phase field pair for orientation phase field simulations[68, 103], and stable solutions have been obtained. Similarly, for the proposed method, it has been observed that equal order lattice rotation-phase field pairs are stable. Consequently, equal order displacement-lattice rotation-phase field approximations are considered in this work. The specific orders of basis vectors used for this work are specified in each numerical example.

5.2. Solution Procedure

To solve the proposed formulations, the staggered solution scheme is applied such that, at time $t = t^n$, the equation is first solved for the phase field while the displacement and lattice orientation are fixed. In the next stage, the obtained phase field is fixed and the equation is solved for the displacement and lattice orientation. This simplifies the implementation of the proposed formulation. In the first stage, the problem states

$$\int_\Omega \delta\eta^h \mu^\eta \dot{\eta}^h \,\mathrm{d}\Omega + \int_\Omega \delta\eta^h_{,i} \pi_i^{\nabla\eta} \,\mathrm{d}\Omega + \int_\Omega \delta\eta^h \pi^\eta \,\mathrm{d}\Omega = \int_{\partial\Omega^{\bar{\pi}}} \delta\eta^h \bar{\pi} \,\mathrm{d}\Gamma \qquad \forall\ \delta\eta^h \in \mathcal{P}^h \subset H^1. \tag{5.11}$$

with given $\mathbf{u}^h$ and θ^h. The backward Euler scheme is employed for the time integration.

The problem of the second stage reads

$$\begin{aligned} &\int_\Omega \delta u^h_{i,j} \sigma^c_{ij} \,\mathrm{d}\Omega + \int_\Omega \delta u^h_{i,j} \frac{1}{2} \epsilon_{ijk} m_{kl,l} \,\mathrm{d}\Omega - \int_{\partial\Omega^{c_i}} \delta u^h_{i,j} \frac{1}{2} \epsilon_{ijk} m_{kl} n_l \,\mathrm{d}\Gamma \\ &\quad + 4\mu_c \int_\Omega \delta u^h_{i,j} \frac{1}{2} \epsilon_{ijk} \left(\theta^h_k - \varphi^e_k\right) \mathrm{d}\Omega \\ &= \int_\Omega \delta u^h_i b_i \,\mathrm{d}\Omega + \int_{\partial\Omega^{h_i}} \delta u^h_i h_i \,\mathrm{d}\Gamma - \int_{\partial\Omega^{c_i}} \delta u^h_{i,j} \frac{1}{2} \epsilon_{ijk} \bar{c}_i \,\mathrm{d}\Gamma \\ &\qquad \forall\ \delta\mathbf{u}^h \in \mathcal{V}^h \in H^1, \end{aligned} \tag{5.12}$$

$$\int_{\Omega} \delta\theta^h_{i,j} m_{ij}\, \mathrm{d}\Omega + \int_{\Omega} \delta\theta^h_i m_{ij,j}\, \mathrm{d}\Omega + \int_{\Omega} \left(\delta\theta^h_{k,l} \frac{\partial m_{ij,j}}{\partial \theta^h_{k,l}} + \delta\theta^h_{k,ls} \frac{\partial m_{ij,j}}{\partial \theta^h_{k,ls}} \right) \left(\theta^h_i - \varphi^e_i\right) \mathrm{d}\Omega$$
$$- \int_{\partial\Omega^{c_i}} \delta\theta^h_i m_{ij} n_j\, \mathrm{d}\Gamma - \int_{\partial\Omega^{c_i}} \delta\theta^h_{k,l} \frac{\partial m_{ij}}{\partial \theta^h_{k,l}} n_j \left(\theta^h_i - \varphi^e_i\right) \mathrm{d}\Gamma \tag{5.13}$$
$$+ 4\mu_c \int_{\Omega} \delta\theta_i (\theta_i - \varphi^e_i)\, \mathrm{d}\Omega = 0$$
$$\forall\, \delta\theta^h \in \mathcal{T}^h \in H^2,$$

with given η^h. The Newton-Raphson algorithm is implemented to solve Eqs. (5.11), (5.12), and (5.13).

5.3. Matrix Equations

The matrix equations for the proposed formulation are provided for two-dimension. Let us first define the following vectors:

$$\mathbf{e} = [u_{1,1} \quad u_{2,2} \quad u_{1,2} \quad u_{2,1}]^T \tag{5.14}$$

$$\boldsymbol{\kappa} = [\theta_{,1} \quad \theta_{,2}\,]^T \tag{5.15}$$

$$\mathbf{q} = [\theta_{,11} \quad \theta_{,22} \quad \theta_{,12} \quad \theta_{,21}]^T \tag{5.16}$$

$$\boldsymbol{\epsilon} = [0 \quad 0 \quad 1 \quad -1]^T \tag{5.17}$$

Next, we have the stress $\boldsymbol{\sigma}$ as follows:

$$\boldsymbol{\sigma} = \mathbf{D}\mathbf{e}^e + \frac{1}{2}\boldsymbol{\epsilon}\left(c m_{k,k} + 4\mu_c(\theta - \varphi)\right) = \widehat{\mathbf{D}}\mathbf{e}^e + \frac{1}{2}\boldsymbol{\epsilon}\left(c m_{k,k} + 4\mu_c\theta\right) \tag{5.18}$$

where

$$\mathbf{D} = \begin{bmatrix} 2\mu + \lambda & \lambda & 0 & 0 \\ \lambda & 2\mu + \lambda & 0 & 0 \\ 0 & 0 & \mu & 0 \\ 0 & 0 & 0 & \mu \end{bmatrix} \tag{5.19}$$

and

$$\widehat{\mathbf{D}} = \mathbf{D} + \mu_c \boldsymbol{\epsilon}\boldsymbol{\epsilon}^T. \tag{5.20}$$

The couple stress $\mathbf{m}$ is

$$\mathbf{m} = \left(\frac{\alpha}{|\nabla\boldsymbol{\theta}|} + \beta\right)\boldsymbol{\kappa} = B\boldsymbol{\kappa} \tag{5.21}$$

where

$$B = \frac{\alpha}{|\nabla\boldsymbol{\theta}|} + \beta \tag{5.22}$$

By substituting Eqs. (5.8), (5.9), and (5.10) into (5.11), (5.12), and (5.13),

$$\begin{aligned} \mathbf{f}_I^{int,u} &= \int_\Omega \mathbf{B}_I^{u^T}\boldsymbol{\sigma}\,\mathrm{d}\Omega - \int_{\partial\Omega^{c_i}} \mathbf{B}_I^{u^T}\frac{1}{2}\boldsymbol{\epsilon}\mathbf{n}^T\mathbf{m}\;\mathrm{d}\Gamma \\ &= \int_\Omega \mathbf{N}_I^{u^T}\mathbf{b}\,\mathrm{d}\Omega + \int_{\partial\Omega^{h_i}} \mathbf{N}_I^{u^T}\mathbf{h}\,\mathrm{d}\Gamma - \int_{\partial\Omega^{c_i}} \mathbf{B}_I^{u^T}\frac{1}{2}\boldsymbol{\epsilon}\mathbf{n}^T\bar{\mathbf{c}}\,\mathrm{d}\Gamma \;= \mathbf{f}_I^{ext,u} \\ &\forall\, I \in \mathcal{S}, \end{aligned} \tag{5.23}$$

$$f_I^{int,\theta} = \int_\Omega \mathbf{B}_I^{\theta^T}\mathbf{m}\,\mathrm{d}\Omega + \int_\Omega \Psi_I^{\theta^T} m_{j,j}\,\mathrm{d}\Omega + \int_\Omega \mathbf{W}_I^{\theta^T}(\theta-\varphi)\,\mathrm{d}\Omega - \int_{\partial\Omega^{c_i}} \Psi_I^{\theta^T}\mathbf{n}^T\mathbf{m}\,\mathrm{d}\Gamma - \int_{\partial\Omega^{c_i}} \mathbf{B}_I^{\theta^T}\mathbf{C}^T\mathbf{n}(\theta-\varphi)\,\mathrm{d}\Gamma = 0 \quad (5.24)$$

$$\forall\, I \in \mathcal{S},$$

$$f_I^{int,\eta} = \int_\Omega \Psi_I^{\eta^T}\mu^\eta\dot{\eta}^h\,\mathrm{d}\Omega + \int_\Omega \mathbf{B}_I^{\eta^T}\boldsymbol{\pi}^{\nabla\eta}\,\mathrm{d}\Omega + \int_\Omega \Psi_I^{\eta^T}\pi^\eta\,\mathrm{d}\Omega = \int_{\partial\Omega^{\bar{\pi}}} \Psi_I^{\eta^T}\bar{\pi}\,\mathrm{d}\Gamma = f_I^{ext,\eta} \quad (5.25)$$

$$\forall\, I \in \mathcal{S}.$$

where

$$\mathbf{C} = B\mathbf{I} - \frac{\alpha}{|\nabla\boldsymbol{\theta}|^3}\boldsymbol{\kappa}\boldsymbol{\kappa}^T \quad (5.26)$$

$$\mathbf{N}_I^u = \mathbf{N}_I^u(\mathbf{X}) = \begin{bmatrix} \Psi_I^u(\mathbf{X}) & 0 \\ 0 & \Psi_I^u(\mathbf{X}) \end{bmatrix} \quad (5.27)$$

$$\mathbf{B}_I^u = \mathbf{B}_I^u(\mathbf{X}) = \begin{bmatrix} \Psi_{I,1}^u(\mathbf{X}) & 0 \\ 0 & \Psi_{I,2}^u(\mathbf{X}) \\ \Psi_{I,2}^u(\mathbf{X}) & 0 \\ 0 & \Psi_{I,1}^u(\mathbf{X}) \end{bmatrix} \quad (5.28)$$

$$\mathbf{B}_I^\theta = \mathbf{B}_I^\theta(\mathbf{X}) = \begin{bmatrix} \Psi_{I,1}^\theta(\mathbf{X}) \\ \Psi_{I,1}^\theta(\mathbf{X}) \end{bmatrix} \quad (5.29)$$

$$\mathbf{B}_I^\eta = \mathbf{B}_I^\eta(\mathbf{X}) = \begin{bmatrix} \Psi_{I,1}^\eta(\mathbf{X}) \\ \Psi_{I,1}^\eta(\mathbf{X}) \end{bmatrix} \quad (5.30)$$

$$\mathbf{W}_I^\theta = 4\mu_c\mathbf{N}_I^\theta + c\left(\mathbf{q}^T\mathbf{T}^T\mathbf{B}_I^\theta + \mathbf{H}\mathbf{Q}_I^\theta\right) \quad (5.31)$$

$$\mathbf{Q}_I^{\theta} = \mathbf{Q}_I^{\theta}(\mathbf{X}) = \begin{bmatrix} \Psi_{I,11}^{\theta}(\mathbf{X}) \\ \Psi_{I,22}^{\theta}(\mathbf{X}) \\ \Psi_{I,12}^{\theta}(\mathbf{X}) \\ \Psi_{I,21}^{\theta}(\mathbf{X}) \end{bmatrix} \tag{5.32}$$

$$\mathbf{T} = -\frac{\alpha}{|\nabla\boldsymbol{\theta}|^3}\begin{bmatrix} 3\theta_{,1} & \theta_{,1} & \theta_{,2} & \theta_{,2} \\ \theta_{,2} & 3\theta_{,2} & \theta_{,1} & \theta_{,1} \end{bmatrix} + 3\frac{\alpha}{|\nabla\boldsymbol{\theta}|^5}\begin{bmatrix} \theta_{,1}^3 & \theta_{,1}\theta_{,2}^2 & \theta_{,1}^2\theta_{,2} & \theta_{,1}^2\theta_{,2} \\ \theta_{,1}^2\theta_{,2} & \theta_{,2}^3 & \theta_{,1}\theta_{,2}^2 & \theta_{,1}\theta_{,2}^2 \end{bmatrix} \tag{5.33}$$

$$\mathbf{H} = [C_{11} \quad C_{22} \quad C_{21} \quad C_{12}] \tag{5.34}$$

If the Nitsche's method is considered for imposing the Dirichlet boundary condition on the displacement, the following terms are additionally introduced with the stability parameter ζ.

$$\mathbf{f}_I^{EBCu,int,u} = -\int_{\partial\Omega^g} \delta\mathbf{B}_I^{u^T}\widehat{\mathbf{D}}\mathbf{v}\mathbf{u}\,\mathrm{d}\Gamma + \int_{\partial\Omega^g} \mathbf{N}_I^{u^T}[\zeta\mathbf{u} - \mathbf{v}^T\boldsymbol{\sigma}]\,\mathrm{d}\Gamma \tag{5.35}$$

$$\mathbf{f}_I^{EBCu,ext,u} = -\int_{\partial\Omega^g} \delta\mathbf{B}_I^{u^T}\widehat{\mathbf{D}}\mathbf{v}\mathbf{g}^u\,\mathrm{d}\Gamma + \int_{\partial\Omega^g} \mathbf{N}_I^{u^T}\zeta\mathbf{g}\,\mathrm{d}\Gamma \tag{5.36}$$

$$\mathbf{f}_I^{EBCu,int,\theta} = -\int_{\Gamma^g} \mathbf{W}_I^{\theta^T}\frac{1}{2}\boldsymbol{\epsilon}^T\mathbf{v}\mathbf{u}\,\mathrm{d}\Gamma \tag{5.37}$$

$$\mathbf{f}_I^{EBCu,ext,\theta} = -\int_{\Gamma^g} \mathbf{W}_I^{\theta^T}\frac{1}{2}\boldsymbol{\epsilon}^T\mathbf{v}\mathbf{g}^u\,\mathrm{d}\Gamma \tag{5.38}$$

where

$$\mathbf{v} = \begin{bmatrix} n_1 & 0 \\ 0 & n_2 \\ n_2 & 0 \\ 0 & n_1 \end{bmatrix}. \tag{5.39}$$

For the nonlinear iteration, we obtain the following matrix equation by taking the incremental forms of Eqs. (5.23) and (5.24):

$$\begin{bmatrix} \mathbf{K}^{uu} & \mathbf{K}^{u\theta} \\ \mathbf{K}^{\theta u} & \mathbf{K}^{\theta\theta} \end{bmatrix} \begin{bmatrix} \Delta\mathbf{d}^{u} \\ \Delta\mathbf{d}^{\theta} \end{bmatrix} = \begin{bmatrix} \Delta\mathbf{f}^{u} \\ \Delta\mathbf{f}^{\theta} \end{bmatrix} \tag{5.40}$$

where

$$\mathbf{K}_{IJ}^{uu} = \int_{\Omega} \mathbf{B}_{I}^{u^T} \widehat{\mathbf{G}} \widehat{\mathbf{D}} \mathbf{B}_{J}^{u} \, \mathrm{d}\Omega \tag{5.41}$$

$$\mathbf{K}_{IJ}^{u\theta} = \int_{\Omega} \mathbf{B}_{I}^{u^T} \frac{1}{2} \widehat{\mathbf{G}} \boldsymbol{\epsilon} \mathbf{W}_{J}^{\theta} \, \mathrm{d}\Omega - \int_{\partial\Omega^{c_i}} \mathbf{B}_{I}^{u^T} \frac{1}{2} \boldsymbol{\epsilon} \mathbf{n}^T \mathbf{C} \mathbf{B}_{J}^{\theta} \, \mathrm{d}\Gamma \tag{5.42}$$

$$\mathbf{K}_{IJ}^{\theta u} = \int_{\Omega} \mathbf{W}_{I}^{\theta^T} \frac{1}{2} \boldsymbol{\epsilon}^T \bar{\mathbf{G}} \mathbf{B}_{J}^{u} \, \mathrm{d}\Omega - \int_{\partial\Omega^{c_i}} \mathbf{B}_{I}^{\theta^T} \frac{1}{2} \mathbf{C}^T \mathbf{n} \boldsymbol{\epsilon}^T \bar{\mathbf{G}} \mathbf{B}_{J}^{u} \, \mathrm{d}\Gamma \tag{5.43}$$

$$\begin{aligned} \mathbf{K}_{IJ}^{\theta\theta} = & \int_{\Omega} \mathbf{B}_{I}^{\theta^T} \mathbf{C} \mathbf{B}_{J}^{\theta} \, \mathrm{d}\Omega + \int_{\Omega} \left[\mathbf{W}_{I}^{\theta^T} \mathbf{N}_{J}^{\theta} + \mathbf{N}_{I}^{\theta^T} \mathbf{W}_{J}^{\theta} \right] \mathrm{d}\Omega - \int_{\Omega} \mathbf{N}_{I}^{\theta^T} 4\mu_c \mathbf{N}_{J}^{\theta} \, \mathrm{d}\Omega \\ & - \int_{\Omega} \mathbf{W}_{I}^{\theta^T} \frac{1}{4} \boldsymbol{\epsilon}^T \mathbf{G} \boldsymbol{\epsilon} \mathbf{W}_{J}^{\theta} \, \mathrm{d}\Omega + c \int_{\Omega} \bar{\mathbf{K}}_{IJ}^{\theta\theta} (\theta - \varphi) \, \mathrm{d}\Omega \\ & - c \int_{\Gamma} \mathbf{B}_{I}^{\theta^T} (\theta - \varphi) \mathbf{P} \mathbf{B}_{J}^{\theta} \, \mathrm{d}\Gamma - c \int_{\Gamma} \left[\mathbf{N}_{I}^{\theta^T} \mathbf{n}^T \mathbf{C} \mathbf{B}_{J}^{\theta} + \mathbf{B}_{I}^{\theta^T} \mathbf{C}^T \mathbf{n} \mathbf{N}_{J}^{\theta} \right] \mathrm{d}\Gamma \\ & + c \int_{\Gamma} \mathbf{B}_{I}^{\theta^T} \mathbf{C}^T \mathbf{n} \frac{1}{4} \boldsymbol{\epsilon}^T \mathbf{G} \boldsymbol{\epsilon} \mathbf{W}_{J}^{\theta} \, \mathrm{d}\Gamma \end{aligned} \tag{5.44}$$

$$\bar{\mathbf{K}}_{IJ}^{\theta\theta} = \mathbf{B}_{I}^{\theta^T} \mathbf{S} \mathbf{B}_{J}^{\theta} + \mathbf{B}_{I}^{\theta^T} \mathbf{T} \mathbf{Q}_{J}^{\theta} + \mathbf{Q}_{I}^{\theta^T} \mathbf{T}^T \mathbf{B}_{J}^{\theta} \tag{5.45}$$

$$\widehat{\mathbf{G}} = \mathbf{I} - \widehat{\mathbf{D}} \mathbf{G} \tag{5.46}$$

$$\bar{\mathbf{G}} = \mathbf{I} - \mathbf{G} \widehat{\mathbf{D}} \tag{5.47}$$

with the surface normal vector **n** and the constitutive model-specific modulus **G**.

If the Nitsche's method is considered for imposing the Dirichlet boundary condition on the displacement, the following terms are additionally introduced, with the stability parameter ζ.

$$\mathbf{K}_{IJ}^{EBC,uu} = -\int_{\partial\Omega g} \mathbf{B}_I^{u^T} \widehat{\mathbf{D}} \mathbf{v} \mathbf{N}_J^u \, d\Gamma + \int_{\partial\Omega g} \mathbf{N}_I^{u^T} \left[\zeta \mathbf{N}_J^u - \mathbf{v}^T \widehat{\mathbf{G}} \widehat{\mathbf{D}} \mathbf{B}_J^u \right] d\Gamma \tag{5.48}$$

$$\mathbf{K}_{IJ}^{EBC,u\theta} = -\int_{\Gamma g} \mathbf{N}_I^{u^T} \mathbf{v}^T \frac{1}{2} \widehat{\mathbf{G}} \boldsymbol{\epsilon} \mathbf{W}_J^{\theta} \, d\Gamma \tag{5.49}$$

$$\mathbf{K}_{IJ}^{EBC,\theta u} = -\int_{\Gamma g} \mathbf{W}_I^{\theta^T} \frac{1}{2} \boldsymbol{\epsilon}^T \mathbf{v} \mathbf{N}_J^u \, d\Gamma \tag{5.50}$$

$$\mathbf{K}_{IJ}^{EBC,\theta\theta} = -\int_{\Gamma g} \bar{\mathbf{K}}_{IJ}^{\theta\theta} \frac{1}{2} \boldsymbol{\epsilon}^T \mathbf{v} (\mathbf{u} - \mathbf{g}^u) \, d\Gamma. \tag{5.51}$$

5.4. Strong Imposition of Rotational Kinematic Constraint on Boundary

Another approach to remove the spurious rigid lattice rotation modes is the imposition of the rotational kinematic constraints on boundaries in (4.17). Consider the following matrix equation of the incremental formulation (5.40) with kinematically admissible function spaces:

$$\mathbf{K}\Delta\mathbf{d} = \begin{bmatrix} \mathbf{K}^{uu} & \mathbf{K}^{u\theta^d} & \mathbf{K}^{u\theta_b} \\ \mathbf{K}^{\theta^d u} & \mathbf{K}^{\theta^d\theta^d} & \mathbf{K}^{\theta^d\theta^b} \\ \mathbf{K}^{\theta^b u} & \mathbf{K}^{\theta^b\theta^d} & \mathbf{K}^{\theta^b\theta^b} \end{bmatrix} \begin{bmatrix} \Delta\mathbf{u} \\ \Delta\boldsymbol{\theta}^d \\ \Delta\boldsymbol{\theta}^b \end{bmatrix} = \begin{bmatrix} \Delta\mathbf{f}^u \\ \Delta\mathbf{f}^{\theta^d} \\ \Delta\mathbf{f}^{\theta^b} \end{bmatrix} = \mathbf{f}, \tag{5.52}$$

where the superscripts d and b denote quantities associated with domain and boundary, respectively. Let N^u, N^{θ^d}, and N^{θ^b} be the length of the vectors $\Delta\mathbf{u}$, $\Delta\boldsymbol{\theta}^d$, and $\Delta\boldsymbol{\theta}^b$, respectively. On a boundary node $\mathbf{x}_I$, the following relation holds.

$$\Delta\theta_{Ii}^b = \Delta\varphi_i^e(\mathbf{x}_I) = -\frac{1}{2}\epsilon_{ijk}\left(\Delta e_{jk}(\mathbf{x}_I) - \Delta e_{jk}^p(\mathbf{x}_I)\right), \tag{5.53}$$

where

$$\Delta\mathbf{e} = \mathbf{B}\Delta\mathbf{u} \tag{5.54}$$

and

$$\Delta\mathbf{e}^p = \mathbf{C}^u\Delta\mathbf{u} + \mathbf{C}^\theta\Delta\boldsymbol{\theta} \tag{5.55}$$

Then,

$$\Delta\boldsymbol{\theta}^b = \begin{bmatrix}\mathbf{A}^u & \mathbf{A}^{\theta^d} & \mathbf{A}^{\theta^b}\end{bmatrix}\begin{bmatrix}\Delta\mathbf{u}\\ \Delta\boldsymbol{\theta}^d\\ \Delta\boldsymbol{\theta}^b\end{bmatrix}, \tag{5.56}$$

where

$$\mathbf{A}^u = -\frac{1}{2}\boldsymbol{\epsilon}^T(\mathbf{B} - \mathbf{C}^u)\Delta\mathbf{u} \tag{5.57}$$

$$\mathbf{A}^{\theta^d} = \frac{1}{2}\boldsymbol{\epsilon}^T\mathbf{C}^{\theta^d}\Delta\boldsymbol{\theta}^d \tag{5.58}$$

$$\mathbf{A}^{\theta^b} = \frac{1}{2}\boldsymbol{\epsilon}^T \mathbf{C}^{\theta^b} \Delta\boldsymbol{\theta}^b, \tag{5.59}$$

which leads to

$$\Delta\boldsymbol{\theta}^b = \boldsymbol{\Lambda}\begin{bmatrix}\Delta\mathbf{u} \\ \Delta\boldsymbol{\theta}^d\end{bmatrix}, \tag{5.60}$$

where

$$\boldsymbol{\Lambda} = \left(\mathbf{I}^b - \mathbf{A}^{\theta^b}\right)^{-1}\begin{bmatrix}\mathbf{A}^u & \mathbf{A}^{\theta^d}\end{bmatrix}, \tag{5.61}$$

with the identity matrix $\mathbf{I}^b$ with the size of $N^{\theta^b} \times N^{\theta^b}$. Now, we have

$$\begin{bmatrix}\Delta\mathbf{u} \\ \Delta\boldsymbol{\theta}^d \\ \Delta\boldsymbol{\theta}^b\end{bmatrix} = \widehat{\boldsymbol{\Lambda}}\begin{bmatrix}\Delta\mathbf{u} \\ \Delta\boldsymbol{\theta}^d\end{bmatrix}, \tag{5.62}$$

with

$$\widehat{\boldsymbol{\Lambda}} = \begin{bmatrix}\mathbf{I}^d \\ \boldsymbol{\Lambda}\end{bmatrix}, \tag{5.63}$$

where $\mathbf{I}^d$ is the identity matrix with the size of $\left(N^u + N^{\theta^d}\right) \times \left(N^u + N^{\theta^d}\right)$.

By pre-multiplying $\mathbf{K}$ and $\Delta\mathbf{f}$, and post-multiplying $\mathbf{K}$ by $\widehat{\boldsymbol{\Lambda}}$, we have the following modified system matrix equation.

$$\widehat{\mathbf{K}}\Delta\widehat{\mathbf{u}} = \Delta\hat{\mathbf{f}} \tag{5.64}$$

with

$$\widehat{\mathbf{K}} = \widehat{\mathbf{\Lambda}}^T \mathbf{K} \widehat{\mathbf{\Lambda}} \tag{5.65}$$

$$\Delta\hat{\mathbf{f}} = \widehat{\mathbf{\Lambda}}^T \Delta\mathbf{f} \tag{5.66}$$

$$\Delta\hat{\mathbf{u}} = \begin{bmatrix} \Delta\mathbf{u} \\ \Delta\boldsymbol{\theta}^d \end{bmatrix}. \tag{5.67}$$

Acknowledgments

A portion of this chapter has been accepted for publication in Baek, J., Chen, J. S., Tupek, M., Beckwith, F., & Fang, H. E. "A Duality-based Coupling of Cosserat Crystal Plasticity and Phase Field Theories for Modeling Grain Refinement", International Journal for Numerical Methods in Engineering. The dissertation author was the primary investigator of this material.

Chapter 6

Stability Analysis of Duality-based Coupled Cosserat Crystal Plasticity – Phase Field Formulation

In this chapter, the stability properties of the proposed method are investigated and an additional stabilization is suggested. The phase field is not included here to focus on the instability that arises from the duality-based imposition of the rotational kinematic constraint.

6.1. Weak inf-sup condition

Consider the following variational formulation associated with the unstabilized dual problem: find $\mathbf{u}^h \in \mathcal{U}^h \in H_0^1$ and $\boldsymbol{\theta}^h \in \mathcal{T}^h \subset H_0^2$, such that

$$a(\mathbf{u}^h, \delta\mathbf{u}^h) + d(\delta\mathbf{u}^h, \boldsymbol{\theta}^h) = F(\delta\mathbf{u}^h), \ \ \forall\, \delta\mathbf{u}^h \in \mathcal{U}^h \subset H_0^1, \tag{6.1}$$

$$d(\mathbf{u}^h, \delta\boldsymbol{\theta}^h) - b(\boldsymbol{\theta}^h, \delta\boldsymbol{\theta}^h) = 0, \ \ \forall\, \delta\boldsymbol{\theta}^h \in \mathcal{T}^h \subset H_0^2, \tag{6.2}$$

where bilinear forms $a(\cdot,\cdot)$, $b(\cdot,\cdot)$, and $d(\cdot,\cdot)$ are defined as

$$a(\mathbf{u}^h, \delta\mathbf{u}^h) = \int_\Omega \varepsilon_{ij}(\delta\mathbf{u}^h) C_{ijkl} \varepsilon_{kl}(\mathbf{u}^h)\, \mathrm{d}\Omega, \tag{6.3}$$

$$b(\boldsymbol{\theta}^h, \delta\boldsymbol{\theta}^h) = -\int_\Omega \delta\theta^h_{i,j} m_{ij}\, \mathrm{d}\Omega - \int_\Omega \delta\theta^h_i m_{ij,j}\, \mathrm{d}\Omega - \int_\Omega \delta m_{ij,j} \theta^h_i \mathrm{d}\Omega, \tag{6.4}$$

$$d(\delta\mathbf{u}^h, \boldsymbol{\theta}^h) = -\int_\Omega \varphi_i(\delta\mathbf{u}^h) m_{ij,j}\, \mathrm{d}\Omega. \tag{6.5}$$

The bilinear form $a(\cdot,\cdot)$ is assumed to possess the following property:

$$a(\mathbf{u}^h, \mathbf{u}^h) \geq C^a \|\mathbf{u}^h\|_1^2. \tag{6.6}$$

The constant C^a is independent of nodal spacing h. By applying integration by parts to the second and third terms on the right-hand side of Eq. (6.4) with $\boldsymbol{\theta}^h \in H_0^2$, $b(\boldsymbol{\theta}^h, \delta\boldsymbol{\theta}^h) = \int_\Omega \delta m_{ij} \theta_{i,j}^h \, \mathrm{d}\Omega$ is obtained, and $b(\cdot,\cdot)$ is assumed to be positive semi-definite:

$$b(\boldsymbol{\theta}^h, \boldsymbol{\theta}^h) \geq C^b |\boldsymbol{\theta}^h|_1^2 \geq 0. \tag{6.7}$$

The bilinear form $d(\cdot,\cdot)$ is required to satisfy the inf-sup condition for positive constant γ independent of h:

$$\sup_{\mathbf{u}^h \in \mathcal{U}^h} \frac{d(\mathbf{u}^h, \boldsymbol{\theta}^h)}{\|\mathbf{u}^h\|_1} \geq \gamma \|\mathbf{m} \cdot \nabla\|_0, \qquad \forall\, \boldsymbol{\theta}^h \in \mathcal{T}^h \tag{6.8}$$

To find the missing term in satisfying Eq. (6.8), a weak inf-sup condition is derived, inspired by Bochev et al.[100].

$$\sup_{\mathbf{u}^h \in \mathcal{U}^h} \frac{\int_\Omega \varphi_i(\mathbf{u}^h)\left(-m_{ij,j}\right) \mathrm{d}\Omega}{\|\mathbf{u}^h\|_1} \geq \frac{\left|\int_\Omega \varphi_i(\delta\mathbf{u}^h)(-m_{ij,j})\, \mathrm{d}\Omega\right|}{\|\delta\mathbf{u}^h\|_1}$$
$$\geq \frac{\left|\int_\Omega \varphi_i(\delta\mathbf{u}^h)(-m_{ij,j})\, \mathrm{d}\Omega\right|}{C\|\delta\mathbf{u}\|_1}$$
$$= \frac{\left|\int_\Omega \Big(\varphi_i(\delta\mathbf{u}^h) - \varphi_i(\delta\mathbf{u})\Big)(-m_{ij,j})\, \mathrm{d}\Omega + \int_\Omega \varphi_i(\delta\mathbf{u})(-m_{ij,j})\, \mathrm{d}\Omega\right|}{C\|\delta\mathbf{u}\|_1} \tag{6.9}$$
$$\geq \frac{\int_\Omega \varphi_i(\delta\mathbf{u})(-m_{ij,j})\, \mathrm{d}\Omega - \left|\int_\Omega \Big(\varphi_i(\delta\mathbf{u}^h) - \varphi_i(\delta\mathbf{u})\Big)(-m_{ij,j})\, \mathrm{d}\Omega\right|}{C\|\delta\mathbf{u}\|_1}$$

With Eq. (3.5), the terms in the numerator of the right-hand side of Eq, (6.9) can be expressed as follows:

$$\int_\Omega \varphi_i(\delta\mathbf{u})(-m_{ij,j})\, \mathrm{d}\Omega = \int_\Omega \delta u_{j,k}(\frac{1}{2}\epsilon_{ijk} m_{il,l})\, \mathrm{d}\Omega \tag{6.10}$$

$$\left|\int_\Omega \Big(\varphi_i(\delta\mathbf{u}^h) - \varphi_i(\delta\mathbf{u})\Big)(-m_{ij,j})\, \mathrm{d}\Omega\right| = \left|\int_\Omega \big(\delta u^h_{j,k} - \delta u_{j,k}\big)(\frac{1}{2}\epsilon_{ijk} m_{il,l})\, \mathrm{d}\Omega\right| \tag{6.11}$$

Let us define $\boldsymbol{\sigma}^\times = \frac{1}{2}\boldsymbol{\epsilon} \cdot (\mathbf{m} \cdot \nabla)$ and assume $\boldsymbol{\sigma}^\times \in L_2$, then, there exists $\delta\mathbf{u} \in H_0^1$ that satisfies the following inequality:

$$\int_\Omega \delta u_{j,k}(\frac{1}{2}\epsilon_{ijk} m_{il,l})\, \mathrm{d}\Omega = \int_\Omega \delta u_{j,k}\sigma^\times_{jk}\, \mathrm{d}\Omega \geq C_1\|\delta\mathbf{u}\|_1\|\boldsymbol{\sigma}^\times\|_0. \tag{6.12}$$

Also, by performing integration by parts on Eq. (6.11),

$$\left|\int_\Omega \big(\delta u^h_{j,k} - \delta u_{j,k}\big)(\frac{1}{2}\epsilon_{ijk} m_{il,l})\, \mathrm{d}\Omega\right| = \left|\int_\Omega \big(\delta u^h_j - \delta u_j\big)\frac{1}{2}\epsilon_{ijk} m_{il,lj}\, \mathrm{d}\Omega\right| \tag{6.13}$$
$$\leq \|\nabla\boldsymbol{\sigma}^\times\|_0\|\delta\mathbf{u} - \delta\mathbf{u}^h\|_0 \leq C_2 h\|\nabla\boldsymbol{\sigma}^\times\|_0\|\delta\mathbf{u}\|_1,$$

where the last inequality holds due to the inverse inequality. Together with Eqs. (6.12) and (6.13), Eq. (6.9) becomes

$$\sup_{\mathbf{u}^h \in \mathcal{U}^h} \frac{\int_\Omega \varphi_i(\mathbf{u}^h)\left(-m_{ij,j}\right) \mathrm{d}\Omega}{\|\mathbf{u}^h\|_1} \geq \frac{C_1}{C}\|\boldsymbol{\sigma}^\times\|_0 - \frac{C_2}{C} h \|\nabla \boldsymbol{\sigma}^\times\|_0. \tag{6.14}$$

Let us consider the case that $\boldsymbol{\sigma}^\times \in H^1$ and introduce a projection operator $\pi^L(\cdot) = \frac{1}{V_L}\int_{\Omega_L}(\cdot)\,\mathrm{d}\Omega$ with the volume V_L of the integration domain Ω_L. Then, with $\nabla \pi^L \boldsymbol{\sigma}^\times = \mathbf{0}$ in Ω_L,

$$\|\nabla(\boldsymbol{\sigma}^\times)\|_0 = \sum_L \|\nabla(\boldsymbol{\sigma}^\times - \pi^L \boldsymbol{\sigma}^\times)\|_{0,\Omega_L} \leq \frac{\bar{C}}{h}\sum_L \|\boldsymbol{\sigma}^\times - \pi^L \boldsymbol{\sigma}^\times\|_{0,\Omega_L}, \tag{6.15}$$

which leads to

$$\sup_{\boldsymbol{u}^h \in \mathcal{U}^h} \frac{\int_\Omega \varphi_i(\mathbf{u}^h)\left(-m_{ij,j}\right) \mathrm{d}\Omega}{\|\mathbf{u}^h\|_1} + \frac{C_2 \bar{C}}{C}\sum_L \|\boldsymbol{\sigma}^\times - \pi^L \boldsymbol{\sigma}^\times\|_{0,\Omega_L} \geq \frac{C_1}{C}\|\boldsymbol{\sigma}^\times\|_0. \tag{6.16}$$

Based on this stability analysis, the introduction of $\frac{\kappa^{proj}}{2}\|\boldsymbol{\sigma}^\times - \pi^L \boldsymbol{\sigma}^\times\|_0^2$ into Eq. (4.12) can be considered for the formulation to be stable as follows.

$$\begin{aligned}\Pi = \frac{1}{2}\int_\Omega \varepsilon_{ij}\sigma_{ij}^c \,\mathrm{d}\Omega + \int_\Omega f_\alpha(\eta)\alpha\|\nabla\boldsymbol{\theta}\| + f_\beta(\eta)\frac{\beta}{2}\|\nabla\boldsymbol{\theta}\|^2 \,\mathrm{d}\Omega + \int_\Omega m_{ij,j}(\theta_i - \varphi_i^e)\,\mathrm{d}\Omega \\ - \int_{\partial\Omega} m_{ij}n_j(\theta_i - \varphi_i^e)\,\mathrm{d}\Gamma - \frac{\kappa^{proj}}{2}\|\boldsymbol{\sigma}^\times - \pi^L\boldsymbol{\sigma}^\times\|_0^2 \\ + 2\mu_c\int_\Omega (\theta_i - \varphi_i^e)(\theta_i - \varphi_i^e)\,\mathrm{d}\Omega + \int_\Omega pr(\eta) + \frac{q}{2}(\nabla\eta)^2\,\mathrm{d}\Omega \\ - \Pi^{ext}(\mathbf{u},\eta)\end{aligned} \tag{6.17}$$

Bochev et al.[100] state that the parameter k^{proj} is introduced for the dimensional correction, not a tunable stabilization parameter. Along this line, we introduce $k^{proj} = a^2/C^p$ with the kernel support size a (see Section 5.1) and $C^p = \pi^L(\|\mathbf{P}\|)$ where $\mathbf{P}$ is the tensor defining the relation between the couple stress divergence and second gradient of θ as given below by taking the divergence of the couple stress in (4.7) with $\eta = 1$.

$$m_{in,n} = P_{ijkl}\theta_{k,lj}, \tag{6.18}$$

where

$$P_{ijkl} = \left(\frac{\alpha}{\|\nabla\boldsymbol{\theta}\|} + \beta\right)\delta_{ik}\delta_{jl} - \frac{\alpha}{\|\nabla\boldsymbol{\theta}\|^3}\theta_{i,j}\theta_{k,l}. \tag{6.19}$$

6.2. Parameter range for least squares stabilization

Now, consider the following modified dual problem with the least squares stabilization adopted to avoid the spurious rigid lattice rotation (see Remark 1).

$$\bar{a}(\mathbf{u}^h, \delta\mathbf{u}^h) = a(\mathbf{u}^h, \delta\mathbf{u}^h) + 4\mu_c \int_\Omega \delta\varphi_i^h \varphi_i^h \, \mathrm{d}\Omega, \tag{6.20}$$

$$\bar{b}(\boldsymbol{\theta}^h, \delta\boldsymbol{\theta}^h) = b(\boldsymbol{\theta}^h, \delta\boldsymbol{\theta}^h) - 4\mu_c \int_\Omega \delta\theta_i^h \theta_i^h \, \mathrm{d}\Omega, \tag{6.21}$$

$$\bar{d}(\delta\mathbf{u}^h, \boldsymbol{\theta}^h) = d(\delta\mathbf{u}^h, \boldsymbol{\theta}^h) - 4\mu_c \int_\Omega \delta\varphi_i^h \theta_i^h \, \mathrm{d}\Omega, \tag{6.22}$$

where $a(\cdot,\cdot)$, $b(\cdot,\cdot)$, and $c(\cdot,\cdot)$ are defined in Eqs. (6.3) – (6.5). Let the stability parameter be a scaled shear modulus, $\mu_c = \bar{c}\mu$, with scaling parameter $\bar{c}$. To determine the suitable range of $\bar{c}$, the following system bilinear operator $\mathcal{A}$ is considered by subtracting Eq. (6.2) from Eq. (6.1) and substituting $\mathbf{u}^h$ and $\boldsymbol{\theta}^h$ into $\delta\mathbf{u}^h$ and $\delta\boldsymbol{\theta}^h$, respectively:

$$\begin{aligned}\mathcal{A}\Big((\mathbf{u}^h,\boldsymbol{\theta}^h),(\mathbf{u}^h,\boldsymbol{\theta}^h)\Big) &= \bar{a}(\mathbf{u}^h,\mathbf{u}^h)+\bar{b}(\boldsymbol{\theta}^h,\boldsymbol{\theta}^h)\\ &\geq C^a\|\mathbf{u}^h\|_1^2 + C^b|\boldsymbol{\theta}^h|_1^2 + \bar{c}\mu\int_\Omega \varphi_i^h\varphi_i^h\,\mathrm{d}\Omega - \bar{c}\mu\int_\Omega \theta_i^h\theta_i^h\,\mathrm{d}\Omega,\end{aligned} \tag{6.23}$$

With Eq. (6.7) in hand, a positive stability parameter $\bar{c}$ could make the bilinear operator $\bar{b}(\cdot,\cdot)$ lose its positive semi-definiteness. On the other hand, a negative $\bar{c}$ leads to

$$\bar{b}(\boldsymbol{\theta}^h,\boldsymbol{\theta}^h) \geq -\bar{c}\mu\|\boldsymbol{\theta}^h\|_0^2 + C^b|\boldsymbol{\theta}^h|_1^2 \geq \min(C^b,-\bar{c}\mu)\,\|\boldsymbol{\theta}^h\|_1^2, \tag{6.24}$$

However, $\bar{c}$ should not be too low to avoid losing the coercivity on $\bar{a}(\mathbf{u}^h,\mathbf{u}^h)$. To determine a proper lower limit, consider a two-dimensional case with homogeneous Dirichlet boundaries on $\mathbf{u}^h$:

$$\bar{a}(\mathbf{u}^h,\mathbf{u}^h) = \int_\Omega \frac{\mu}{2}\big(u_{i,j}^h + u_{j,i}^h\big)\big(u_{i,j}^h + u_{j,i}^h\big) + \lambda u_{i,i}^h u_{j,j}^h\,\mathrm{d}\Omega + \bar{c}\mu\int_\Omega {\varphi_3^h}^2\,\mathrm{d}\Omega, \tag{6.25}$$

where $i,j = 1,2$. In the last term of (6.25), φ_3^h is equivalent to $\varphi_3^h = -0.5\epsilon_{3ij}u_{i,j} = 0.5\big(u_{2,1}^h - u_{1,2}^h\big)$. Also, performing the integration by parts twice, we have $\int_\Omega \mu u_{i,j}^h u_{j,i}^h\,\mathrm{d}\Omega = \int_\Omega \mu u_{i,i}^h u_{j,j}^h\,\mathrm{d}\Omega$. Thus, the following inequality is obtained.

$$\bar{a}(\mathbf{u}^h, \mathbf{u}^h) \geq \mu \int_\Omega u^h_{i,j} u^h_{i,j} \, \mathrm{d}\Omega + \bar{c}\mu \int_\Omega \left(u^h_{1,2} u^h_{1,2} + u^h_{2,1} u^h_{2,1} \right) \mathrm{d}\Omega. \tag{6.26}$$

With $c \equiv -\bar{c} < 1$, $a(\cdot,\cdot)$ maintains $\bar{a}(\mathbf{u}^h, \mathbf{u}^h) \geq \bar{C}^a \|\mathbf{u}^h\|_1^2$ with a positive constant $\bar{C}^a$, so $\mathcal{A}\Big((\mathbf{u}^h, \boldsymbol{\theta}^h), (\mathbf{u}^h, \boldsymbol{\theta}^h)\Big) \geq C^a \|\mathbf{u}^h\|_1^2 + C^b \|\boldsymbol{\theta}^h\|_1^2$. Note that the derivation is based on the Dirichlet boundary assumption. The upper limit can be slightly lower when a Neumann boundary is present. For these reasons, $\log_{10} c \leq -2$ is suggested. The lower limit must be sufficiently large and $\log_{10} c \geq -5$ is suggested although this is not a decisive value. Numerical studies on the upper limit and the c-sensitivity of solution are shown in Sections 6.3.1 and 0.

6.3. Numerical Verification

A series of numerical examples are presented in this section to demonstrate that the proposed method is stable, convergent, and insensitive to the stability parameter. The plane strain is assumed and a quadratic RK basis is used for the displacement, the lattice rotation, and the phase field with a normalized support size of 3.0 unless otherwise stated. For the domain integration, the 5×5 Gauss quadrature is employed.

6.3.1. Stabilization effects and convergence

To demonstrate the proposed stabilization techniques, we consider a two-dimensional Cosserat elasticity problem with the problem domain $\Omega = (-H/2, +H/2) \times (-H/2, +H/2)$ with $H = 10$ μm and all displacement boundaries are Dirichlet boundaries as shown in Figure 6.1 (a). The phase field is neglected. The Lamé constants $\lambda = 69.2$ GPa, $\mu = 46.1$ GPa and the Cosserat parameters $\alpha = 0$, $\beta = \mu \ell_\beta^2$ with $\ell_\beta = H/5$ are used. As shown in Figure 6.1 (b), the domain is

discretized by 441 uniformly distributed RK nodes and the linear RK basis is used for both **u** and θ with a cubic B-spline kernel function and the normalized support size of 2.0. For the domain integration, the 5×5-point Gauss integration is employed for 400 conforming integration domains which uniformly divide Ω. Nitsche's method is used to impose the Dirichlet boundary condition on **u**.

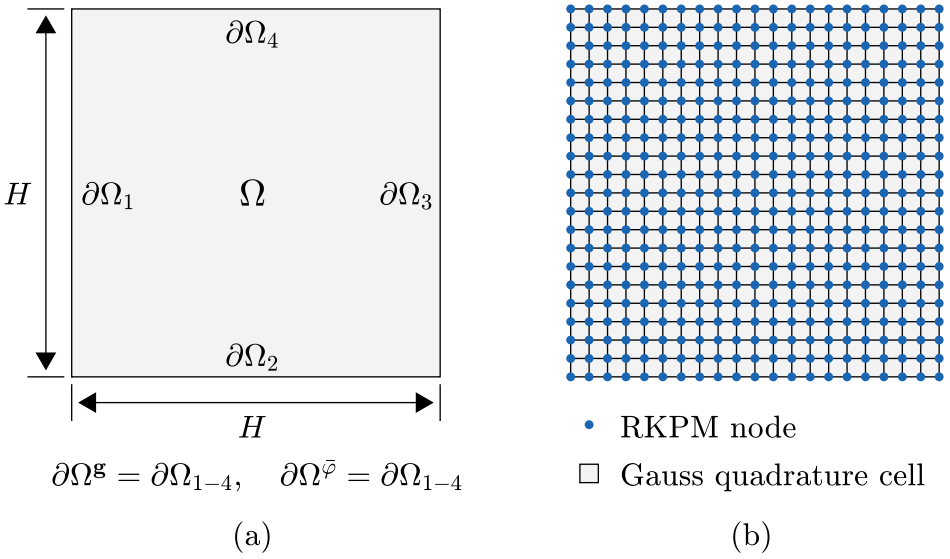

Figure 6.1. Problem setup: (a) domain and boundaries, (b) RKPM nodes and Gauss quadrature cells

Figure 6.2 shows the first five lowest energy modes of the condensed stiffness matrix $\bar{\mathbf{K}}$ defined as

$$\mathbf{K} = \begin{bmatrix} \mathbf{K}^{uu} & \mathbf{K}^{u\theta} \\ \mathbf{K}^{u\theta^T} & -\mathbf{K}^{\theta\theta} \end{bmatrix}, \qquad \bar{\mathbf{K}} = \mathbf{K}^{\theta\theta} + \mathbf{K}^{\theta u}\mathbf{K}^{uu^{-1}}\mathbf{K}^{\theta u^T}. \tag{6.27}$$

In this example, Dirichlet boundary conditions on the rotation are also applied to all four boundaries ($\partial\Omega_{1-4}$) using Eq. (4.19) and $c = 0$. Figure 6.2(a) shows that the formulation without

the weak inf-sup projection yields severe node-to-node oscillation modes. In contrast, such unstable modes are not observed in the formulation with the projection following (6.17).

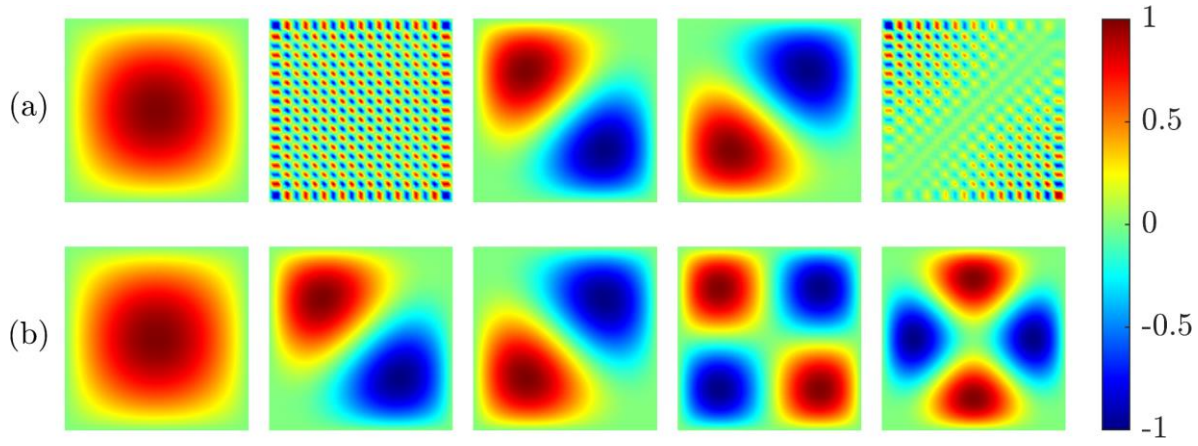

Figure 6.2. Five lowest energy modes: (a) without projection and (b) with projection

Let us consider the body force and boundary conditions corresponding to the following analytical solution:

$$
\begin{aligned}
u_1 &= \frac{2H}{\pi}\bar{\theta}\sin\left(\frac{\pi}{2H}(x_1+x_2)\right)\\
u_2 &= \frac{2H}{\pi}\bar{\theta}\sin\left(\frac{\pi}{2H}(x_1-x_2)\right)\\
\theta &= \frac{1}{2}\left(u_{2,1}-u_{1,2}\right) = \bar{\theta}\sin\left(\frac{\pi}{2H}x_1\right)\sin\left(\frac{\pi}{2H}x_2\right),
\end{aligned}
\tag{6.28}
$$

with $\bar{\theta} = 10°$.

The numerical solutions obtained with and without the projection are presented in Figure 6.3. The node-to-node oscillation modes shown in Figure 6.2 have strong effects on the solutions without implementing the projection, particularly on the curvature fields (right two subfigures on the top row of Figure 6.3). Such oscillations are effectively suppressed by the projection-based

stabilization. The projected formulation achieves the optimal convergence rates for linear bases and for quadratic bases as shown in Figure 6.4. For the convergence study, 121, 441, 1681, and 6561 RK nodes are used for each level of refinement. Throughout the remaining numerical examples, the projection-based stabilization is used for all simulations when solved by the proposed method, unless otherwise stated.

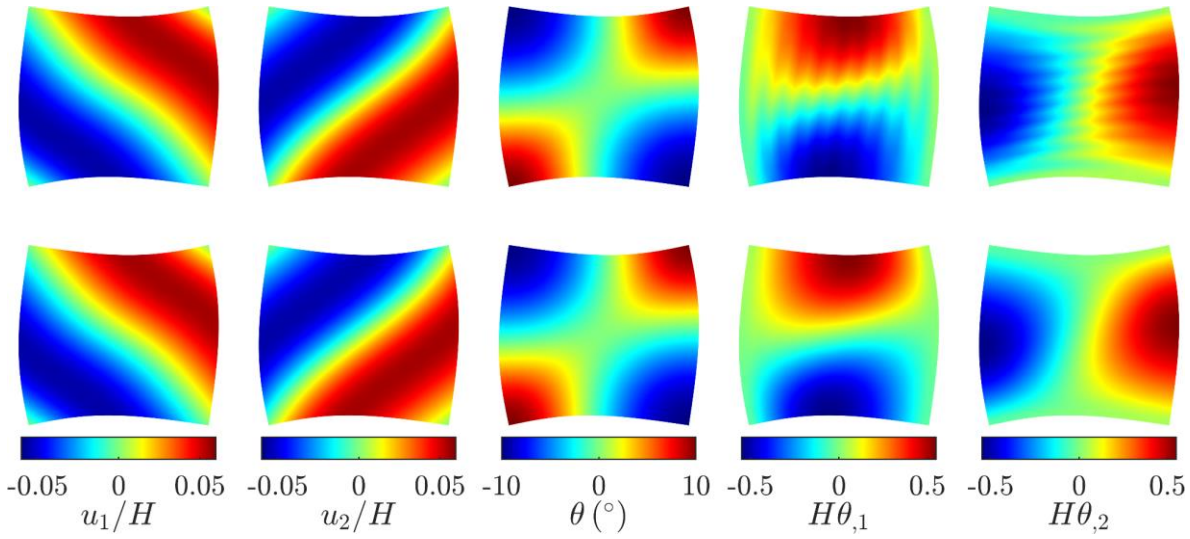

Figure 6.3. Solutions obtained by the proposed method without projection (top) and with projection (bottom)

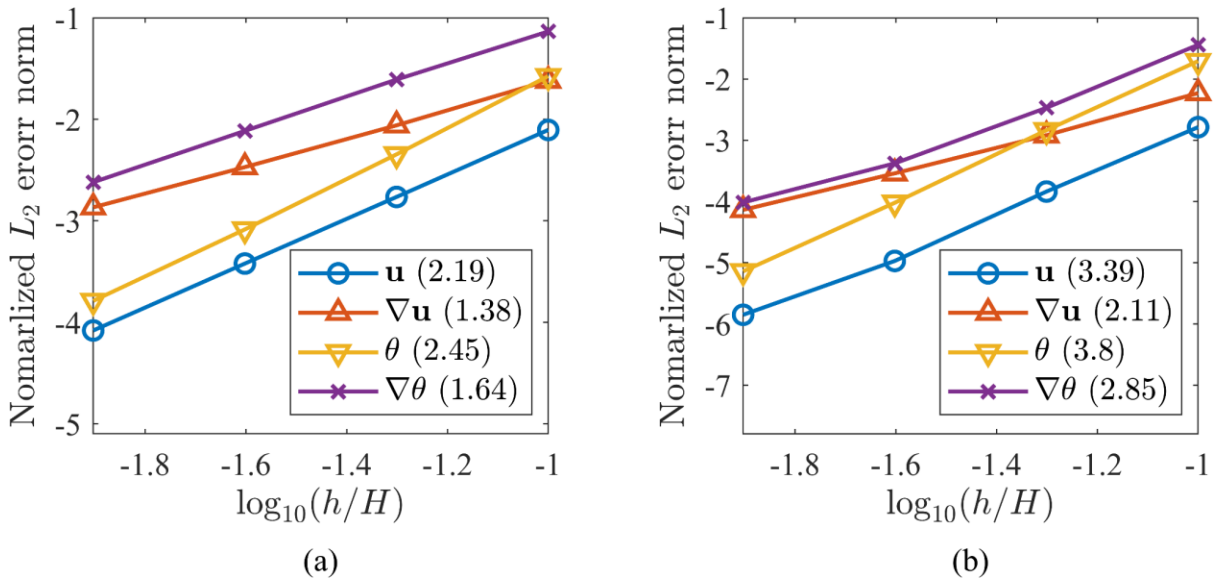

Figure 6.4. Convergence curves obtained by the proposed method with projection: (a) linear RK bases for $\mathbf{u}$ and θ and (b) quadratic RK bases for $\mathbf{u}$ and θ. The average convergence rates are enclosed by parentheses in the legends. The rotational Dirichlet boundary conditions are applied to both φ^e and θ. $c = 0$ is used.

6.3.2. Parameter sensitivity

Let us consider cases that there is no Dirichlet boundary conditions on rotation. To avoid spurious rigid lattice rotation, least squares stabilization can be utilized as discussed in Chapter 4. The stability analysis performed in Section 6.2 suggests that the upper limit of the normalized stabilization parameter c is one, i.e., at the upper limit, $\log_{10} c = 0$, for cases of Dirichlet displacement boundary. Table 6.1 lists the value of $\log_{10} c$ at which the sign of the minimum eigenvalue of $\bar{\mathbf{K}}$ in Eq. (6.27) changes from positive to negative for four cases with different boundary conditions. Case I agrees well with the result of the stability analysis and the upper limit of $\log_{10} c$ decreases as the fraction of Dirichlet boundary decreases. For this reason, $\log_{10} c \leq -2$ as estimated from stability analysis can be considered a conservative choice.

Table 6.1. List of cases with different displacement boundaries

Case	Displacement boundary	$\log_{10} c$ upper limit
Case I	Dirichlet: $\partial\Omega_{1-4}$ Neumann: $\emptyset$	0.2
Case II	Dirichlet: $\partial\Omega_{1-3}$ Neumann: $\partial\Omega_4$	-0.36
Case III	Dirichlet: $\partial\Omega_{1-2}$ Neumann: $\partial\Omega_{3-4}$	-0.85
Case IV	Dirichlet: $\partial\Omega_1$ Neumann: $\partial\Omega_{2-4}$	-0.94

Now, we investigate the solution accuracy and convergence behavior for a wide range of $\log_{10} c$ for Case III. As can be seen in Figure 6.5, for $-6 \leq \log_{10} c \leq -1$, nearly identical solution accuracy and convergence behaviors are obtained. However, for $\log_{10} c > 0$, poor performances are observed, which is consistent with the stability analysis in Section 6.2 and the numerically tested upper limit for a few cases of Dirichlet boundary conditions given in Table 6.1. Figure 6.7 shows the solution fields obtained by the proposed method with 441 RK nodes for each $\log_{10} c$. Clearly, the simulations with a positive $\log_{10} c$ lead to severe instability and such parameter range must be avoided. However, with negative $\log_{10} c$, the results are insensitive to $\log_{10} c$ in a wide range. Contrarily, the penalty-based approach is very sensitive to the penalty parameter as shown in Figure 6.6, and none of these cases achieves the optimal convergence rates for all four error measures. Also shown in Figure 6.8, small penalty parameters fail to capture θ and $\nabla\theta$ accurately.

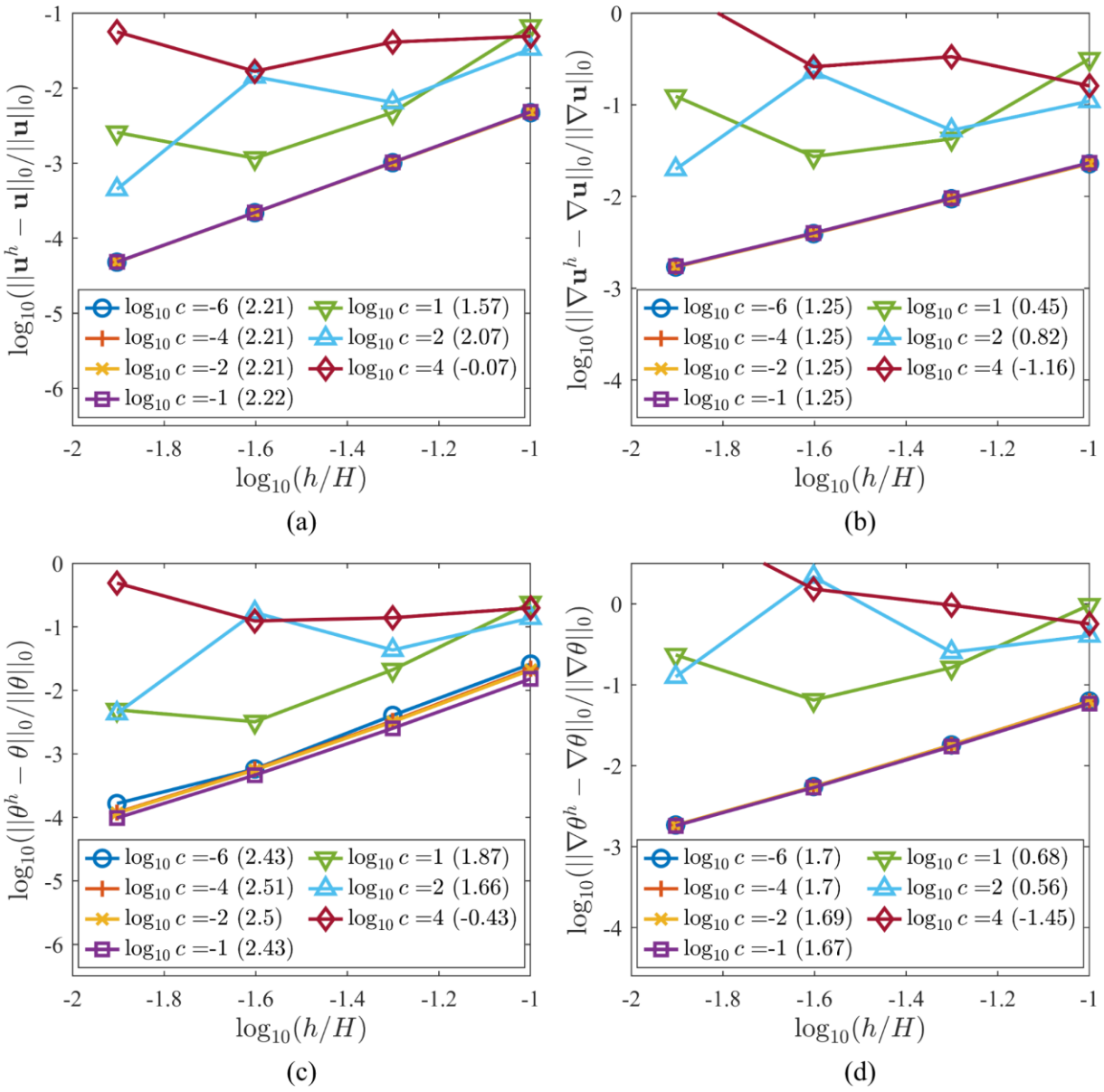

Figure 6.5. Convergence curves obtained by the proposed method with various c: (a) $\mathbf{u}^h$, (b) $\nabla\mathbf{u}^h$, (c) θ^h, and (d) $\nabla\theta^h$. The average convergence rates are enclosed by parentheses in the legends.

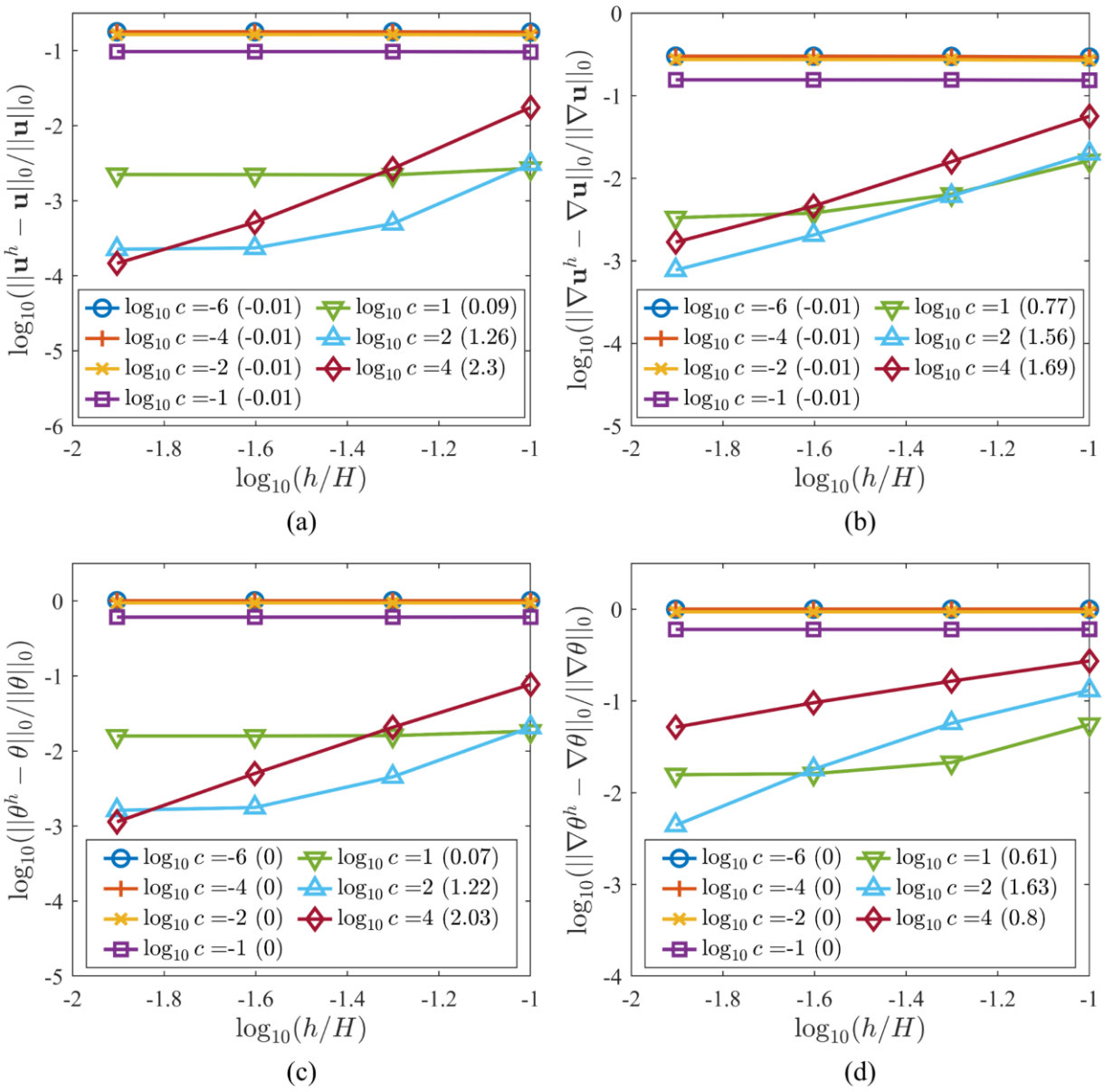

Figure 6.6. Convergence curves obtained by the penalty-based approach with various c: (a) $\mathbf{u}^h$, (b) $\nabla\mathbf{u}^h$, (c) θ^h, and (d) $\nabla\theta^h$. The average convergence rates are enclosed by parentheses in the legends.

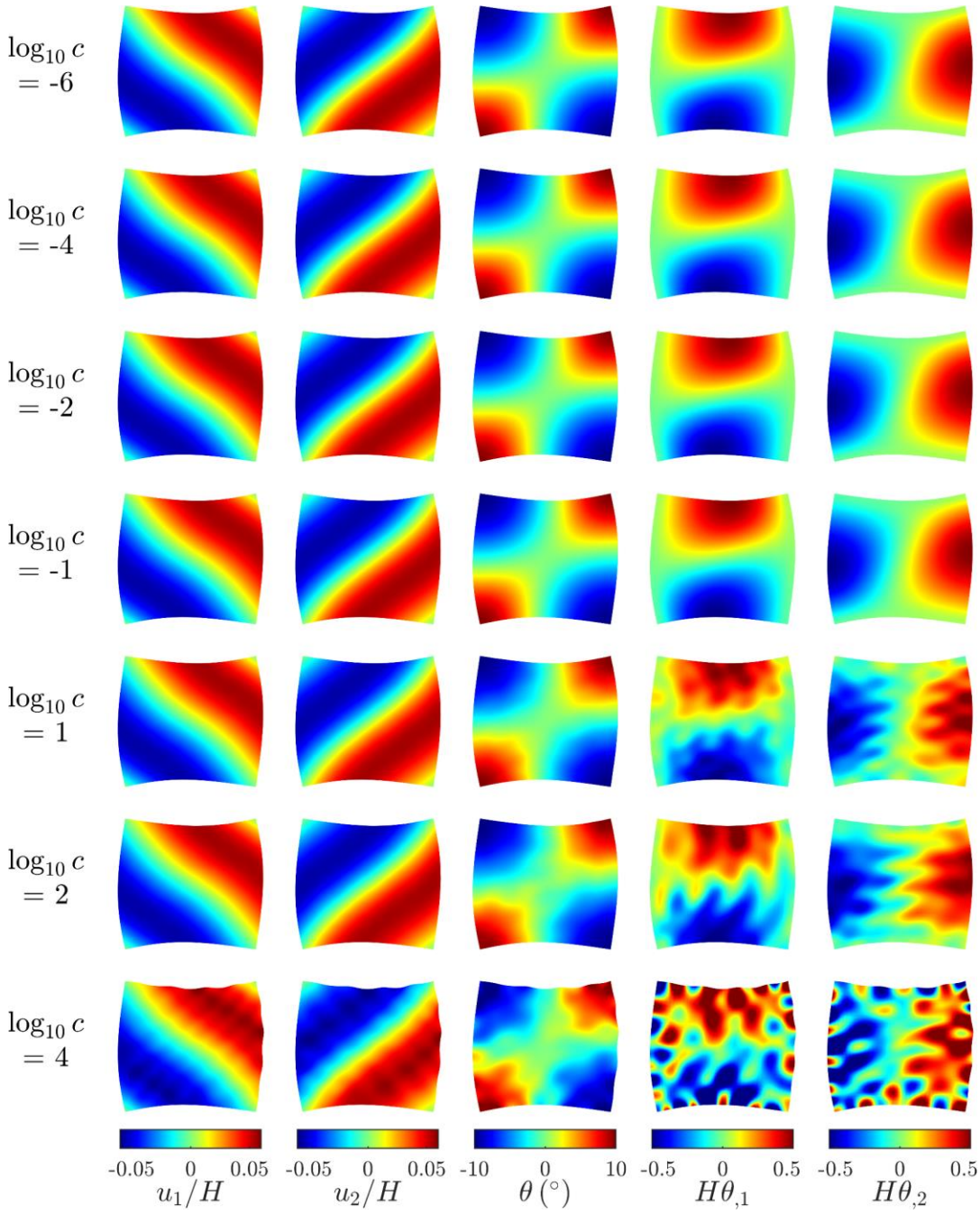

Figure 6.7. Solutions obtained by the proposed method for various *c*

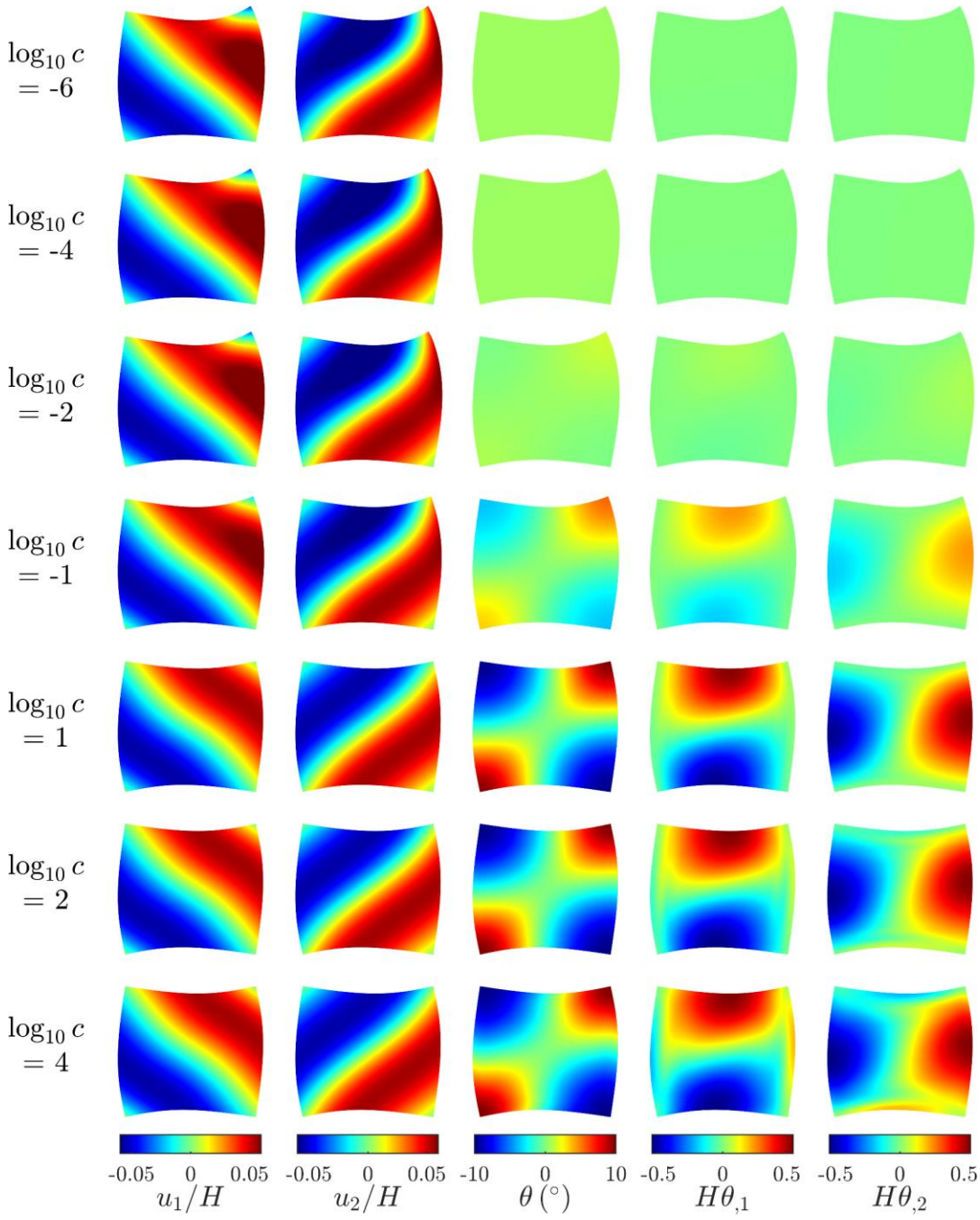

Figure 6.8. Solutions obtained by the penalty-based approach for various *c*

6.3.3. Computational costs

The CPU times taken for various methods to assemble the global matrices are plotted in Figure 6.9. The simulations were conducted by a parallel code written in MATLAB with four CPU cores (3.00 GHz per core) and a 32 GB RAM. Each CPU time is computed by averaging the CPU times of five simulations. On average, the proposed formulation costs approximately 22.0 % more than the penalty method due to the additional terms to assemble and the projection-based stabilization introduces 6.94 % of additional CPU time. Considering the convergence, accuracy, parameter insensitivity, and stability attained by the proposed method, the additional computational costs are justifiable. Note that a high-order Guass quadrature (5×5 points per cell) is used in this study to exclude errors introduced by the numerical integration since the RK shape functions and their derivatives are rational function: 2500, 10000, 40000, and 160000 total domain integration points are used for the cases of 121, 441, 1681, and 6561 RK nodes, respectively. Reduced order integration techniques such as stabilized conforming nodal integration[104, 105] and variationally consistent reduced order integration[106] can be considered as a future research of this work. Since the formulation is developed for general three-dimensional problems, the extension to 3D is straightforward, provided an efficient reduced order domain integration is employed.

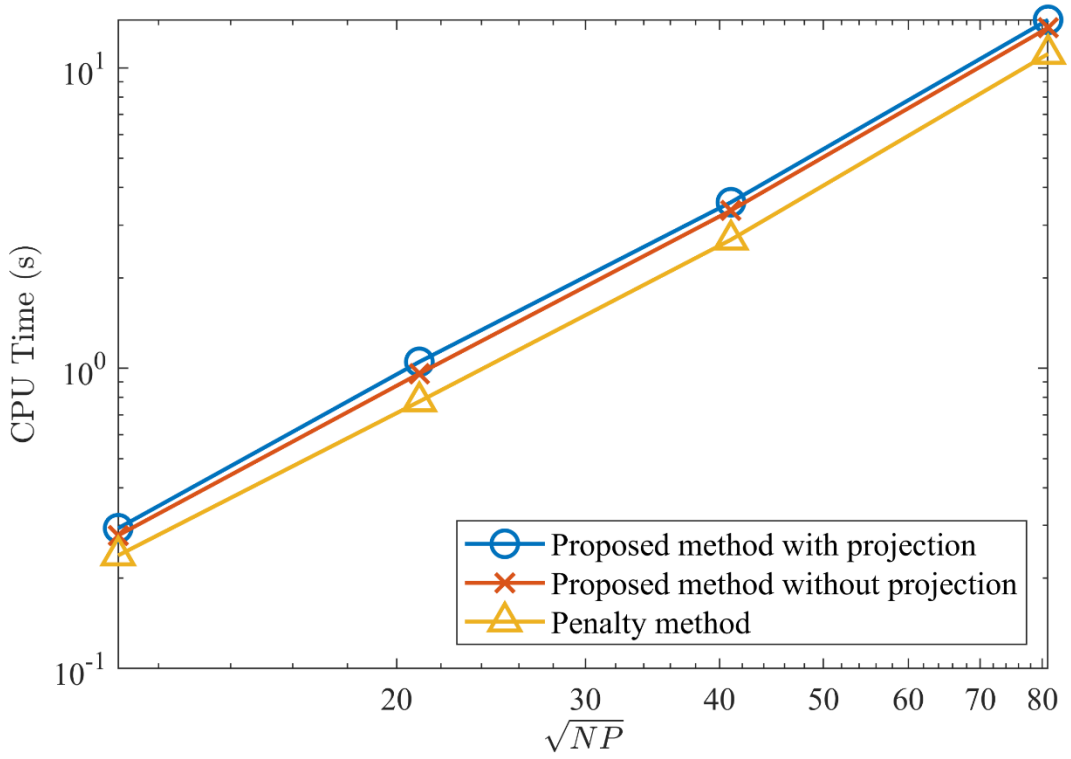

Figure 6.9. CPU times for the global matrix assembly taken by various methods: *NP* denotes the number of RK particles.

Acknowledgments

A portion of this chapter has been accepted for publication in Baek, J., Chen, J. S., Tupek, M., Beckwith, F., & Fang, H. E. "A Duality-based Coupling of Cosserat Crystal Plasticity and Phase Field Theories for Modeling Grain Refinement", International Journal for Numerical Methods in Engineering. The dissertation author was the primary investigator of this material.

Chapter 7

Neural Network-enhanced Reproducing Kernel Approximation

Modeling the sharp transition in the phase field near the grain boundaries associated with the lattice orientation often requires highly refined discretization for sufficient accuracy, which significantly increases the computational cost. While adaptive model refinement can be employed for enhanced effectiveness, it is cumbersome for the traditional mesh-based methods to perform adaptive model refinement.

In this chapter, a neural network enhanced RKPM is proposed. Neural network architectures are developed with interpretable weights and biases to automatically detect the locations and orientations of strain localization, and to construct functions with sharp transitions near the grain boundaries. Further, details of the network structure that incorporates the RK approximation will be presented.

7.1. Overview

Let $\mathbf{x} \in \mathbb{R}^D$ be the physical coordinate with space dimension D. The approximation $f^h(\mathbf{x}) \approx f(\mathbf{x}) \in \mathbb{R}$ is constructed by the addition of reproducing kernel (RK) and neural network (NN) approximations.

$$f^h(\mathbf{x}) = f^{h,RK}(\mathbf{x}) + f^{h,NN}(\mathbf{x}), \tag{7.1}$$

where $f^{h,RK}(\mathbf{x}) \in \mathcal{V}^{RK}$ and $f^{h,NN}(\mathbf{x}) \in \mathcal{V}^{NN}$ are RK approximation and NN approximation, respectively, with $\mathcal{V}^{RK}$ the RK approximation space and $\mathcal{V}^{NN}$ the NN approximation space. In the above approximation, the NN approximation is constructed to introduce a fine-scale feature to the solution at a region close to a localization and to capture sharp solution transitions, while the RK approximation is formulated to capture the overall smooth behavior of the solution. The RK approximation takes its traditional form discussed in Section 5.1:

$$f^{h,RK}(\mathbf{x}) = \sum_{I=1}^{NP} \Psi_I(\mathbf{x}) f_I^{RK}, \tag{7.2}$$

where $\Psi_I(\mathbf{x})$ and f_I^{RK} are RK shape function and RK generalized coefficient associated with RK node I, respectively.

7.1.1. Considerations on the construction of neural network approximation

In the construction of the NN approximation, we focus on the following considerations: 1) both *strong and weak discontinuities* should be approximated with a far higher resolution than the RK approximation, 2) the position and orientation of *complex localization paths* should be automatically captured, 3) the NN approximation influences only *local regions* close to localizations, and 4) the localization capturing procedure can be achieved by the *total potential minimization* without introducing additional criterion. As stated in Consideration 1, both strong and weak discontinuities are to be approximated by considering weak discontinuity in the displacement field and the corresponding strong discontinuity in the lattice orientation following $\varphi = u_{2,1} - u_{1,2}$ in 2D (Eq. (3.5)). To achieve Consideration 2, unknown parameters representing the localization position and orientation will be included in the NN approximation. Also, a block

level NN approximation will be constructed to capture complex localization topology by a superposition of multiple block-level NN approximations, each of which are designed to approximate relatively simple localization topology.

Consideration 3 is related to the computational efficiency. As the smooth solution far from the localization can be efficiently captured by the RK approximation, the domain of influence of the NN approximation should be small so that the NN approximation focuses on the regions around localizations that requires fine resolution of the solution. The neural network approximation will be designed such that the domain of influence is controlled by adjustable parameters that are automatically determined by the optimization. When multiple sparsely distributed localization clusters are populated in the domain as shown in Figure 7.1, the domain of influence in the NN approximation is sparsely distributed near the localization clusters. The aforementioned block-level NN approximation will also reflect this consideration.

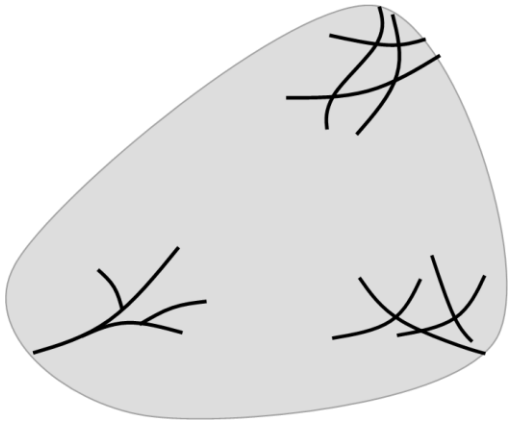

Figure 7.1. A domain with multiple localization regions

In the construction of NN approximation space that satisfies Considerations 1-3, parameters that control the location, orientation, and shape of a localization are included in the NN approximation space, and these parameters are determined by the potential energy minimization.

In the next subsection, a design of block-level NN approximation to satisfy Considerations 1-3 is proposed.

7.2. Block-level approximation

As discussed in Section 7.1.1, it is desirable to have the NN approximation only locally enrich the solution space in the presence of localizations for computational efficiency. In this regard, NN approximation is constructed by the block-level NN approximations as follows.

$$f^{h,NN}(\mathbf{x}) = \sum_{\mathrm{A}=1}^{NB} b_{\mathrm{A}}^{NN}\left(\mathbf{x}; \mathbf{W}_J\right), \tag{7.3}$$

where $b_{\mathrm{A}}^{NN}(\mathbf{x}; \mathbf{W}_{\mathrm{A}})$ is A-th block-level approximation with unknown weights and biases $\mathbf{W}_{\mathrm{A}}$ and NB is the number of blocks. Each NN block is constructed to capture a certain part of localizations distributed throughout the domain and to enrich the solution at a local region. Here the introduction of NN blocks helps reduce the number of unnecessary unknown weights and biases that exist when a dense network is employed. Also, the superposition of multiple block-level approximations is performed to capture complex localization topology.

In this work, the block-level approximation takes the following form:

$$b_{\mathrm{A}}^{NN}(\mathbf{x};\mathbf{W}) = \sum_{I=1}^{NK} \hat{\phi}_{I\mathrm{A}}(\mathbf{x};\mathbf{W}^{L},\mathbf{W}^{\mathrm{S}}) p(\mathbf{x};\mathbf{W}_{I\mathrm{A}}^{P}) \tag{7.4}$$

where p is a monomial function and $\hat{\phi}_{I\mathrm{A}}$ is a normalized kernel function. The role of the kernel function is to capture the location, orientation, and the transition shape of the localization. Thus $\hat{\phi}_{I\mathrm{A}}$ involves two sets of unknown parameters: the localization location and orientation capturing parameter set $\mathbf{W}^{L}$ and the kernel shape control parameter set $\mathbf{W}^{S}$ serving as the parameters in capturing the localization. Meanwhile, the monomial function adds the monomial completeness to the neural network function space with a set of unknown polynomial basis parameters $\mathbf{W}_{I\mathrm{A}}^{M}$ for further accuracy.

In the following sections, how these three sets of parameters contribute to the construction of the NN approximation suitable for capturing localizations will be introduced.

7.2.1. Construction of adjustable kernel functions

Let us consider the following one-dimensional kernel function:

$$\phi(y;\{\bar{y}_1,\bar{y}_2,c_1,c_2\}) = \bar{\phi}_1(y;\{\bar{y}_1,c_1\})\bar{\phi}_2(y;\{\bar{y}_2,c_2\}), \tag{7.5}$$

with

$$\bar{\phi}_i(y;\{\bar{y}_i,c_i\}) = \left(\frac{1}{2} - (-1)^i \frac{1}{2}\tanh\left(\frac{(y-\bar{y}_i)}{c_i}\right)\right) \tag{7.6}$$

where $\{\bar{y}_1,\bar{y}_2,c_1,c_2\}$ is a set of shape control parameters. Figure 7.2 illustrates the above-mentioned kernel function constructed with various sets of the shape control parameters. The

kernels presented in Figure 7.2(a) and (b) possess a sharp transition while the kernel shown in Figure 7.2(c) is a symmetric kernel. For simulation of grain boundary evolution, kernels in Figure 7.2(a) and (b) are suitable in capturing the sharp transition of the lattice orientation, i.e., strong localization of lattice curvature. The symmetric kernel in Figure 7.2(c) is suitable in approximating the localized phase field with a small support. In this work, this kernel is called *neural network (NN) kernel (Type I)*.

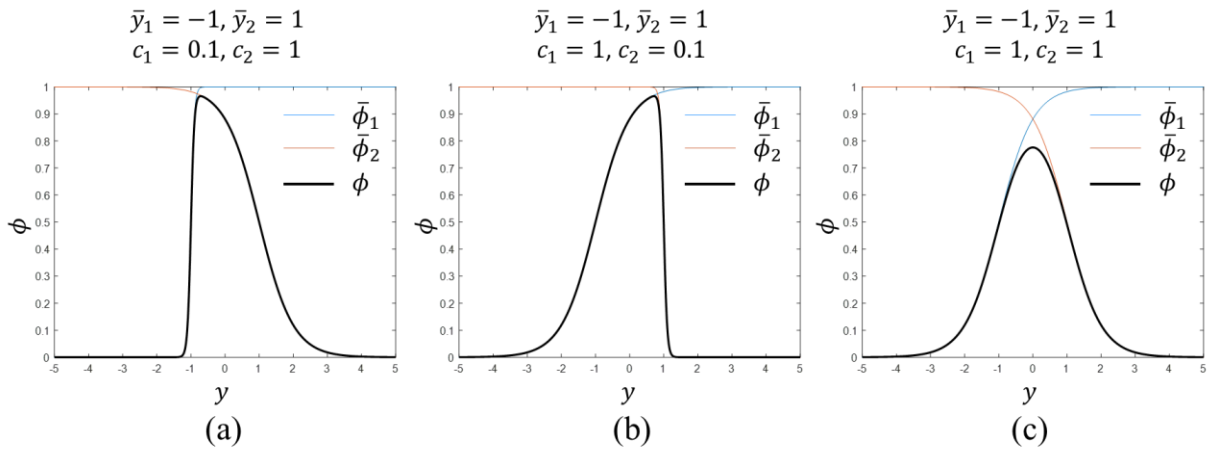

Figure 7.2. Kernel function constructed with various sets of shape control parameters: the parameters $\{\bar{y}_1, \bar{y}_2, c_1, c_2\}$ used for each case is (a) $\{-1,1,0.1,1\}$, (b) $\{-1,1,1,0.1\}$, and (c) $\{-1,1,1,1\}$.

Now consider a set of NK kernels: $\mathcal{S} = \{\phi_J\}_{J=1}^{NK}$ employed in a single block. For the kernels to possess the partition of unity, the following normalization is considered:

$$\hat{\phi}_J(y) = \frac{\phi_J(y)}{\sum_{K=1}^{NK} \phi_K(y) + \bar{\epsilon}} \tag{7.7}$$

where $\hat{\phi}_J(y)$ is the normalized NN kernel, and $\bar{\epsilon}$ is a small number introduced to control locality of the domain of influence. Figure 7.3 shows a group of normalized NN kernels with various selections of the shape control parameters.

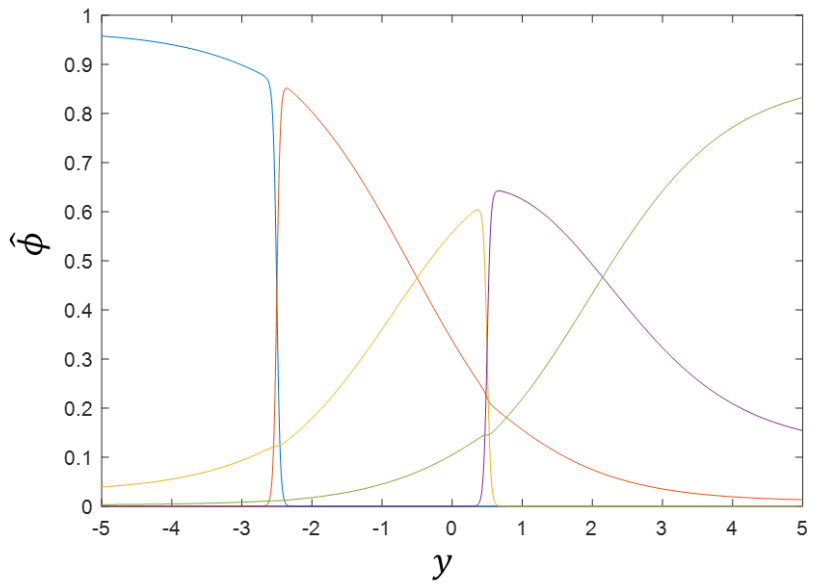

Figure 7.3. Normalized NN kernels. The parameter sets $\{\bar{y}_1, \bar{y}_2, c_1, c_2\}$ are set $\{-4, -2.5, 2, 0.5\}$, $\{-2.5, -0.5, 0.5, 2\}$, $\{-0.5, 0.5, 2, 0.5\}$, $\{0.5, 2, 0.5, 2\}$, and $\{2, 4, 2, 2\}$ for the kernels from left to right.

To introduce a weak discontinuity, one can further consider a modification of Eq. (7.6) as follows:

$$\bar{\phi}_i(y; \{\bar{y}_i, c_i, s_{1i}, s_{2i}\}) = \left(\frac{1}{2} - (-1)^i \frac{1}{2} \tanh\left(\frac{MPRELU(y - \bar{y}_i; \{s_{1i}, s_{2i}\})}{c_i}\right)\right) \tag{7.8}$$

where the modified parametric rectified linear unit (MPRELU) is defined as

$$MPRELU(y;\{s_1,s_2\}) = \begin{cases} s_1 y & z \le 0 \\ s_2 y & z > 0 \end{cases} \tag{7.9}$$

Figure 7.7 shows an example of the distribution of kernel functions with a weak discontinuity. In (7.7), introducing a small number $\bar{\epsilon}$ ensures that the NN solution affects only a region close to the localization by having the normalized kernel vanish when the evaluation point is far from the kernel center (see Figure 7.5).

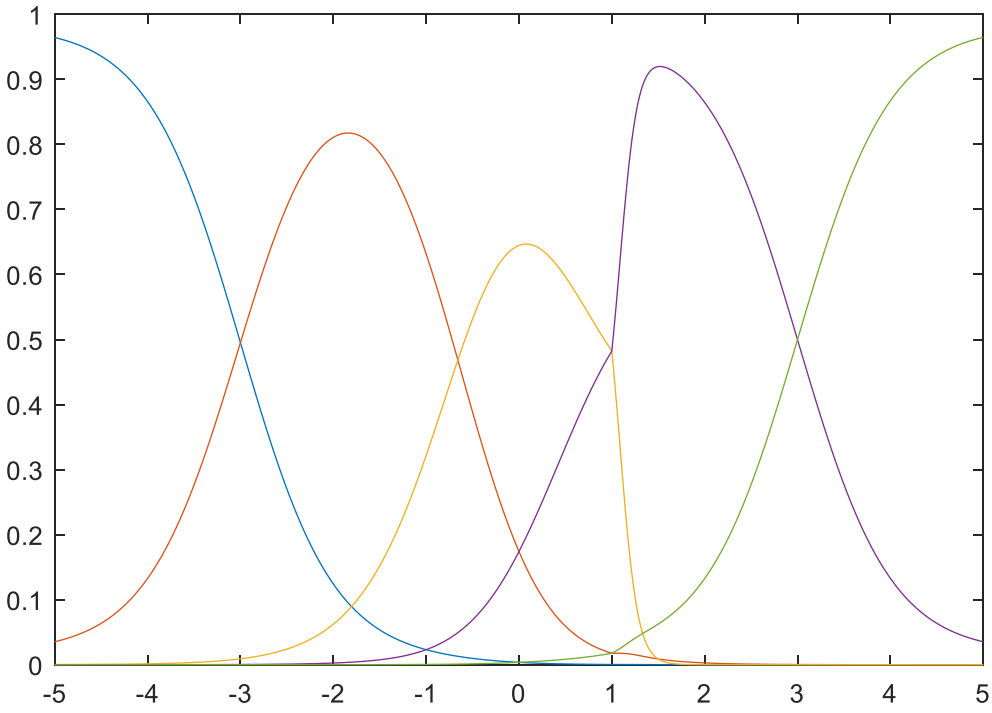

Figure 7.4. Normalized NN kernels with weak discontinuities. The parameters $\{\bar{y}_1, \bar{y}_2, c_1, c_2\}$ are set {-5, -3, 1, 1}, {-3, -1, 1, 1}, {-1, 1, 1, 1}, {1, 3, 1, 1}, and {3, 5, 1, 1} for the NN kernels from left to right. $\{s_1, s_2\} = \{0,5\}$ is applied to the NN kernel in the middle.

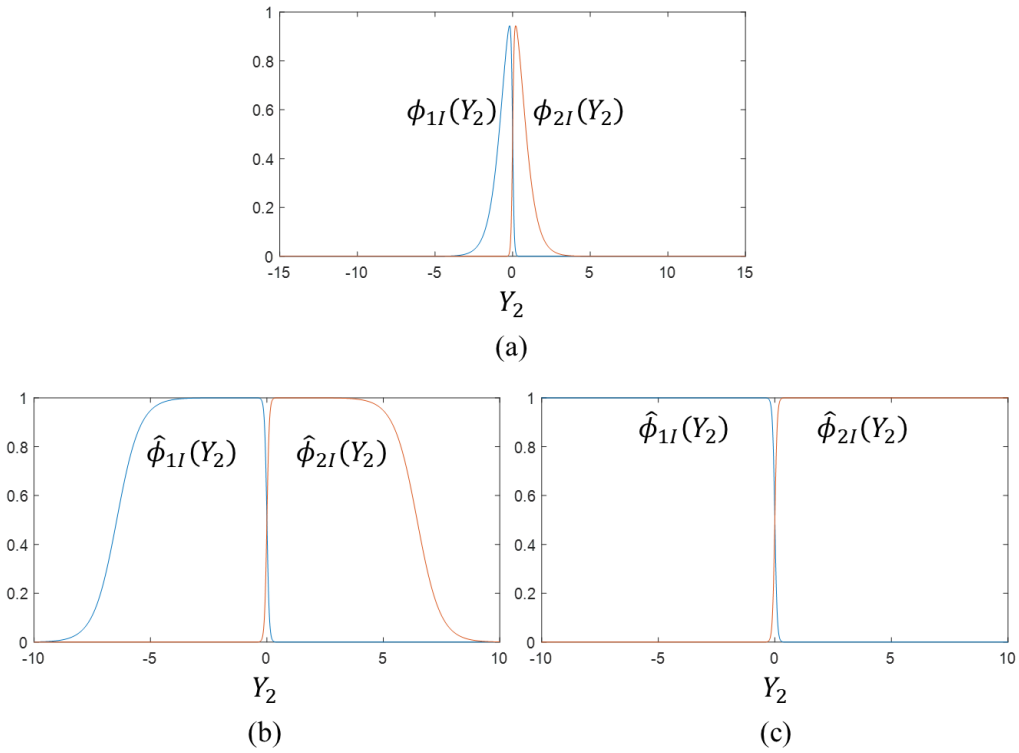

Figure 7.5. kernel functions: (a) unnormalized kernels, (b) normalized kernels with $\epsilon = 10^{-5}$, and (c) normalized kernels with $\epsilon = 0$

For a multi-block scenario, the normalization is performed as follows:

$$\hat{\phi}_{J\mathrm{A}}(x;\mathbf{W}^L,\mathbf{W}^{\mathrm{S}}) = \frac{\phi_{J\mathrm{A}}\left(y(x;\mathbf{W}^L_{\mathrm{A}});\mathbf{W}^S_{J\mathrm{A}}\right)}{\sum_{\mathrm{B}=1}^{NB}\sum_{K=1}^{NK}\phi_{K\mathrm{B}}(y(x;\mathbf{W}^L_{\mathrm{B}});\mathbf{W}^S_{K\mathrm{B}})+\bar{\epsilon}} \tag{7.10}$$

where $\hat{\phi}_{J\mathrm{A}}(x;\mathbf{W}^L,\mathbf{W}^{\mathrm{S}})$ is the J-th NN kernel in block A, $y(x;\mathbf{W}^L_{\mathrm{A}})$ is parametric coordinate constructed for block A with location-controlling parameter set $\mathbf{W}^L_{\mathrm{A}}$ (see Section 7.2.2 for parametrization), $\mathbf{W}^S_{J\mathrm{A}}$ is shape control parameter set, $\mathbf{W}^L = \{\mathbf{W}^L_{\mathrm{A}}\}^{NB}_{\mathrm{A}=1}$, and $\mathbf{W}^S = \left\{\left\{\mathbf{W}^S_{J\mathrm{A}}\right\}^{NK}_{J=1}\right\}^{NB}_{\mathrm{A}=1}$. Note that the normalization of the kernels is performed across all the blocks. This is intended to have the kernels possess the partition of unity even for the block-overlapping regions and

consequently have the polynomial completeness hold, achieving better solution accuracy than normalizing the kernels only among the kernels in the same block.

The extension of the NN kernel in (7.6) to two-dimension is straightforward:

$$\begin{aligned}\phi_K(\mathbf{y};\{\mathbf{W}_{11K}^S,\mathbf{W}_{21K}^S,\mathbf{W}_{12K}^S,\mathbf{W}_{22K}^S\}) \\ = \bar{\phi}_{11K}(y_1;\mathbf{W}_{11K}^S)\bar{\phi}_{21K}(y_1;\mathbf{W}_{21K}^S)\bar{\phi}_{12K}(y_2;\mathbf{W}_{12K}^S)\bar{\phi}_{22K}(y_2;\mathbf{W}_{22K}^S)\end{aligned} \tag{7.11}$$

where ϕ_K denotes K-th kernel and, with the shape control parameter set $\mathbf{W}_{i\alpha K}^S = \{\bar{y}_{i\alpha K}, c_{i\alpha K}\}$, and $\bar{\phi}_{i\alpha K}$ are defined as follows:

$$\bar{\phi}_{i\alpha K}\left(y_\alpha;\mathbf{W}_{i\alpha K}^S\right) = \left(\frac{1}{2} - (-1)^i\frac{1}{2}\tanh\left(\frac{(y_\alpha - \bar{y}_{i\alpha K})}{c_{i\alpha K}}\right)\right) \tag{7.12}$$

Another type of NN kernels (Type II) can be considered as follows:

$$\phi_K(\mathbf{y};\mathbf{W}^S) = \bar{\phi}(\mathbf{y})S_K(\mathbf{y};\mathbf{W}^S) \text{ for } K = 1,2, \tag{7.13}$$

where $\bar{\phi}(\mathbf{y})$ and $S_K(\mathbf{y};\mathbf{W}^S)$ are standard kernel function and regularized step function, respectively. For example, the following functions can be considered:

$$\bar{\phi}(\mathbf{y}) = \text{sech}^2(\|\mathbf{y}\|) \tag{7.14}$$

$$S_K(\mathbf{y};\mathbf{W}^S) = \frac{1}{2} + \frac{1}{2}\tanh\left((-1)^K\frac{y_2}{c}\right) \tag{7.15}$$

where $\|\mathbf{y}\| = \|\mathbf{y}\|_2 = (\mathbf{y}\cdot\mathbf{y})^{1/2}$. As shown in Figure 7.6, the above-mentioned normalized NN kernels have a sharp transition at $y_2 = 0$. This type of kernel can reduce the number of control

parameters than the kernel presented in (7.11) and (7.12), but is less flexible in capturing localizations.

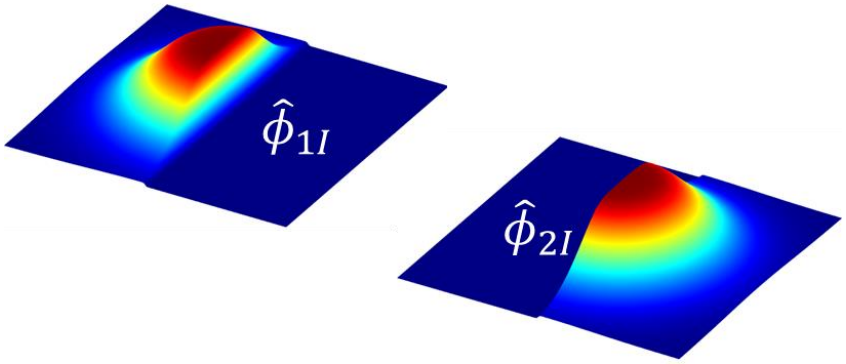

Figure 7.6. Two-dimensional NN functions (normalized with $\epsilon = 10^{-3}$)

7.2.2. Parametrization

In multi-dimensional problems, highly complex localization topology can present and the complicated localization patterns will be projected on to a low-dimensional manifold by parametric coordinates with a proper parametrization $\mathcal{P}: \mathbf{x} \rightarrow \mathbf{y}$ where $\mathbf{x} \in \mathbb{R}^d$ and $\mathbf{y} \in \mathbb{R}^d$ are physical coordinates and parametric coordinates, respectively. Figure 7.7 provides a schematic illustration where a complex localization pattern (red curves) in the physical coordinate is represented by multiple lines in a parametric coordinate. With parametrization, kernel functions defined in the low-dimensional manifold can capture complex localizations in the high-dimensional space.

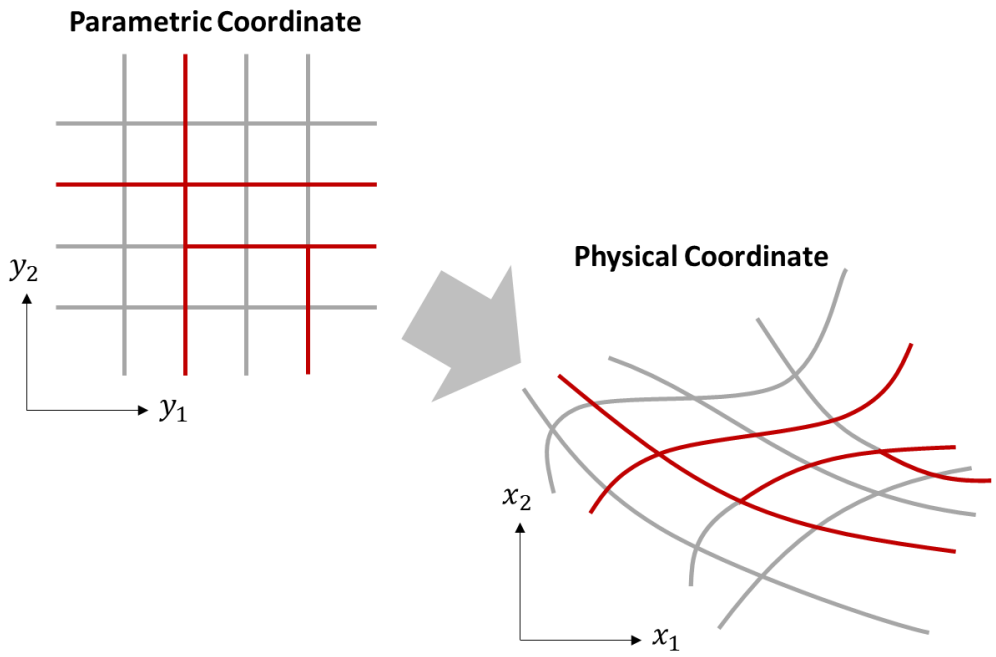

Figure 7.7. Parametric and physical coordinates: the red curves in the physical coordinate denote discontinuities. The coordinates are parametrized as shown in the right-hand side figure.

For parametrization, multiple layers with hyperbolic tangent activation function can be considered as an example. Let

$$\bar{\mathbf{y}}(\mathbf{X};\mathbf{W}_{\mathrm{A}}^{L}) = \mathbf{h}_{n_L}\left(\cdot;\mathbf{W}_{\mathrm{A}n_L}^{L}\right) \circ \mathbf{h}_{n_L-1}\left(\cdot;\mathbf{W}_{\mathrm{A}n_L-1}^{L}\right) \circ \cdots \circ \mathbf{h}_1(\mathbf{x};\mathbf{W}_{\mathrm{A}1}^{L}) \tag{7.16}$$

where $\mathbf{W}_{\mathrm{A}}^{L} = \{\mathbf{W}_{\mathrm{A}1}^{L},\ \mathbf{W}_{\mathrm{A}2}^{L}, \cdots,\ \mathbf{W}_{\mathrm{A}N}^{L}\}$ with $\mathbf{W}_{\mathrm{A}i}^{L}$ are the weights and biases of layer i of block A, N is the number of layers employed in the parameterization network, and $\mathbf{h}_i$ of i-th layer is defined as

$$\begin{aligned} \mathbf{h}_i(\boldsymbol{\xi};\mathbf{W}_{\mathrm{A}i}^{L}) &= \tanh\left(\mathbf{z}_i(\boldsymbol{\xi};\mathbf{W}_{\mathrm{A}i}^{L})\right), \qquad \text{for } i < \mathrm{N} \\ \mathbf{h}_i(\boldsymbol{\xi};\mathbf{W}_{\mathrm{A}i}^{L}) &= \mathbf{z}_i(\boldsymbol{\xi};\mathbf{W}_{\mathrm{A}i}^{L}), \qquad \text{for } i = N, \end{aligned} \tag{7.17}$$

where

$$\mathbf{z}_i(\boldsymbol{\xi}; \mathbf{W}_{\mathrm{A}i}^L) = \boldsymbol{\Theta}^{\mathrm{A}i}\boldsymbol{\xi} + \boldsymbol{\beta}^{\mathrm{A}i} \tag{7.18}$$

where $\mathbf{W}_{\mathrm{A}i}^L = \{\boldsymbol{\Theta}^{\mathrm{A}i}, \boldsymbol{\beta}^{\mathrm{A}i}\}$ with the weight matrix $\boldsymbol{\Theta}^{\mathrm{A}i}$ and the bias vector $\boldsymbol{\beta}^{\mathrm{A}i}$ and $\bar{\mathbf{y}}$ defined in (7.16) is scaled to obtain $\mathbf{y}$ as follows:

$$y_i = \frac{1}{a_i}\bar{y}_i, \qquad i = 1, \cdots, D \tag{7.19}$$

where a_i is a positive scaling factor.

7.3. Network structure details

Figure 7.8 describes the network structure considered in this work. The entire network provides the map $\mathbb{R}^D \to \mathbb{R}$ with input $\mathbf{x} \in \mathbb{R}^D$ and output $u^h \in \mathbb{R}$ where D denotes the space dimension. As the RK approximation serves on approximating the smooth part of the solution, a relatively coarse, predetermined discretization is sufficient. Since the RK shape functions do not evolve throughout the simulation, and the shape functions $\{\Psi_I(\mathbf{X})\}_{I=1}^{NP}$ is precomputed and directly inputted to the network as shown in Figure 7.8. The RK network has the RK coefficients as its weights.

Meanwhile, the NN approximation directly takes the coordinate $\mathbf{x}$ as its input. Instead of employing a densely connected deep neural network, multiple network blocks are constructed in parallel as discussed in Section 7.2, and each block has a block-level approximation (see Eq. (7.3)) as its output. Each block is built upon its own parametric coordinate, contains multiple NN kernels,

and is capable of capturing discontinuities in the regions near localizations as described in Sections 7.1 and 7.2. In this approach we consider superposition of multiple NN approximation functions, each of which represents the captured discontinuities in the NN block by its independent parametric coordinates. If highly complicated localization topology is developed in a small region, utilizing multiple NN blocks can enhance the solution accuracy.

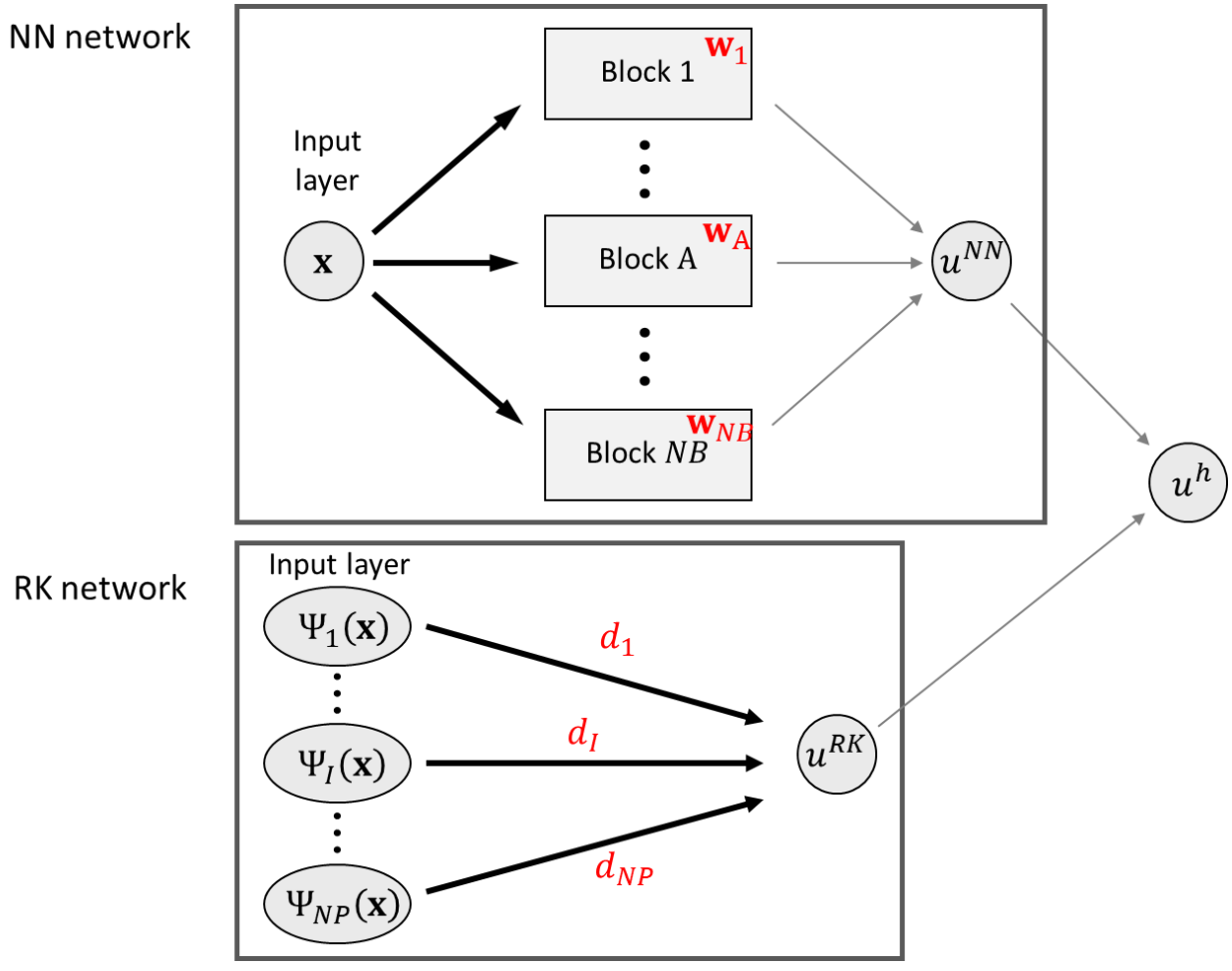

Figure 7.8. Entire network structure that incorporates the RK approximation and the NN approximation. The unknown parameters associated with each part of the network are written in red. The thick black arrows denote that the network connections entail unknown parameters and the thin grey arrows denote that the weight of the associated connection is one (1) and do not change throughout the computation.

The network structure of block A is described in Figure 7.9. The parameterization network contains the kernel function layer and the polynomial layer independently constructed. All the unknown parameters introduced in 7.2 for each part of the block are denoted as $\mathbf{W}^L$, $\mathbf{W}^S$, and $\mathbf{W}^P$ in red color. The details of polynomial subblock are presented in Figure 7.10. The neuron-wise multiplication of the polynomial layer and kernel function layer is performed by employing *tensorflow.keras.layers.multiply* available in TensorFlow. Figure 7.11 shows how the solution derivatives are computed for use in solving the potential energy minimization problem. To compute the spatial derivatives of u^{NN}, the automatic differentiation function provided by TensorFlow is utilized. To compute the spatial derivatives of u^{RK}, the input of the RK network, $\Psi_I(\mathbf{x})$ in Figure 7.8 is replaced by the pre-computed shape function derivatives $\Psi_{I,i}(\mathbf{x})$.

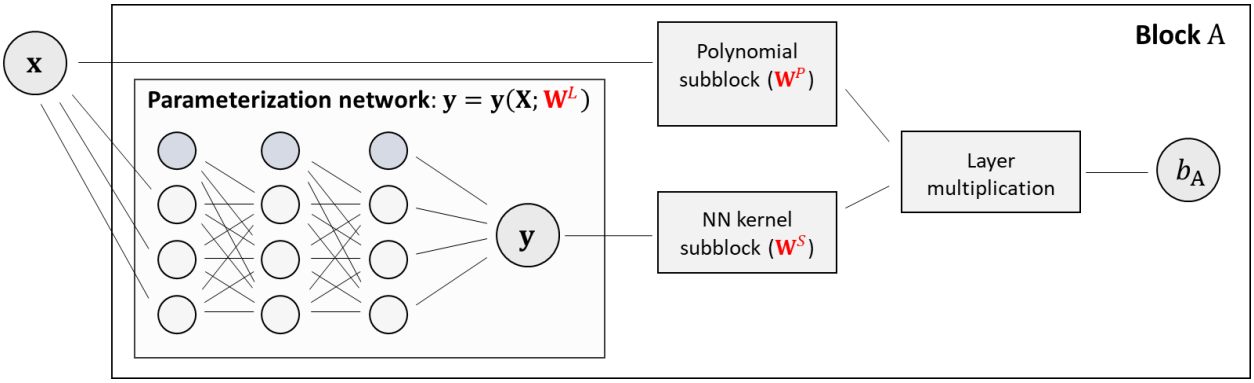

Figure 7.9. Network structure for block A. The unknown parameters introduced in each part are denoted in red color.

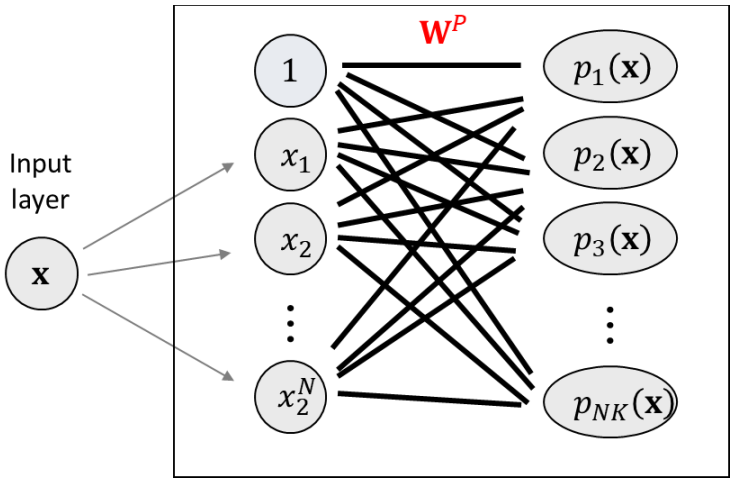

Figure 7.10. Polynomial subblock details: The thick black lines denote that the network connections entail unknown parameters and the thin grey arrows denote that the weight of the associated connection is one (1) and do not change throughout the computation.

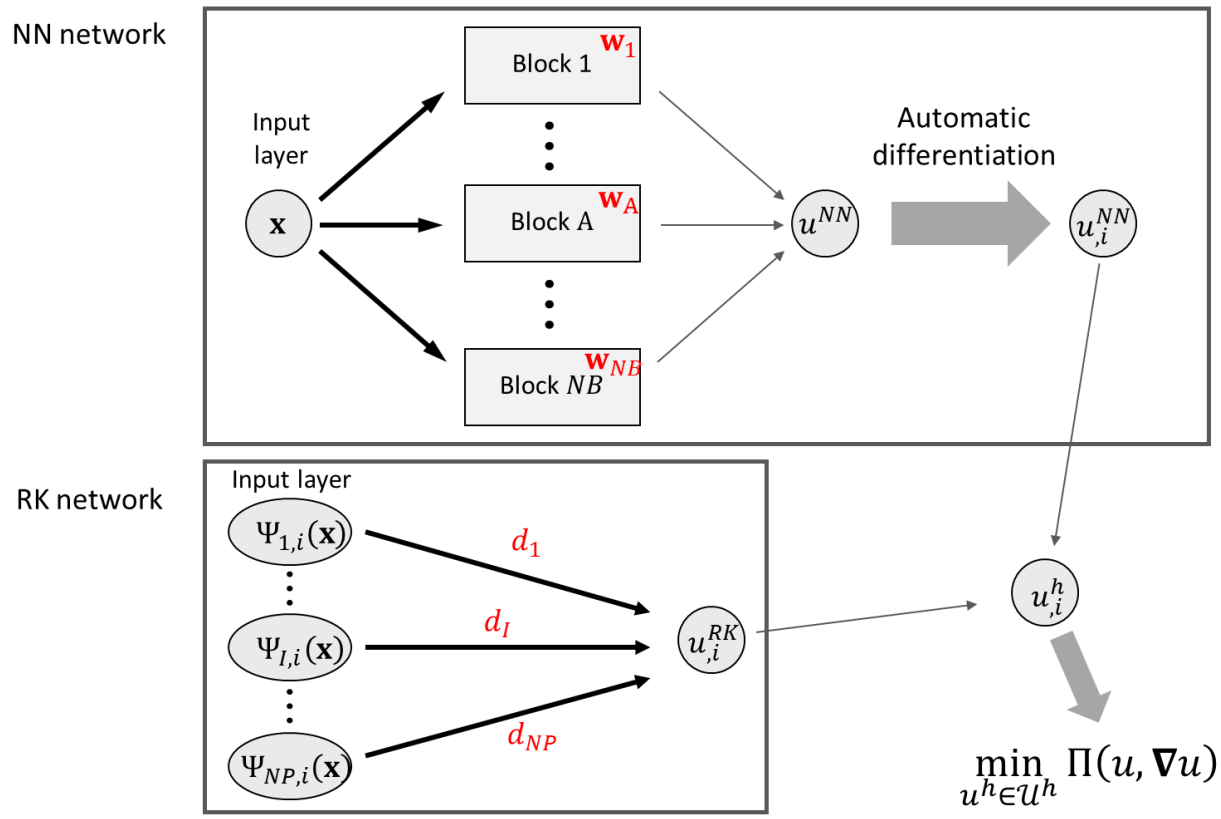

Figure 7.11. Computation of solution derivative $u_{,i}^h$: The thick black lines denote that the network connections entail unknown parameters and the thin grey arrows denote that the weight of the associated connection is one (1) and do not change throughout the computation.

The optimization problem to solve is the minimization of potential energy as follows:

$$\underset{\mathbf{d},\mathbf{W}}{\operatorname{argmin}}\, \Pi\left(\mathbf{U}^h(\mathbf{d},\mathbf{W})\right) = \int_\Omega \psi\left(\mathbf{U}^h(\mathbf{d},\mathbf{W})\right) d\Omega - F\left(\mathbf{U}^h(\mathbf{d},\mathbf{W})\right), \tag{7.20}$$

where $\mathbf{U}^h(\mathbf{d},\mathbf{W}) = \mathbf{U}^{h,RK}(\mathbf{d}) + \mathbf{U}^{h,NN}(\mathbf{W})$ is the set of approximations of independent field variables of a general multi-field formulation constructed upon the RK coefficient set $\mathbf{d}$ and the neural network weight set $\mathbf{W} = \{\mathbf{W}^L, \mathbf{W}^S, \mathbf{W}^P\}$, and ψ and F are internal energy density and external work, respectively.

The potential energy minimization problem is solved in two stages. In the first stage, the problem is solved only for the RK coefficients to find the initial guess of the RK coefficients as follows:

$$\underset{\bar{\mathbf{d}}}{\operatorname{argmin}}\, \Pi\left(\mathbf{U}^{h,RK}(\bar{\mathbf{d}})\right) = \int_\Omega \psi\left(\mathbf{U}^{h,RK}(\bar{\mathbf{d}})\right) d\Omega - F\left(\mathbf{U}^{h,RK}(\bar{\mathbf{d}})\right) \tag{7.21}$$

In this stage, the overall solution behavior including the smooth part of the solution and the boundary conditions is found by the RK approximation. Note that this leads to a standard Galerkin-based RKPM formulation and the problem can be solved by using a standard matrix solver. Since the RK approximation obtained in the first stage can oscillate around the localization due to the Gibbs-type phenomenon, the filtered RK coefficients are used as the initial guess for the next step as follows:

$$\bar{\mathbf{d}}^{fil} = \bar{\mathbf{\Psi}}\bar{\mathbf{d}}, \tag{7.22}$$

where $\bar{\mathbf{d}}^{fil}$ is the filtered RK coefficient set and $\bar{\mathbf{\Psi}}$ is the filter with its entries $\bar{\Psi}_{IJ} = \Psi_J(\mathbf{x}_I)$.

In the second stage, Eq. (7.23) is solved for both $\mathbf{d}$ and $\mathbf{W}$. The initial guess of the RK coefficients is $\mathbf{d} = \bar{\mathbf{d}}^{fil}$. The neural network weights $\mathbf{W} = \{\mathbf{W}^L, \mathbf{W}^S, \mathbf{W}^P\}$ are initialized as follows: 1) $\mathbf{W}^L$ is initialized such that the blocks are uniformly distributed over the domain, 2) $\mathbf{W}^S$ is initialized such that the kernels are uniformly distributed is uniformly distributed in the parametric coordinate of the corresponding blocks, 3) $\mathbf{W}^P = 0$ is taken for the polynomial basis parameters.

The potential energy minimization problem can be solved by a gradient descent-type optimizer. In this work, *Adam* [107], a first-order gradient-based stochastic optimizer with adaptive learning rate, is used. For the upper bound of the learning rate, the default value (10^{-3}) is initially used and the upper bound of the learning rate is decreased when severe oscillation in the loss curve is observed. In all cases presented in this work, the upper bounds between 10^{-4} and 10^{-3} yielded a stable loss curve.

7.4. Regularization

The NN-RK approximation proposed in this work can be applied to both local (e.g., Cauchy continuum) and nonlocal models (e.g., phase field formulation). If a local model is employed, the localization width may not be bounded and the NN approximation may become sensitive to the distribution of integration points. When the NN-RK approximation is applied to a nonlocal formulation, it has been observed that the network regularization introduces additional stabilization in solving the potential energy minimization problem with a model with insufficient integration point resolution.

Although the NN kernel contains the sharpness control parameter c in Eqs. (7.6), (7.12), and (7.15), the sharpness is also affected by the parametrization, more specifically, the gradient of

the parametric coordinate **y** with respect to the physical coordinate **x**. In this subsection, two methods are proposed to introduce a localization limiter into the NN approximation.

To analyze the influence of the parametrization on the transition sharpness, consider the Taylor expansion of $y_i(\mathbf{x})$ and truncate the second order and higher terms as follows.

$$y_i(\mathbf{x}) \approx y_i(\bar{\mathbf{x}}) + (\mathbf{x} - \bar{\mathbf{x}}) \cdot \left.\frac{\partial y_i}{\partial \mathbf{x}}\right|_{\mathbf{x}=\bar{\mathbf{x}}} \tag{7.23}$$

Additionally, define $\widehat{H}$ as follows.

$$\widehat{H} \equiv 1 / \left\| \frac{\partial y_i}{\partial \mathbf{x}} \right\|_{\mathbf{x}=\bar{\mathbf{x}}} \tag{7.24}$$

By substituting (7.23) into the term inside the hyperbolic tangent in (7.6), (7.12), or (7.15), we have

$$\frac{y_i - \bar{y}_i}{c} \approx \frac{(\mathbf{x} - \bar{\mathbf{x}}) \cdot \left(\left.\frac{\partial y_i}{\partial \mathbf{x}}\right|_{\mathbf{x}=\bar{\mathbf{x}}} \right)}{c}, \tag{7.25}$$

where $\bar{y}_i = y_i(\bar{\mathbf{x}})$. Then, multiply both the numerator and the denominator by $\widehat{H}$.

$$\frac{y_i - \bar{y}_i}{c} \approx \frac{(\mathbf{x} - \bar{\mathbf{x}}) \cdot \left(\widehat{H} \left.\frac{\partial y_i}{\partial \mathbf{x}}\right|_{\mathbf{x}=\bar{\mathbf{x}}} \right)}{c\widehat{H}}, \tag{7.26}$$

Note that the norm of $\widehat{H}\frac{\partial y_i}{\partial \mathbf{x}}\Big|_{\mathbf{x}=\bar{\mathbf{x}}}$ in (7.26) is unity (1) due to the definition of $\widehat{H}$ in (7.24). Hence, $(\mathbf{x}-\bar{\mathbf{x}})\cdot\left(\widehat{H}\frac{\partial y_i}{\partial \mathbf{x}}\Big|_{\mathbf{x}=\bar{\mathbf{x}}}\right)$ is a projection of $(\mathbf{x}-\bar{\mathbf{x}})$ onto a unit vector, thus, the scale of $(\mathbf{x}-\bar{\mathbf{x}})\cdot\left(\widehat{H}\frac{\partial y_i}{\partial \mathbf{x}}\Big|_{\mathbf{x}=\bar{\mathbf{x}}}\right)$ is always the same as the scale of the physical coordinate and the sharpness of the following hyperbolic tangent is solely controlled by the numerator $c\widehat{H}$.

$$\tanh\left(\frac{(\mathbf{x}-\bar{\mathbf{x}})\cdot\left(\widehat{H}\frac{\partial y_i}{\partial \mathbf{x}}\Big|_{\mathbf{x}=\bar{\mathbf{x}}}\right)}{c\widehat{H}}\right) \tag{7.27}$$

A straightforward way is to make the following modification to (7.6):

$$\bar{\phi}(y)=\left(\frac{1}{2}+\frac{1}{2}\tanh\left(\frac{(y-\bar{y})\widehat{H}}{c}\right)\right), \tag{7.28}$$

of which the hyperbolic tangent function leads to Eq. (7.27) but without $\widehat{H}$ in the denominator, and the sharpness is entirely controlled by c. Therefore, imposing a lower limit constraint on c is sufficient for regularization (Type I regularization). The complexity in the implementation of this approach depends on the complexity of the parametrization network as the derivative of the parametric coordinate y is directly used. One can consider using the automatic differentiation, but it might deteriorate the computational efficiency.

Another approach for regularization is to impose certain constraints on the weights of the parametrization network such that $\widehat{H}$ has a lower bound (Type II regularization), which is relatively easier than the first approach as it does not require computing the spatial derivative of y. To achieve this, first estimate the lower limit of $\widehat{H}$ in terms of the weights of the parametric

network. The derivation provided here is based on Type II NN kernel, but the generalization is straightforward. The derivative of y_2 with respect to $\mathbf{x}$ is as follows.

$$\frac{\partial y_2}{\partial \mathbf{x}} = \frac{1}{a_2}\frac{\partial \bar{y}_2}{\partial \mathbf{x}} = \frac{1}{a_2}\frac{\partial \bar{y}_2}{\partial \mathbf{h}_{n_L-1}} \cdot \cdots \cdot \frac{\partial \mathbf{h}_2}{\partial \mathbf{h}_1} \cdot \frac{\partial \mathbf{h}_1}{\partial \mathbf{x}}, \tag{7.29}$$

where the functions $\mathbf{h}_i$ are defined in (7.24). With the hyperbolic tangent activation, the r-th row of last term in (7.29), $\partial h_1^r/\partial \mathbf{x}$, can be written as

$$\frac{\partial h_1^r}{\partial \mathbf{x}} = \operatorname{sech}^2(h_1^r)\frac{\partial z_1^r}{\partial \mathbf{x}} = \operatorname{sech}^2(h_1^r)\,\boldsymbol{\Theta}_r^1 \tag{7.30}$$

where $z_L^r = \sum_{k=1}^{D} \Theta_{rk}^L x_k + \beta_r^L$ is defined with the weight matrix $\boldsymbol{\Theta}^L$ and the bias vector $\boldsymbol{\beta}^L$ of layer L, and $\boldsymbol{\Theta}_r^L$ is the r-th row of $\boldsymbol{\Theta}^L$. In (7.30), the duplicated indices do not imply summation.

Let us consider the following constraint.

$$\|\boldsymbol{\Theta}_r^1\| \le C_1, \tag{7.31}$$

where C_1 is a constant. Then,

$$\begin{aligned}\left\|\frac{\partial y_2}{\partial \mathbf{x}}\right\| = \frac{1}{a_2}\left\|\frac{\partial \bar{y}_2}{\partial \mathbf{x}}\right\| = \frac{1}{a_2}\left\|\sum_{r=1}^{n_N^1}\frac{\partial \bar{y}_2}{\partial h_1^r}\frac{\partial h_1^r}{\partial \mathbf{x}}\right\| &\le \frac{1}{a_2}\sum_{r=1}^{n_N^1}\left\|\frac{\partial \bar{y}_2}{\partial h_1^r}\frac{\partial h_1^r}{\partial \mathbf{x}}\right\| \le \frac{1}{a_2}\sum_{r=1}^{n_N^1}\left|\frac{\partial \bar{y}_2}{\partial h_1^r}\right|\left\|\frac{\partial h_1^r}{\partial \mathbf{x}}\right\| \\ &= \frac{1}{a_2}\sum_{r=1}^{n_N^1}\left|\frac{\partial \bar{y}_2}{\partial h_1^r}\right| \operatorname{sech}^2(h_1^r)\,\|\boldsymbol{\Theta}_r^1\|,\end{aligned} \tag{7.32}$$

where n_N^L is the number of neurons at layer L. By utilizing (7.31) and $\operatorname{sech}^2(\cdot) \le 1$, (7.32) becomes

$$\left\|\frac{\partial y_2}{\partial \mathbf{x}}\right\| \le \frac{C_1}{a_2}\sum_{r=1}^{n_N^1}\left|\frac{\partial \bar{y}_2}{\partial h_1^r}\right| = \frac{C_1}{a_2}\left\|\frac{\partial \bar{y}_2}{\partial \mathbf{h}_1}\right\|_1 \le \frac{C_1\sqrt{n_N^1}}{a_2}\left\|\frac{\partial \bar{y}_2}{\partial \mathbf{h}_1}\right\|, \tag{7.33}$$

where $\|\mathbf{z}\|_1 = \sum_{i=1}^{n} z_i$ is 1-norm of $\mathbf{z}$ with dimension n and $\|\mathbf{z}\|_1 \le \sqrt{n}\|\mathbf{z}\|_2$ is utilized. Now, we introduce the constraint in (7.31) to all layers.

$$\|\boldsymbol{\Theta}_r^L\| \le C_L, \qquad L = 1 \cdots n_N^L \tag{7.34}$$

By iterating the procedure performed in (7.32) and (7.33), the following inequality is obtained.

$$\left\|\frac{\partial y_2}{\partial \mathbf{x}}\right\|_{\mathbf{x}=\bar{\mathbf{x}}} \le \max_{\mathbf{x}}\left\|\frac{\partial Y_2}{\partial \mathbf{x}}\right\| \le \frac{1}{a_2}\prod_{L=1}^{n_L} C_L\sqrt{n_N^L} \equiv \frac{1}{\widehat{\widehat{H}}} \tag{7.35}$$

From (7.24) and (7.35),

$$\frac{1}{\left\|\frac{\partial y_2}{\partial \mathbf{x}}\right\|_{\mathbf{x}=\bar{\mathbf{x}}}} = \widehat{H} \ge \widehat{\widehat{H}}, \tag{7.36}$$

which leads to

$$\widehat{H}c \ge \widehat{\widehat{H}}\hat{\hat{c}}, \tag{7.37}$$

with an additional constraint

$$c \ge \hat{\hat{c}} \tag{7.38}$$

Note that the left-hand side of (7.37) is the denominator of the last term in (7.26). Therefore, by enforcing the constraints (7.34) and (7.38), the hyperbolic tangent function is regularized with the localization limit of $\widehat{\widehat{H}}\hat{\hat{c}}$. The constraints on the weight matrices are imposed by using *MinMaxNorm* provided in TensorFlow, which is trivial to implement. Compared to Type I regularization, the implementation of Type II regularization is much easier and computationally more efficient. Note that, as the Type II regularization constrains the weights of NN, the function space with the constrained parametrization network becomes less flexible.

7.5. Numerical Examples

A series of numerical examples is presented to demonstrate the localization capturing ability of the proposed method including automatic detection of localization locations and orientations, as well as the effectiveness of regularization. To construct the RK shape functions, the linear monomial basis functions and the cubic B-spline kernel function with normalized support size of 2.0 are used unless otherwise specified. For the numerical integration, the Gauss quadrature is employed. The distribution of the quadrature cells is described in each example. To minimize the total potential energy, *Adam*, a first-order gradient-based stochastic optimizer is used. The step size upper bound α of *Adam* used in this study is given in each numerical example. For the imposition of Dirichlet boundary conditions, $\beta = 1000$.

7.5.1. Pre-degraded one-dimensional elastic bar

The following one-dimensional elastic bar problem is considered to investigate how the individual NN block approximations play a role in capturing localizations.

$$\min \Pi = \int_{-1}^{+1} \frac{1}{2} E(x) u(x)_{,x}^2 - u(x) b(x)\, dx + \frac{1000E}{2h} [(u(-1) - g_1)^2 + (u(1) - g_2)^2] \tag{7.39}$$

where E, b, h, and g_i are Young's modulus, body force, RK nodal spacing, and Dirichlet boundary value, respectively. The Dirichlet boundary values $g_1 = 0$ and $g_2 = 0.5$ are used. As shown in Figure 7.12, the material is pre-degraded locally with small Young's modulus and the bar is subjected to a smooth body force:

$$E(x) = E_0\left[1.0 - \sum_{k=1}^{3} 0.99\,\mathrm{sech}\left(\frac{\max(0, |x - \bar{x}_k| - 0.002)}{0.01}\right)\right] \tag{7.40}$$

with $(\bar{x}_1, \bar{x}_2, \bar{x}_3) = (-0.65, -0.21, 0.55)$, and

$$b(x) = 10\sin 3\pi x. \tag{7.41}$$

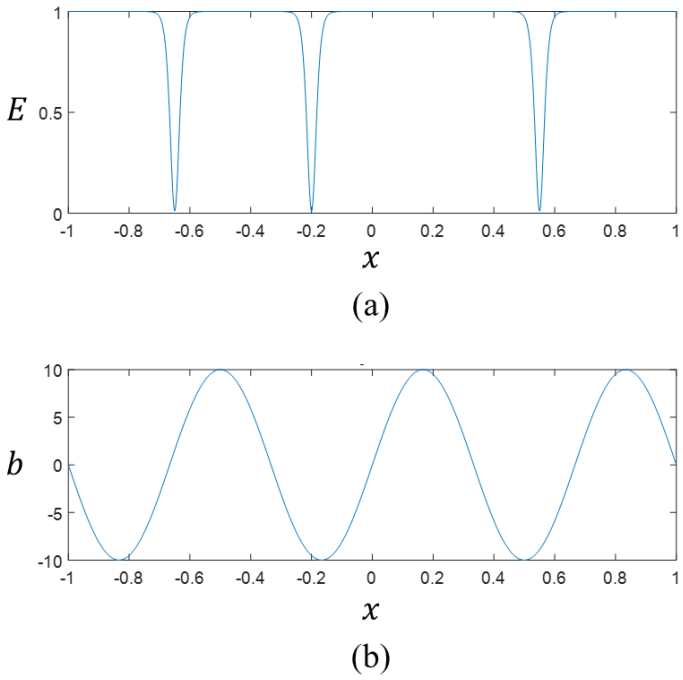

Figure 7.12. One-dimensional elasticity: (a) Young's modulus distribution and (b) body force distribution

The RK approximation space is constructed by 21 equally spaced RK points. Also uniformly distributed 500 quadrature cells are employed and the two-point Gauss quadrature is used for each cell. Four NN blocks are initially uniformly distributed with quadratic monomial bases which amount to 36 total unknowns. The NN kernels are uniformly distributed throughout the domain at the initial stage and the monomial coefficients are initialized to be zero, which means

that the neural network initially does not have any information on the localizations. Note that the domain is discretized by only 21 RK nodes. This is purposely done as the sharp transition is solely taken care of by the neural network and the RK approximation only targets the smooth part.

Figure 7.13 shows the total solution, NN approximation, and RK approximation. As expected, the NN approximation captures the very sharp solution transition while the RK approximation represents the overall smooth solution. As shown in Figure 7.14, the pure RK solution achieves a similar resolution with 801 unknowns while the transitions are insufficiently sharp even with 201 and 401 nodes while the NN-enhanced approximation agrees very well with the exact solution with 57 unknowns, which is 93% reduction in the number of unknowns. The number of unknowns required to capture localizations in multi-dimensional problems will be much more pronounced and the proposed approach is expected to be more effective compared to the standard RK approximation. Figure 7.15 shows the block-level approximation where each block locally influences the solution and captures nearby localizations.

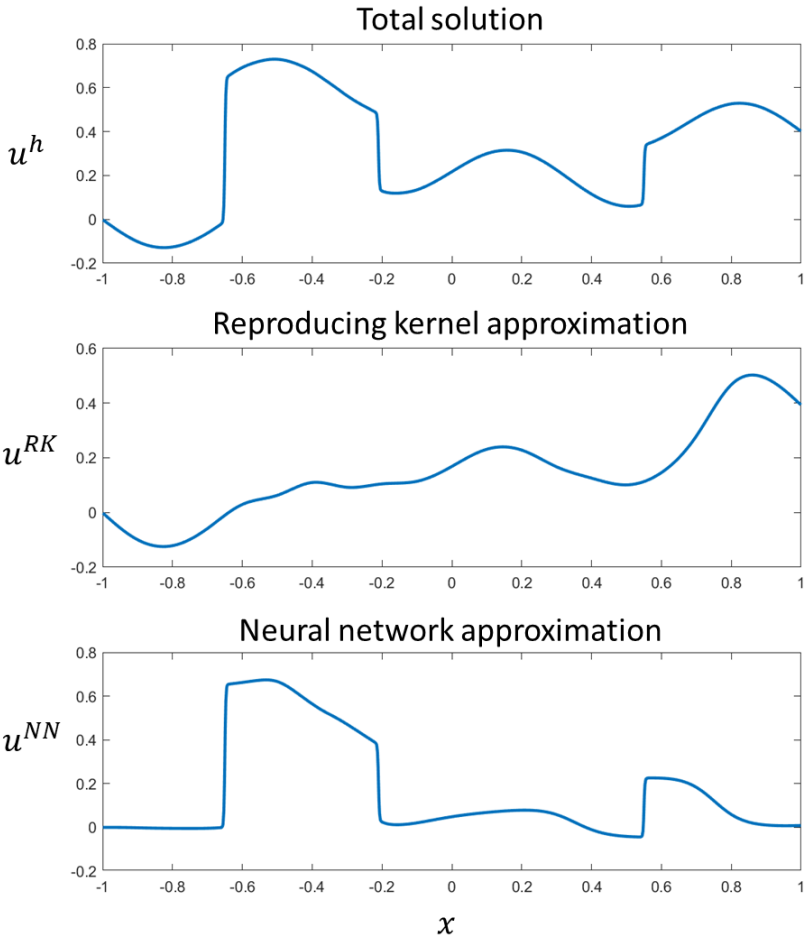

Figure 7.13. Numerical solution of one-dimensional problem: total solution, NN approximation, and RK approximation

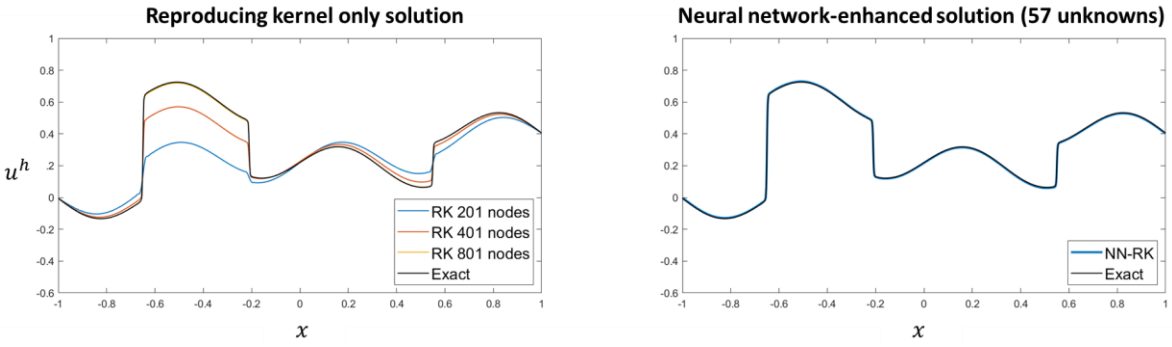

Figure 7.14. Pure RK solution (left) and NN-enhanced RK solution (right)

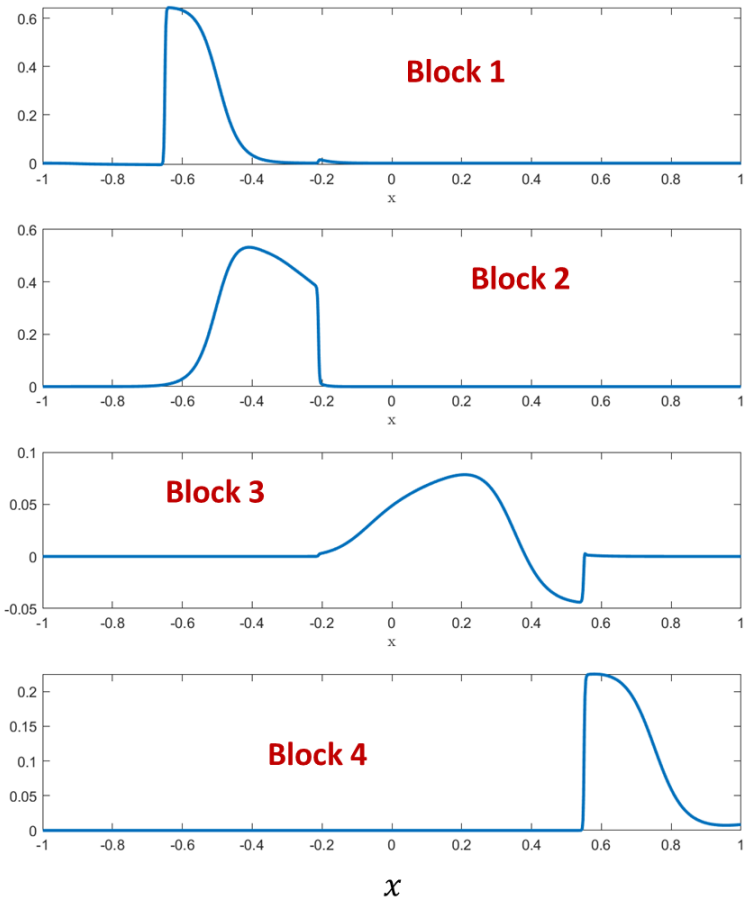

Figure 7.15. Block-level approximations

7.5.2. Two-dimensional elasticity with pre-degraded material

To demonstrate the capability of the proposed method to capture the geometry of localizations, a two-dimensional elastic specimen under tension with the locally pre-degraded shear modulus is considered as shown in Figure 7.16. For the RK approximation, the domain is uniformly discretized with 256 RK points. 2×2 Gauss quadrature is used with 3600 quadrature cells which uniformly divide the domain. For NN approximation, four blocks are randomly populated at the initial stage. For the parametrization network, two hidden layers with the

hyperbolic tangent activation and four neurons per layer are employed. For each block-level approximation, quadratic polynomial basis functions are employed. The total number of unknowns is 780, consisting of 512 RK unknowns and 268 NN unknowns.

Figure 7.17 shows the numerical solutions including the total solution, RK approximation, and NN approximation. Similar to the one-dimensional example, the total solution captures the sharp solution transition very well, primarily due to the NN approximation as shown in Figure 7.17 (c) and (f). Figure 7.18 shows the evolution of the NN approximation, u_2^{NN}, at different epochs. Since the information on the localization is not prescribed in the NN approximation, each NN block does not approximate the localization accurately at an early stage of the simulation. However, the block-level approximations gradually evolve and successfully capture the localization during the total potential energy minimization procedure as discuss in Section 7.1. Figure 7.19 shows all the NN kernel functions used in this simulation. Each pair of NN kernel functions in each NN block covers a segment of the localization and has a sharp decrease in the NN kernel function value along the curved path $y_2^I = 0$.

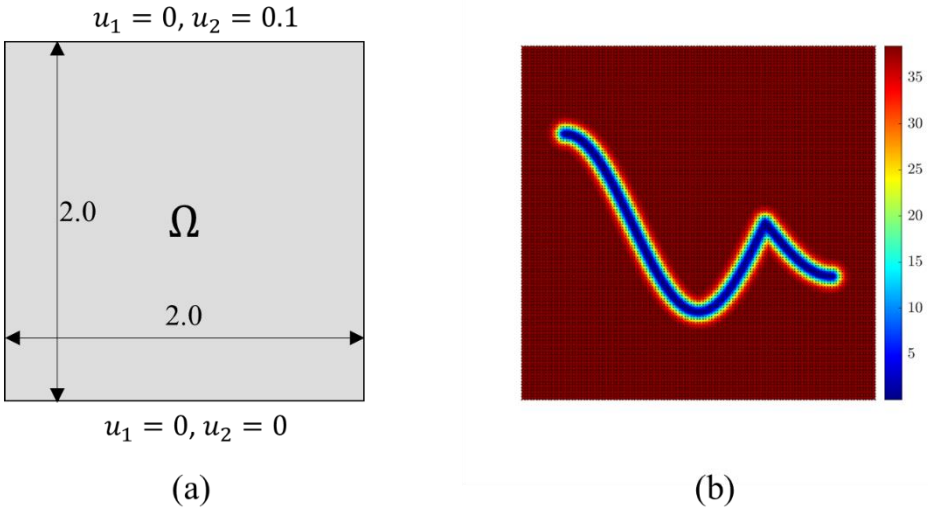

Figure 7.16. Problem setting of two-dimensional elasticity: (a) model geometry and boundary conditions and (b) shear modulus distribution

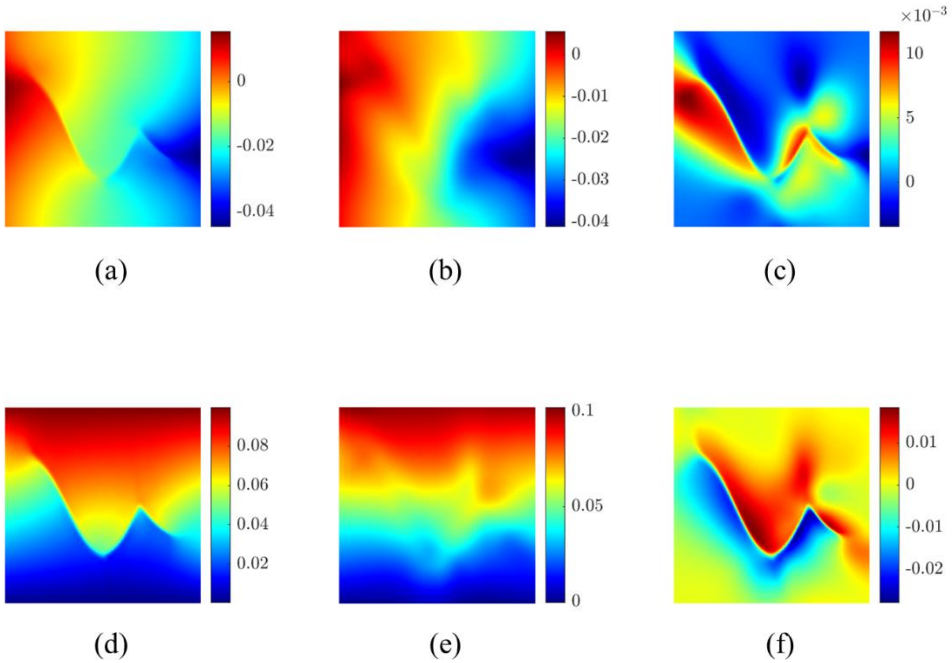

Figure 7.17. Numerical solution of two-dimensional elasticity problem: (a) u_1^h, (b) u_1^{RK}, (c) u_1^{NN}, (d) u_2^h, (e) u_2^{RK}, (f) u_2^{NN}

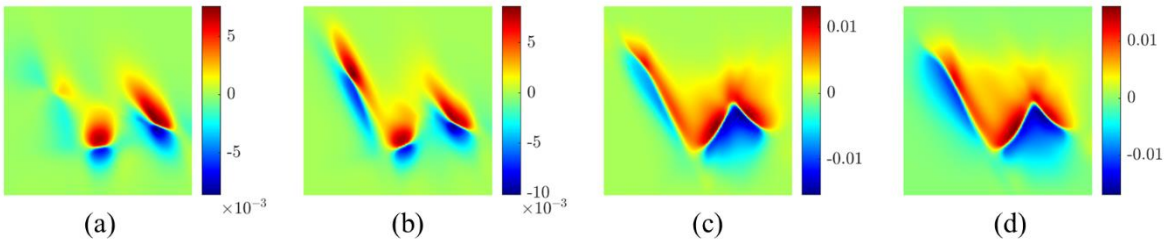

Figure 7.18. The evolution of u_2^{NN}: (a) 500-th epoch, (b) 1000-th epoch, (c) 2000-th epoch, (d) 5000-th epoch

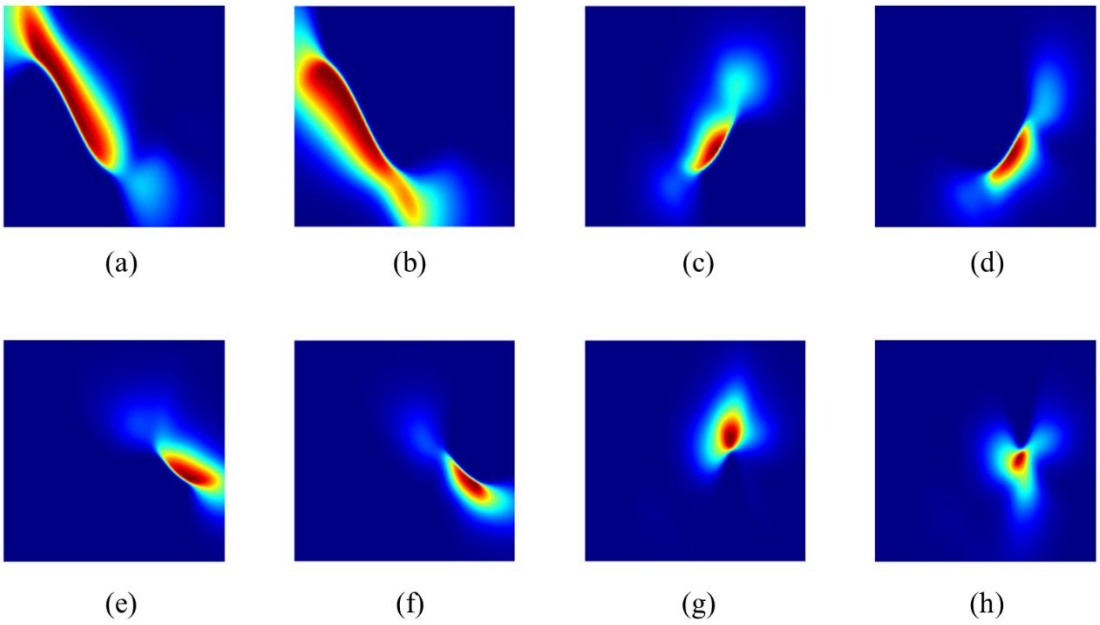

Figure 7.19. NN kernel functions at 13000-th epoch: (a) $\hat{\phi}_{11}$, (b) $\hat{\phi}_{21}$, (c) $\hat{\phi}_{12}$, (d) $\hat{\phi}_{22}$, (e) $\hat{\phi}_{13}$, (f) $\hat{\phi}_{23}$, (g) $\hat{\phi}_{14}$, (h) $\hat{\phi}_{24}$

Next, let us consider a domain with a pre-degraded zone that includes a triple junction (Case 2) as shown in Figure 7.20. The material properties and RK discretization are the same as the previous example. For NN approximation, six (6) NN blocks are used with the initial block distribution shown in Figure 7.21. The initial center positions of the blocks are uniformly

distributed throughout the domain while the orientations are randomly chosen. As shown in Figure 7.22 - Figure 7.24, the NN kernels evolve and the sharp transition in the kernels are correctly located on the degraded zone. Consequently, the sharp solution transition along the branching curves is well-captured as shown in Figure 7.25.

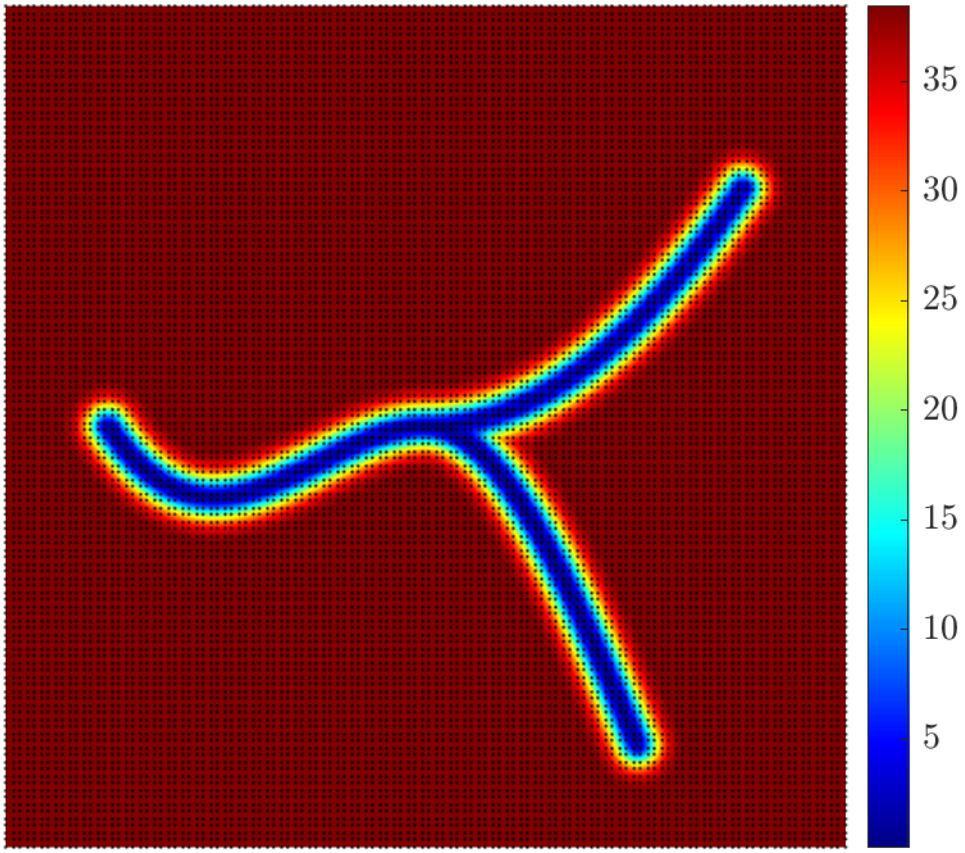

Figure 7.20. Shear modulus distribution (Case 2): the pre-degraded zone includes a triple junction.

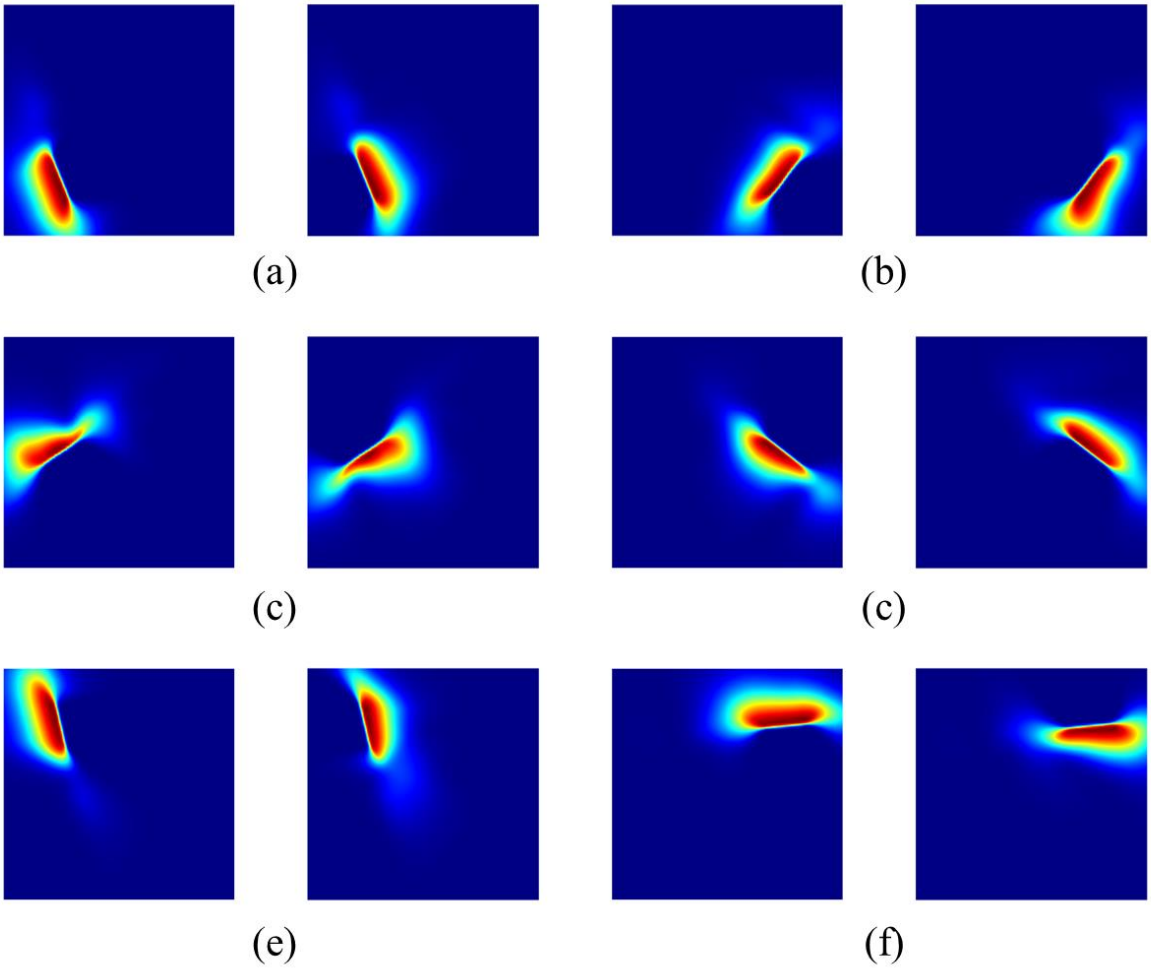

Figure 7.21. NN kernels at the initial states: (a) block 1, (b) block 2, (c) block 3, (d) block 4, (e) block 5, and (f) block 6

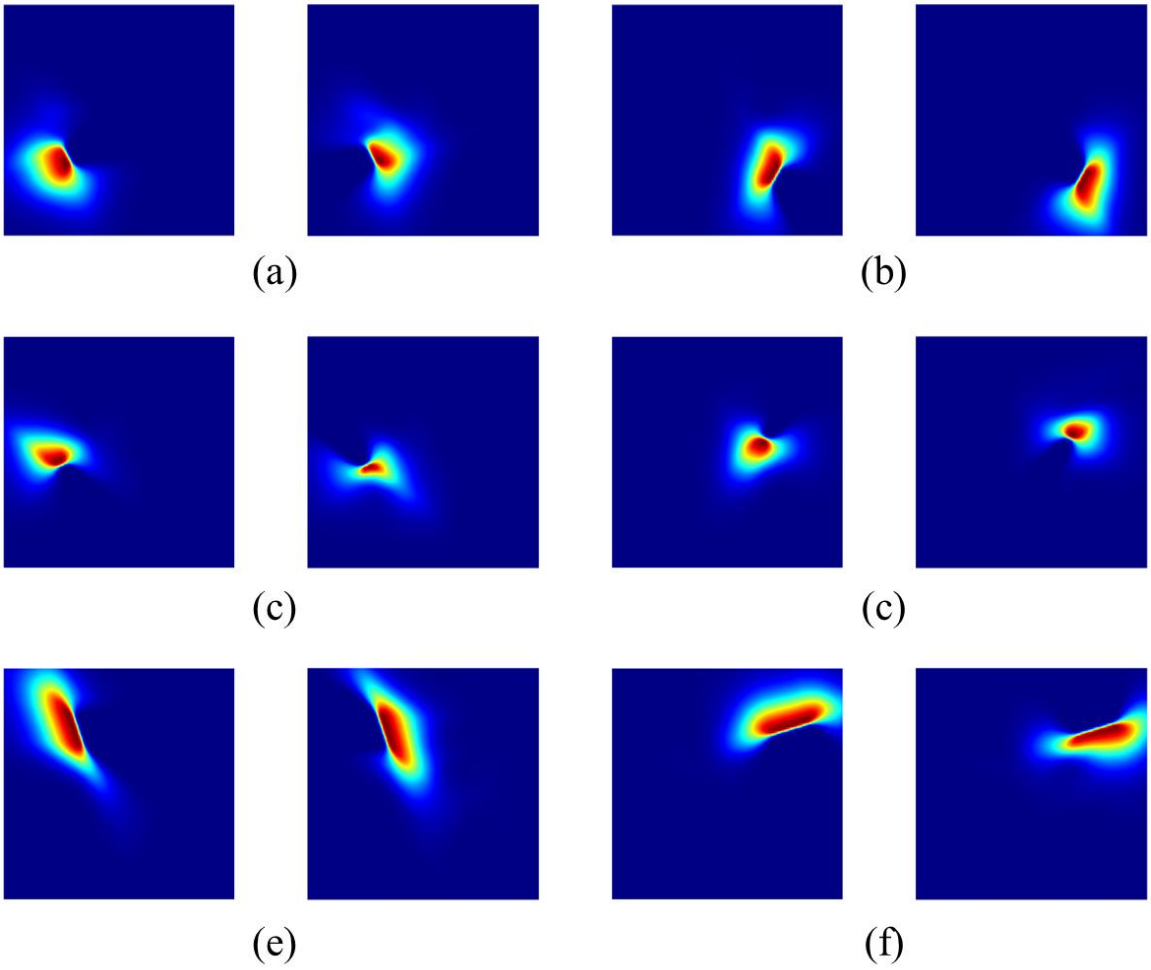

Figure 7.22. NN kernels at epoch 500: (a) block 1, (b) block 2, (c) block 3, (d) block 4, (e) block 5, and (f) block 6

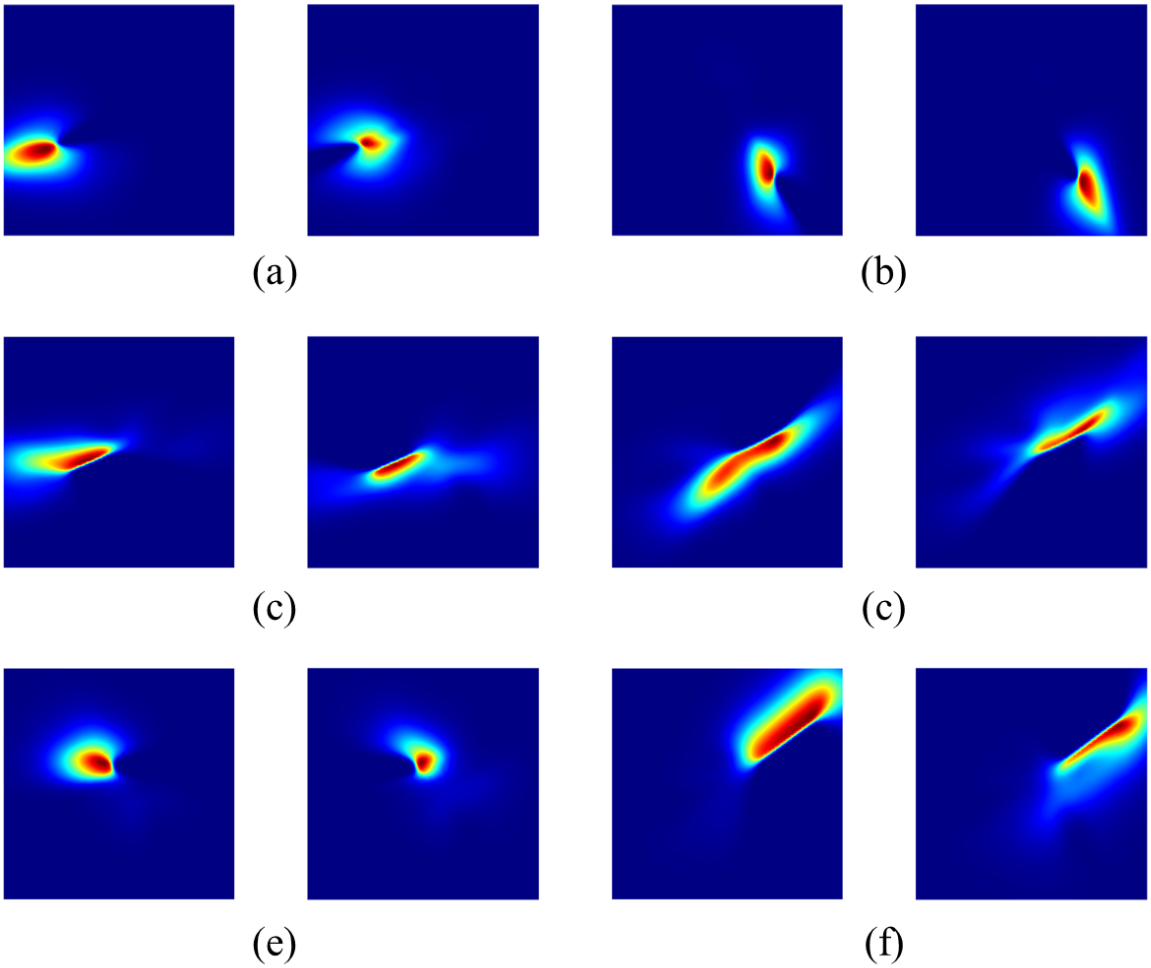

Figure 7.23. NN kernels at epoch 1000: (a) block 1, (b) block 2, (c) block 3, (d) block 4, (e) block 5, and (f) block 6

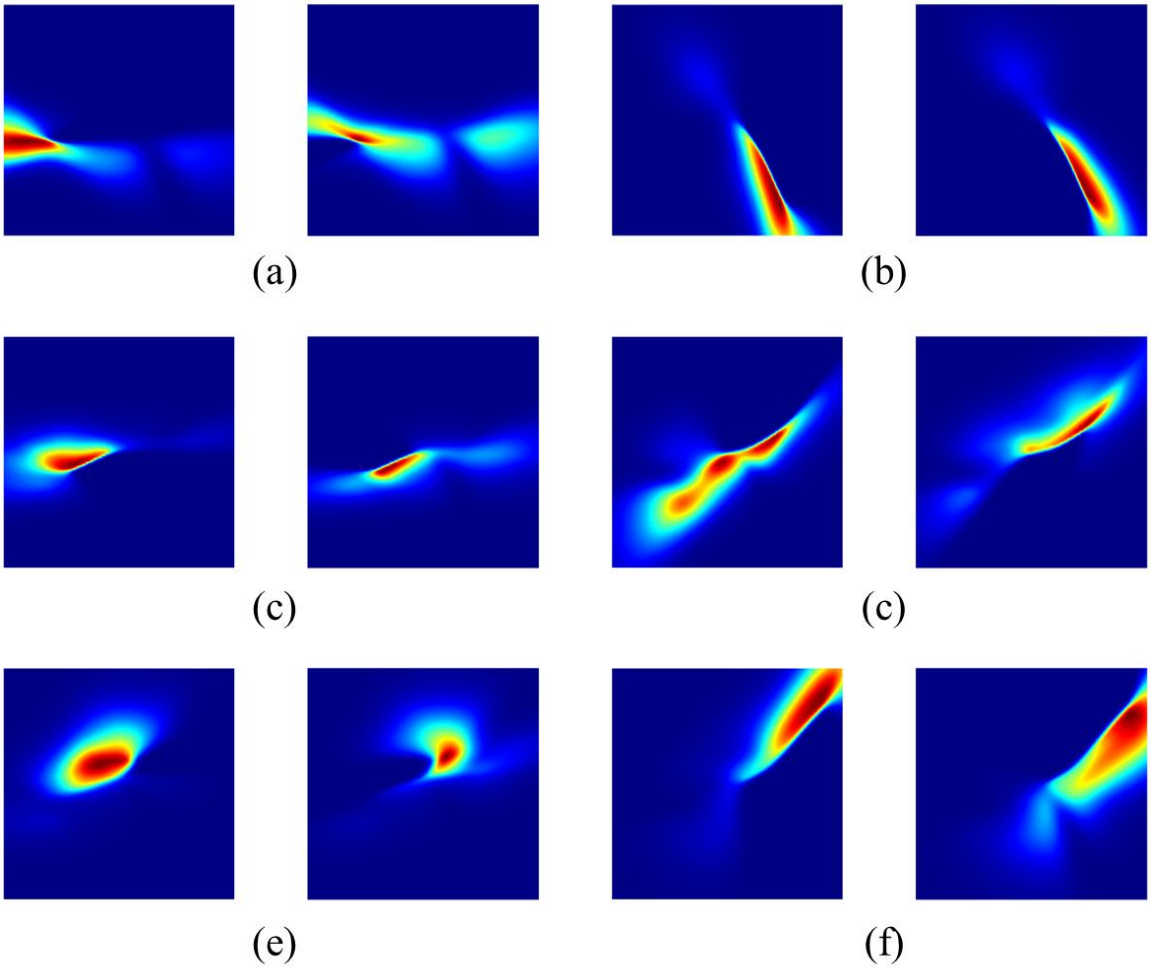

Figure 7.24. NN kernels at epoch 12000: (a) block 1, (b) block 2, (c) block 3, (d) block 4, (e) block 5, and (f) block 6

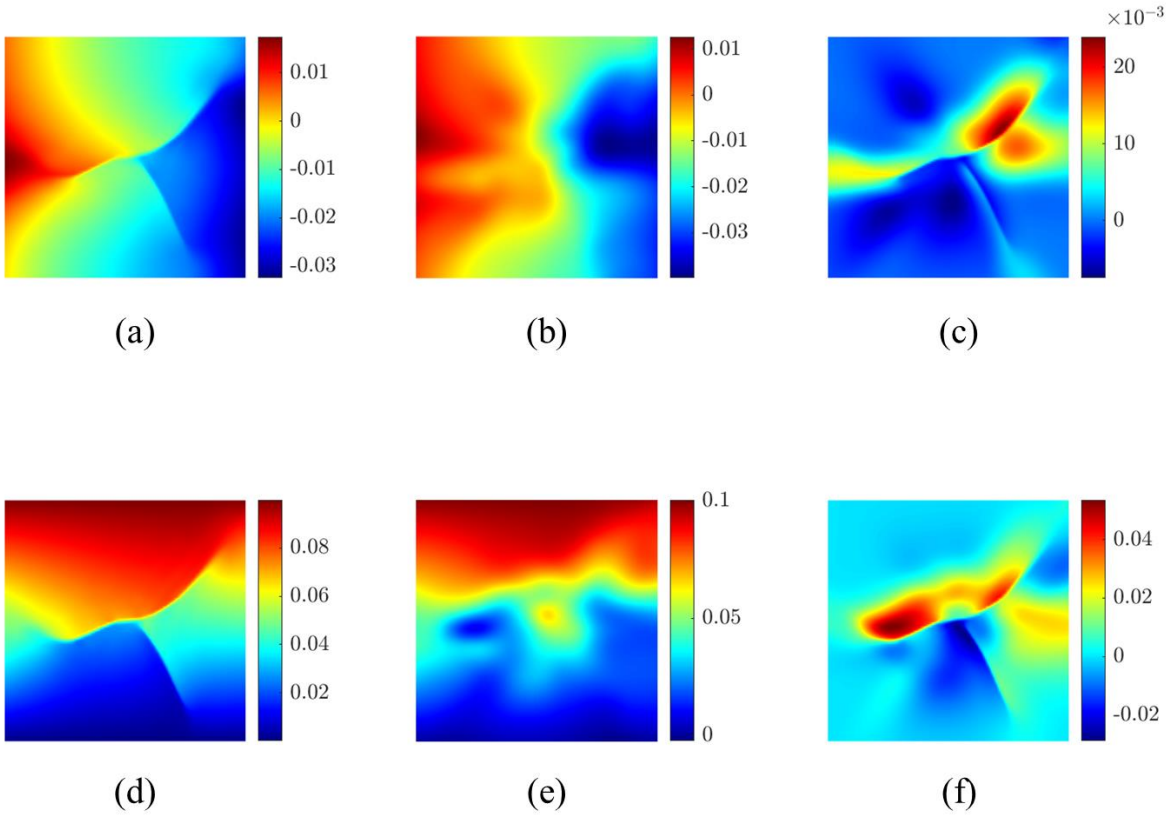

Figure 7.25. Numerical solution of two-dimensional elasticity problem (case 2): (a) u_1^h, (b) u_1^{RK}, (c) u_1^{NN}, (d) u_2^h, (e) u_2^{RK}, (f) u_2^{NN}

7.5.3. Damage Propagation: A Simple-sheared Pre-notched Problem

A pre-notched specimen under simple shear as shown in Figure 7.26(a) is considered with the following potential functional.s

$$\Pi(\mathbf{u}) = \psi_0^- + g(\eta)(\psi_0^+ - \psi_c) + \psi_c + D(\eta) \tag{7.42}$$

where, η, $g(\eta)$, $D(\eta)$, and ψ_c are damage, degradation function, dissipation functional, and critical fracture energy density for damage initiation, respectively, and, with the principal strain $\bar{\boldsymbol{\varepsilon}}$, we have

$$\psi_0^+ = \mu\langle\bar{\varepsilon}_i\rangle\langle\bar{\varepsilon}_i\rangle + \frac{\lambda}{2}\langle\bar{\varepsilon}_i\bar{\varepsilon}_i\rangle \tag{7.43}$$

$$\psi_0^- = \psi_0 - \psi_0^+ \tag{7.44}$$

with

$$\psi_0 = \frac{2\mu + \lambda}{2}\bar{\varepsilon}_i\bar{\varepsilon}_i. \tag{7.45}$$

In (7.43), μ and λ are Lamé's first and second parameters, respectively, and $\langle\cdot\rangle = \max(\cdot, 0)$ are Macaulay brackets. Additionally, the following degradation functional $g(\eta)$ and dissipation functional $D(\eta)$ are employed.

$$g(\eta) = (1-\eta)^2 \tag{7.46}$$

$$D(\eta) = \frac{p}{2}\eta^2 \tag{7.47}$$

with model constant p. Damage η has the following functional form.

$$\eta = \frac{2\kappa}{2\kappa + p} \tag{7.48}$$

where κ is defined as

$$\kappa = \langle \mathcal{H} - \psi_c \rangle \tag{7.49}$$

Here, the history variable $\mathcal{H}$ is the maximum ψ_0^+ that the material point has been experienced.

Note that (7.42) is equivalent to the potential functional for phase field fracture proposed in [101] except for the term involving the gradient of damage. In the absence of the gradient term, this damage model is a local model. Instead, the regularization is introduced by regularizing the NN approximation as discussed in Section 3.4. The model constant p is estimated as

$$p = \frac{6\mathcal{G}_c}{\bar{\ell}}, \tag{7.50}$$

where $\mathcal{G}_c$ and $\bar{\ell}$ are fracture energy and localization limit, respectively. In this work, as used in [91, 108], Young's modulus of 210 GPa, Poisson's ratio of 0.3, and $\mathcal{G}_c$=2.7 N/mm are chosen, and $\bar{\ell}$=0.01667 mm is used by selecting a_2=3.0, C_L=3.0, and $\ell_I = 0.15$. Material is pre-degraded as shown in Figure 7.26(b). The domain is uniformly discretized by 256 RK nodes for the RK approximation and four NN blocks are used with cubic basis for the NN approximation. The total number of unknowns is 790, including 512 RK unknowns and 278 NN unknowns. The Gauss quadrature points used for this simulation are plotted in Figure 7.26(b). Figure 7.27 shows the evolution of damage produced by the increase of g. The series of results demonstrates that the proposed method is also capable to capture evolving localizations including the damage and the sharp transition in u_1^h and u_2^h across the localization, which is a promising result. The angle of crack path of 63° degrees compares well with the initial angle of 65° reported in [108].

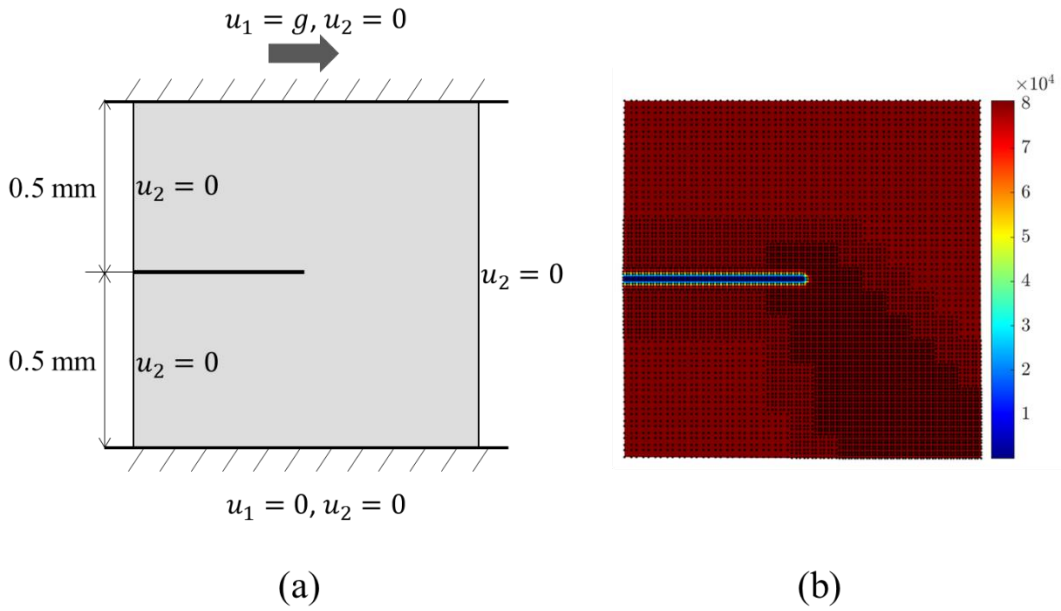

Figure 7.26. Problem setting of elastic-damage problem: (a) geometry and boundary conditions and (b) pre-degraded shear modulus and Gauss integration points

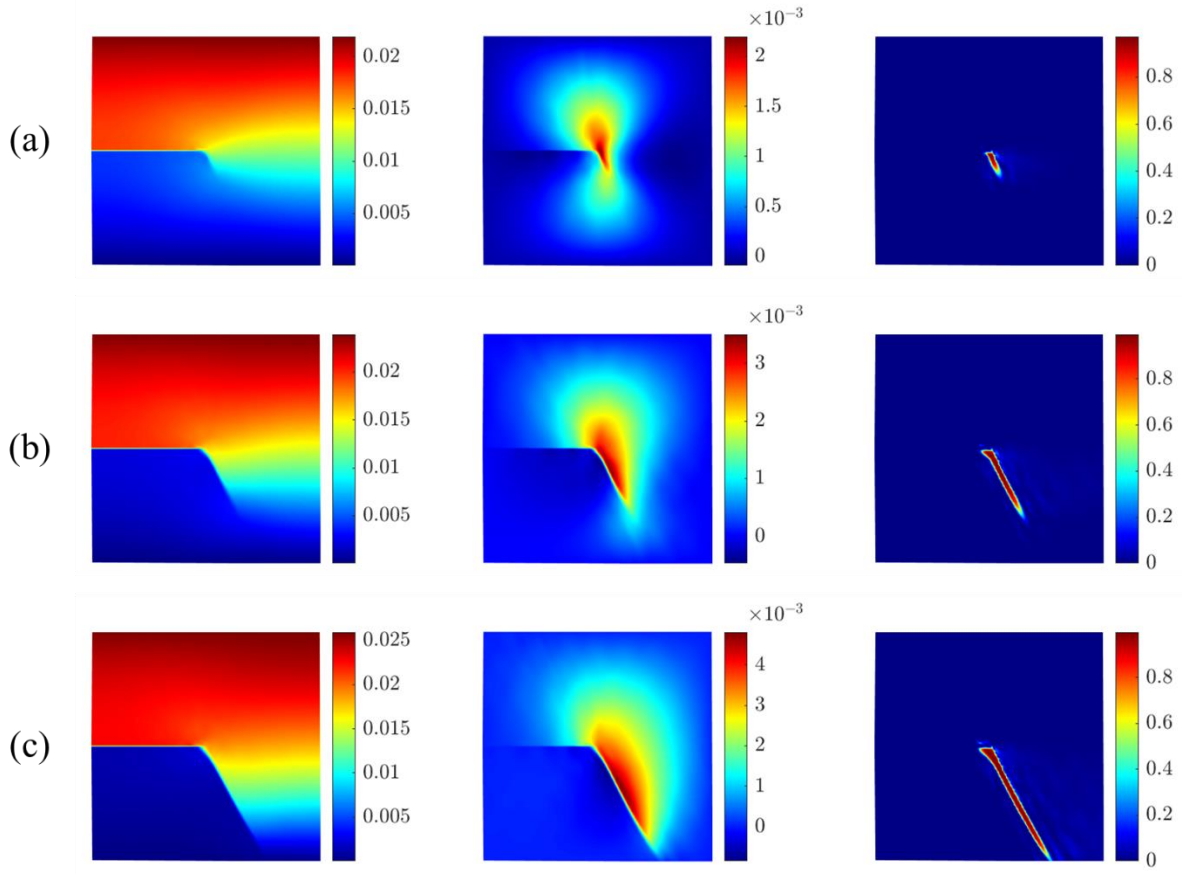

Figure 7.27. Damage evolution: (a) $g = 22 \times 10^{-3}$ mm, (b) $g = 24 \times 10^{-3}$ mm, (c) $g = 26 \times 10^{-3}$ mm; (left) u_1^h, (center) u_2^h, (right) damage

Acknowledgments

A portion of this chapter is currently being prepared for submission for publication in Baek, J., Chen, J. S., & Susuki, K. "Neural Network-enhanced Reproducing Kernel Particle Method for Modeling Localizations". The dissertation author was the primary investigator of this material.

A portion of this chapter is currently being prepared for submission for publication in Baek, J. & Chen, J. S "Neural Network-enhanced Reproducing Kernel Particle Method for Modeling Grain Refinement". The dissertation author was the primary investigator of this material.

Chapter 8

Applications to modeling of Grain Refinement

In this chapter, a series of numerical examples are presented to verify its capability to simulate sub-grain formations and grain boundary migrations which are key stages of rotational recrystallization. The plane-strain condition is assumed and the quadratic RK basis functions are used for the displacement, the lattice rotation, and the phase field, and kernel function with a normalized support size of 3.0 is used unless otherwise stated. For the domain integration, the 5×5 Gauss quadrature is employed.

8.1. Parameter sensitivity of the coupled Cosserat-phase field formulation

A single crystal under tension is simulated to investigate the sensitivity of the proposed formulation to the normalized stabilization parameter c introduced in Section 6.2. As shown in Figure 8.1, a single crystal contains two slip systems with angles 33.7° and 123.7° with respect to the horizontal axis. The domain is defined as $\Omega = (-H/2, +H/2) \times (-H/2, +H/2)$ with $H = 10$ μm. Fixed Dirichlet boundary conditions are imposed to u_1 and u_2 on the lower boundary and $g_2(t)$ is imposed to u_2 on the upper surface. All the other boundary conditions on $\mathbf{u}$, θ, and η are zero Neumann boundaries. The Lamé parameters of $\lambda = 69.2$ GPa, $\mu = 46.1$ GPa and the Cosserat parameters of $\alpha = f_0 \ell_\alpha$, $\beta = f_0 \ell_\beta^2$ with $f_0 = 1.8$ MPa, $\ell_\alpha = 3$ μm, and $\ell_\beta = 2$ μm are used. The phase field model constants $p = f_0$ and $q = f_0 \ell_\eta$ with $\ell_\eta = 0.5$ μm are also used together with the phase field model functions $r(\eta) = 0.5(1-\eta)^2$, $f(\eta) = \eta^2$ and $g(\eta) = 0.05 + 0.95\eta^2$, motivated by[90]. This set of model constants is taken from[93] and modified such that

the steady state diffuse grain boundary has its width approximately in the range of 0.7 to 1.0 μm. Additionally, the following velocity gradient is employed with $\dot{\gamma}^{(I)}$ defined in (3.34).

$$\dot{e}_{ij}^{p} = \sum_{I=1}^{2} \dot{\gamma}^{(I)} s_i^{(I)} n_j^{(I)}, \tag{8.1}$$

The constitutive model constants are $n = 10$, $K_v = 8.2$ MPa, $R = 0.3\mu b\sqrt{\rho_0}$ with $b = 0.2556$ nm and $\rho_0 = 10^{15}$ m^{-2} [68, 69]. The backward Euler scheme is employed to solve the constitutive equation. The phase field inverse mobility $\mu^{\eta} = 0.001 f_0 \tau_0$ with $\tau_0 = 10^{-5}$ s is used. The domain is discretized by 441 uniformly distributed RK nodes.

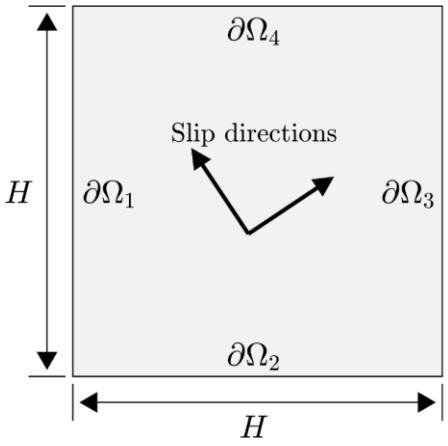

Dirichlet boundaries
- $\mathbf{u} = \mathbf{0}$ on $\partial\Omega_2$
- $u_2 = 2t\,(\mathrm{m})$ on $\partial\Omega_4$

Neumann boundaries
- $\sigma_{1j} n_j = 0$ on $\partial\Omega \setminus \partial\Omega_2$
- $\sigma_{2j} n_j = 0$ on $\partial\Omega \setminus (\partial\Omega_2 \cup \partial\Omega_4)$
- $m_j n_j = 0$ on $\partial\Omega$
- $\pi_j^{\nabla\eta} n_j = 0$ on $\partial\Omega$

Figure 8.1. Problem description.

Figure 8.2 shows the progressive deformation obtained by the proposed method with $\log_{10} c = -4$. Due to the presence of slip systems, the anisotropic deformation is developed as the initially single crystal is deformed. Under such anisotropy, lattice curvature is localized, i.e., GNDs locally evolve, to accommodate the anisotropic deformation. As a result, four distinct dislocation block structures are developed during the deformation process. The phase field effectively captures

the localized lattice curvature. As larger deformation is developed, the crystalline lattice of each sub-grain independently rotates and the misorientation becomes larger at the sub-grain boundaries with a maximum value of 8° at approximately time $t = 0.6\,\mu s$. As shown in Figure 8.3, the solutions obtained from different values of c within the suggested parameter range agree with each other, which demonstrates that the proposed formulation is insensitive to the stabilization parameter.

Additionally, the solution obtained with the strong imposition of rotational kinematic constraint on boundaries discussed in Section 0 is compared with the solutions obtained with the least squares stabilization presented in 6.3.2 with various stability parameters. As discussed in Section 6.3.2, the lower bound of the normalized stability parameter has not been fully discovered and a choice of a small stability parameter may not eliminate the spurious lattice rotation modes. As shown in Figure 8.4(a), the lattice orientation field obtained with $\log c = -8$ has a spurious lattice rotation compared to the choices of larger stability parameters (Figure 8.4(b) and (c)). In contrast, the strong imposition of the rotational kinematic constraint on boundaries without the least squares stabilization introduced yields the lattice orientation fields without a spurious rotation, which demonstrates that the strong imposition can be an alternative approach to eliminate the spurious lattice rotation modes introduced in the duality-based formulation.

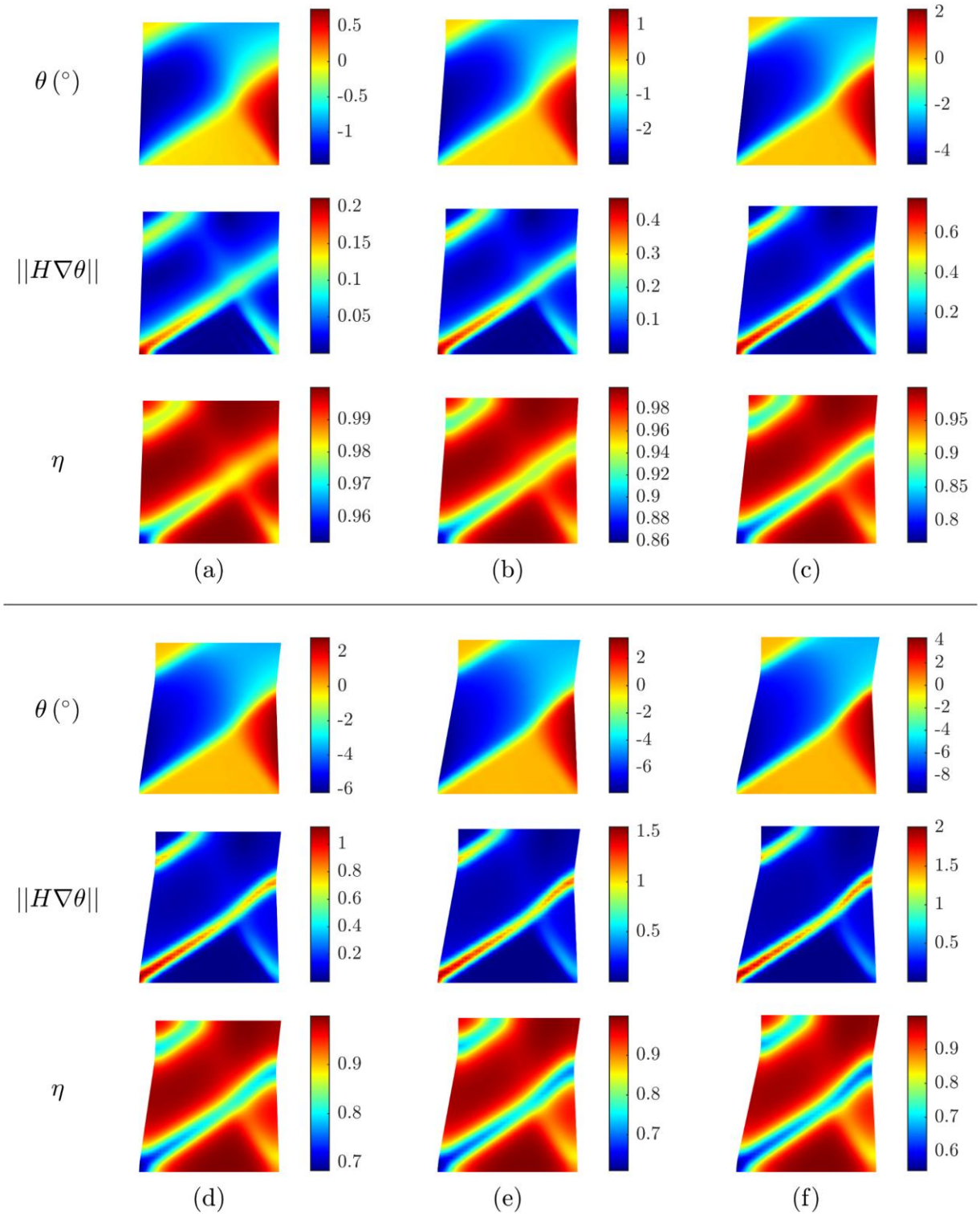

Figure 8.2. Progressive deformation obtained by the proposed method with $\log_{10} c = -4$ at times of (a) 0.1, (b) 0.2, (c) 0.3, (d) 0.4, (e) 0.5, and (f) 0.6 μs

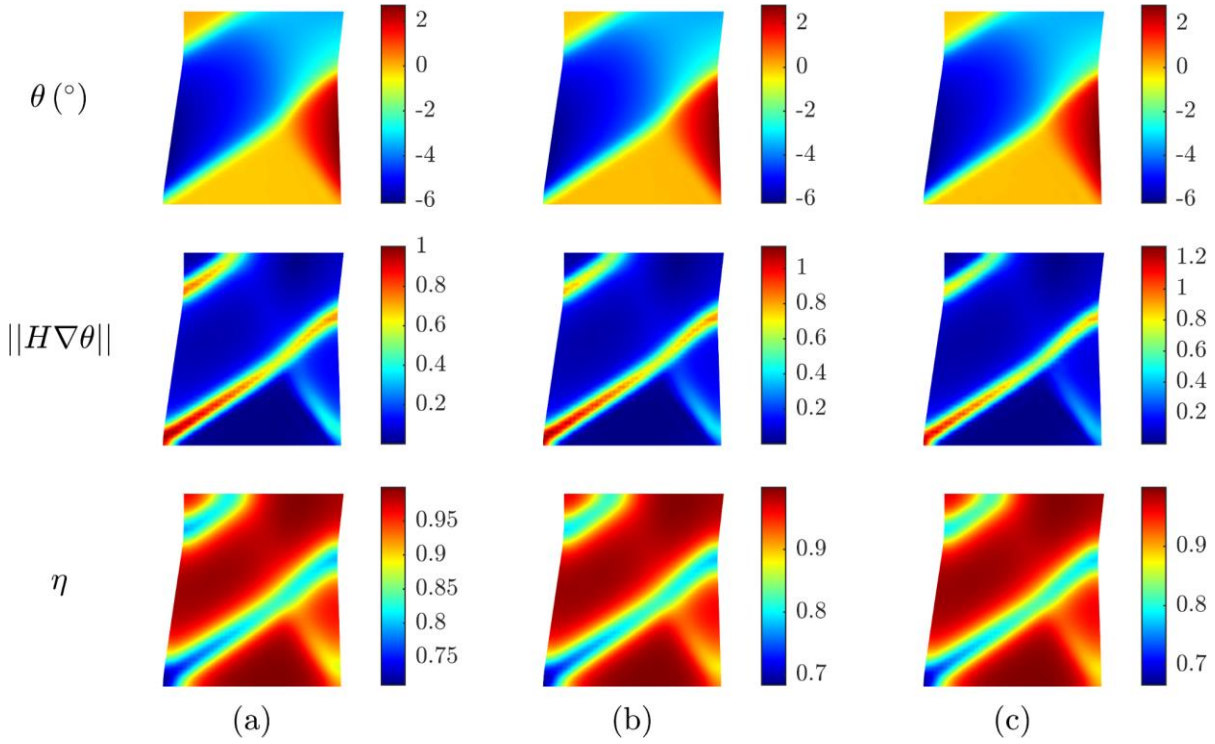

Figure 8.3. Solutions obtained at $t = 0.4$ μs with different c: (a) $\log_{10} c = -6$, (b) $\log_{10} c = -4$, and (c) $\log_{10} c = -2$

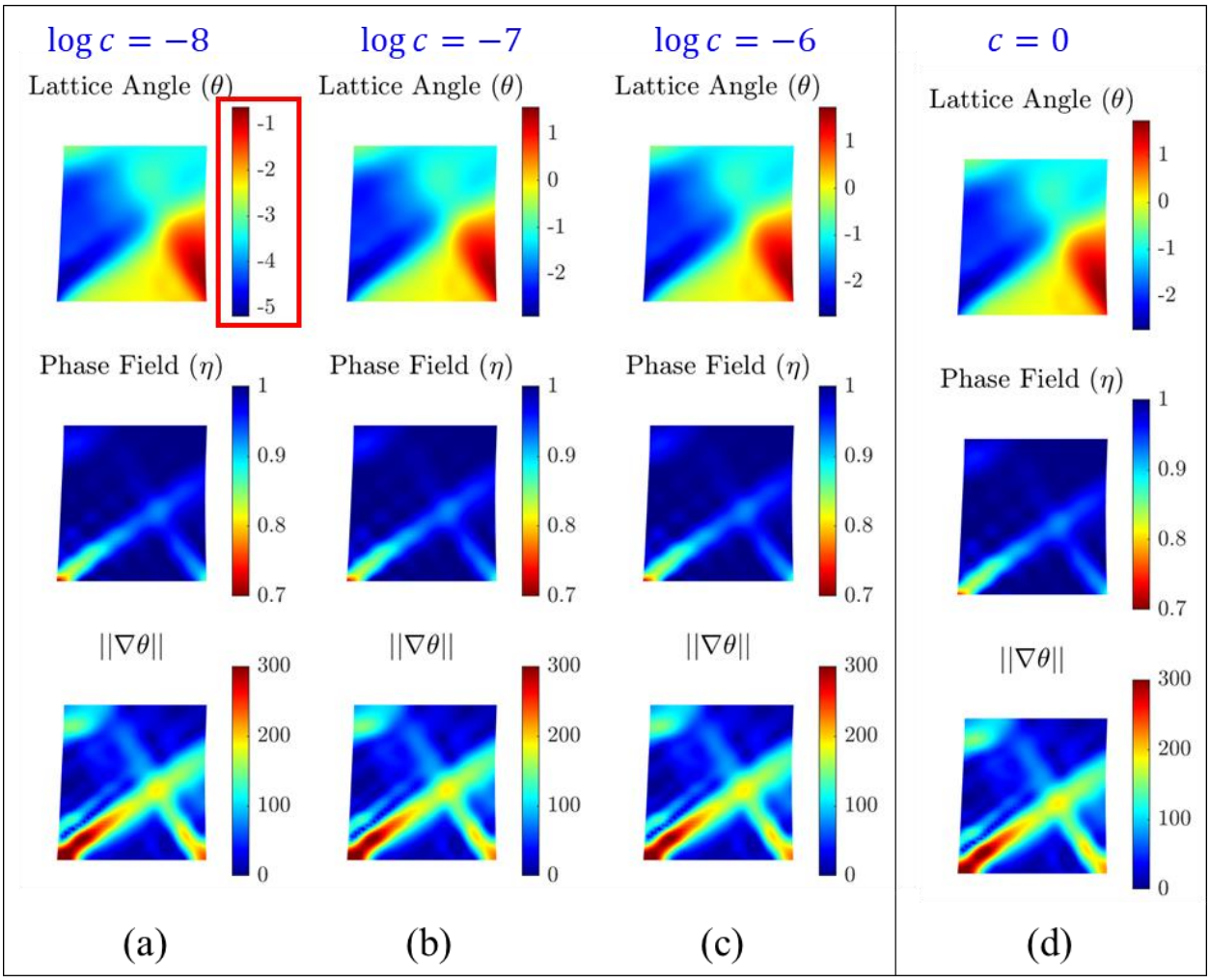

Figure 8.4. Comparison of the numerical solutions: least squares stabilization with (a) $\log c = -8$, (b) $\log c = -7$, and (c) $\log c = -6$, and (d) the strong imposition of the rotational kinematic constraints on boundaries with $c = 0$

8.2. Migration of grain boundaries with a triple junction

A problem involving migrations of grain boundaries with a triple junction is considered. In this problem, the grain boundary topology is evolved towards steady state by grain boundary migrations. This is an essential stage in the rotational recrystallization mechanism where the dislocation blocks formed under large anisotropic deformation is made into equiaxed grains.

Consider a square domain $\Omega = (0,0) \times (D, H)$ with dimensions D = 12 μm and H = 10 μm as shown in Figure 8.5(a). The domain is initially composed of three rectangular grains with the initial constant lattice orientation $\theta(t = 0)$ within each grain. The initial values are shown in Figure 8.5(a) along with the initial displacement $\mathbf{u}(t = 0) = \mathbf{0}$. The Dirichlet boundary conditions on $\mathbf{u}$ and θ are applied on all boundaries: $\mathbf{u} = \mathbf{0}$ and $\theta = \theta(t = 0)$ on Γ.

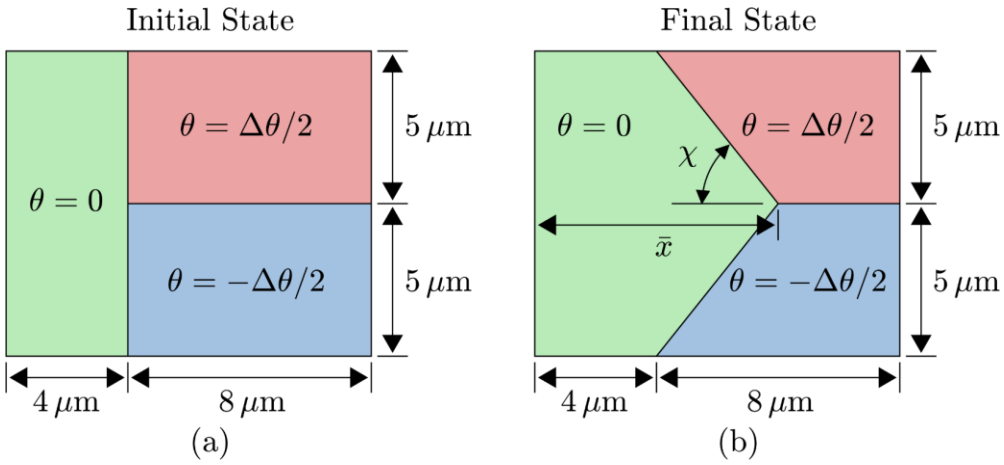

Figure 8.5. Problem dimension and initial grain orientation

The following constitutive equation is used.

$$\dot{e}_{ij}^{p} = \mu_{*}^{-1}\sigma_{ij}^{a}, \tag{8.2}$$

where the inverse grain boundary mobility is taken as [93]

$$\mu_{*} = \hat{\mu}_{*}\big(1 - \big(1 - \mu_{p}\big)\exp(-\beta_{P}|\nabla\theta|)\big), \tag{8.3}$$

with $\mu_p = 1000$, $\beta_P = 1000$, and $\hat{\mu}_* = 0.1 f_0 \tau_0$ with $\tau_0 = 10^{-5}$ s. The phase field inverse mobility $\mu^\eta = 0.001 f_0 \tau_0$ is also used. The phase field model functions and constants used for this numerical example are listed in Set III of Table 3.1 in Section 3.3.

For the numerical implementation, the following initial lattice orientation field is applied:

$$\theta(t=0) = \frac{\Delta\theta}{4}\left(1 + \tanh\left(\frac{x_1 - \xi_1}{w_1}\right)\right)\tanh\left(\frac{x_2 - \xi_2}{w_2}\right), \tag{8.4}$$

where ξ_1, ξ_2, w_1, and w_2 are 4 μm, 5 μm, 1.5 μm, and 1.2 μm, respectively, and $\Delta\theta$ is the difference in the initial lattice orientations of the upper-right and lower-right grains as shown in figure Figure 8.5(a). To hold $\mathbf{u}(t=0) = \mathbf{0}$ and nonzero elastic rotation such that $\varphi^e(t=0) = \theta(t=0)$ simultaneously, the initial plastic rotation $\varphi^p(t=0) = -\theta(t=0)$ is applied. With $\varphi(t=0) = 0$ derived from $\mathbf{u}(t=0) = \mathbf{0}$, $\varphi^e(t=0) = \varphi(t=0) - \varphi^p(t=0) = \theta(t=0)$ holds.

The analytical value of χ in Figure 8.5(b) can be obtained by the Herring's equation [109]:

$$\chi = 180° - \cos^{-1}\left(-\frac{1}{2}\frac{E^{GB,horiz}}{E^{GB,diag}}\right), \tag{8.5}$$

where $E^{GB,horiz}$ and $E^{GB,diag}$ are the GB energies of the horizontal grain boundary and the diagonal grain boundaries, respectively. At the steady state, each grain keeps its initial lattice orientation [93] as shown in Figure 8.5(b) and the displacement $\mathbf{u} = \mathbf{0}$.

For numerical simulations, the domain is uniformly discretized by 806 RK particles with a cubic RK basis function for $\mathbf{u}^h$, θ^h, and η^h with a normalized support size of 4.0 for accurate

estimation of $\nabla \cdot \mathbf{m}$ which acts as a driving force of the grain boundaries. Figure 8.6 presents the progression of θ^h, $|\nabla\theta^h|$, and η^h for $\Delta\theta = 15°$. The triple junction moves as the grain boundary migrates while the lattice orientation of each grain does not change from its original value. Two additional problems with $\Delta\theta = 12°$ and $\Delta\theta = 24°$ are considered for comparison and the predicted steady state solutions for all three cases are presented in Figure 8.7. A smaller χ is obtained with larger $\Delta\theta$. This is because the Read – Shockley type relation, the nonlinear relation of GB energy and $\Delta\theta$, shown in Figure 3.8(a), leads to smaller $E^{GB,horiz}$-to-$E^{GB,diag}$ ratio with larger $\Delta\theta$, and consequently the grain boundary topology is in equilibrium with larger χ as Herring established[109] and reflected in Eq. (8.4). Figure 8.8 shows numerical and analytical χ and $\bar{x}$ against $\Delta\theta$ and the numerical results agree with the analytical solutions with errors less than 4%.

The effectiveness of the proposed phase field approach is shown in Figure 8.9. As shown in Figure 8.9(d)-(f), the simulation without the phase field does not maintain the sharp transition of the lattice orientation, therefore cannot capture the grain boundary structure.

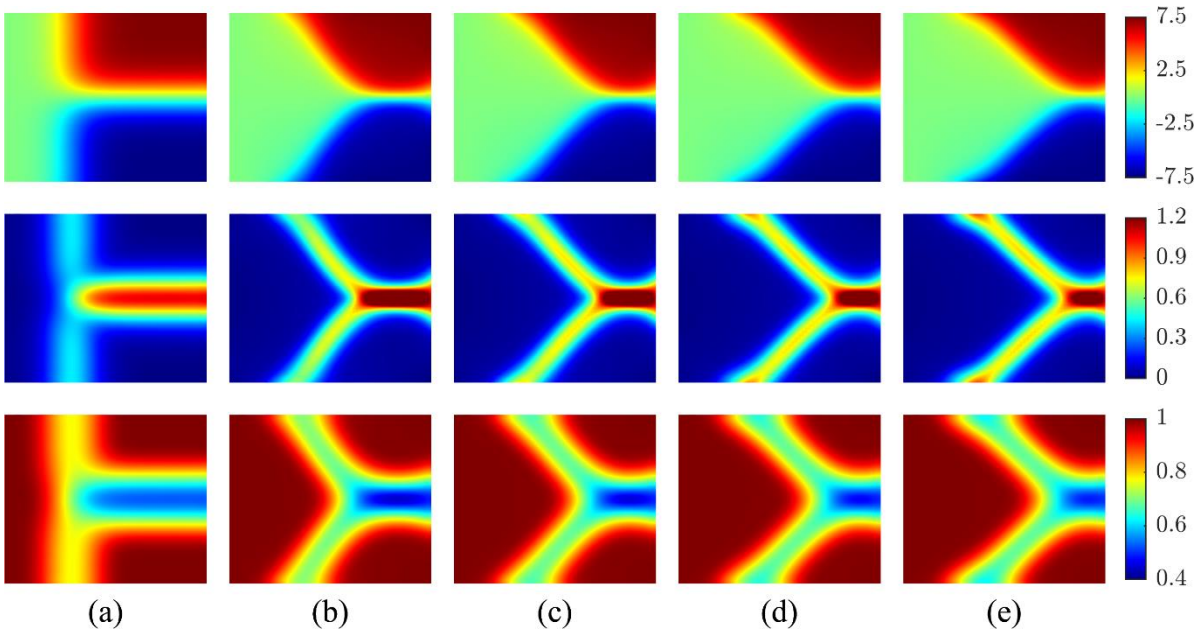

Figure 8.6. Numerical results of progressive grain migration at times of (a) 0, (b) 1.0, (c) 2.0, (d) 3.0, and (e) 4.0 μs: θ (top), $|H\nabla\theta|$ (middle), and η (bottom).

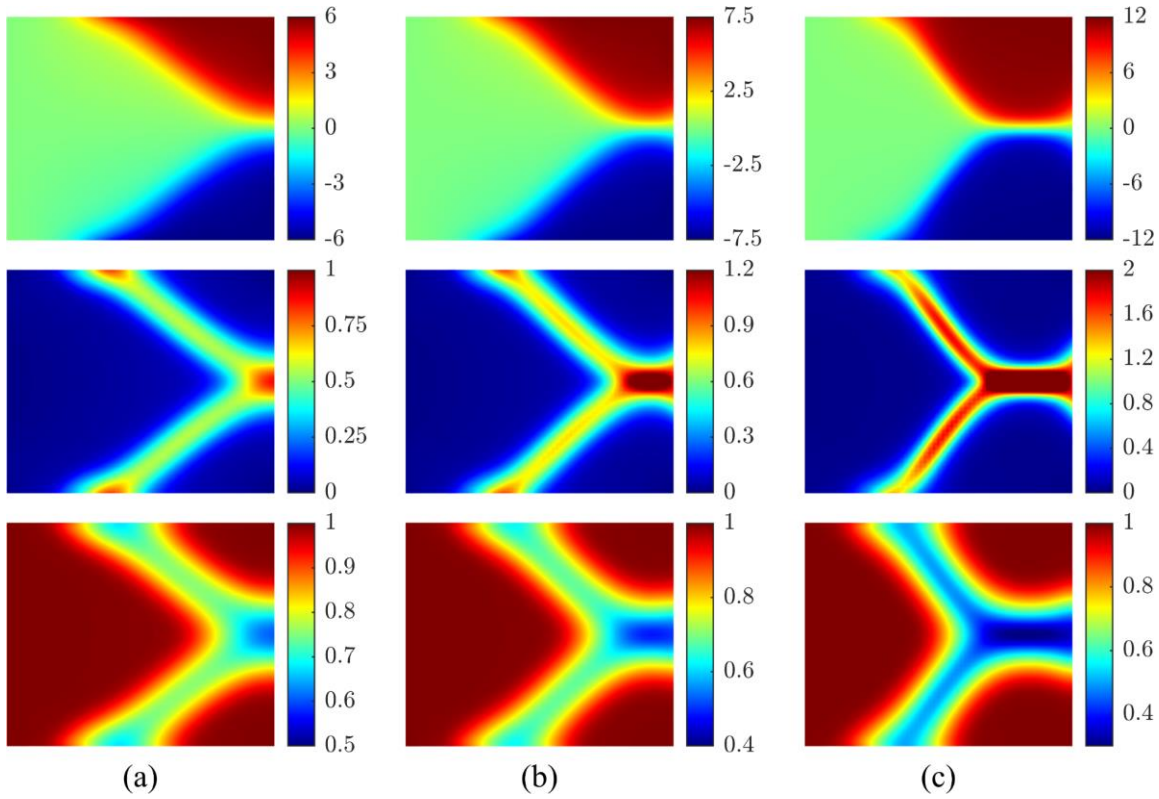

Figure 8.7. Predicted steady states of (a) $\Delta\theta = 12°$, (b) $\Delta\theta = 15°$, and (c) $\Delta\theta = 24°$: θ (top), $|H\nabla\theta|$ (middle), and η (bottom).

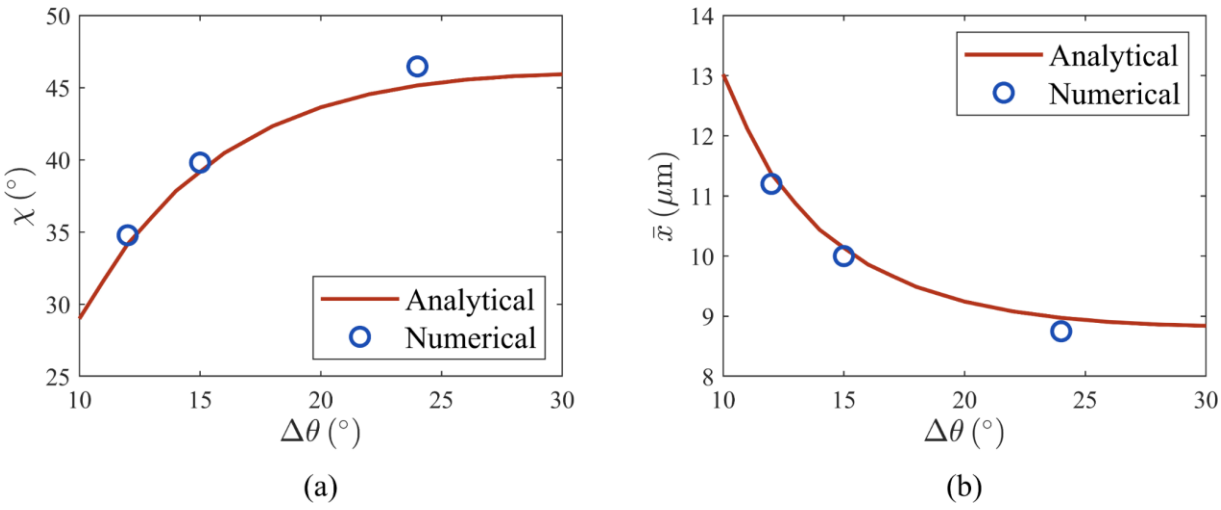

Figure 8.8. Comparison of numerical and analytical solutions: (a) χ vs $\Delta\theta$ and (b) $\bar{x}$ vs $\Delta\theta$

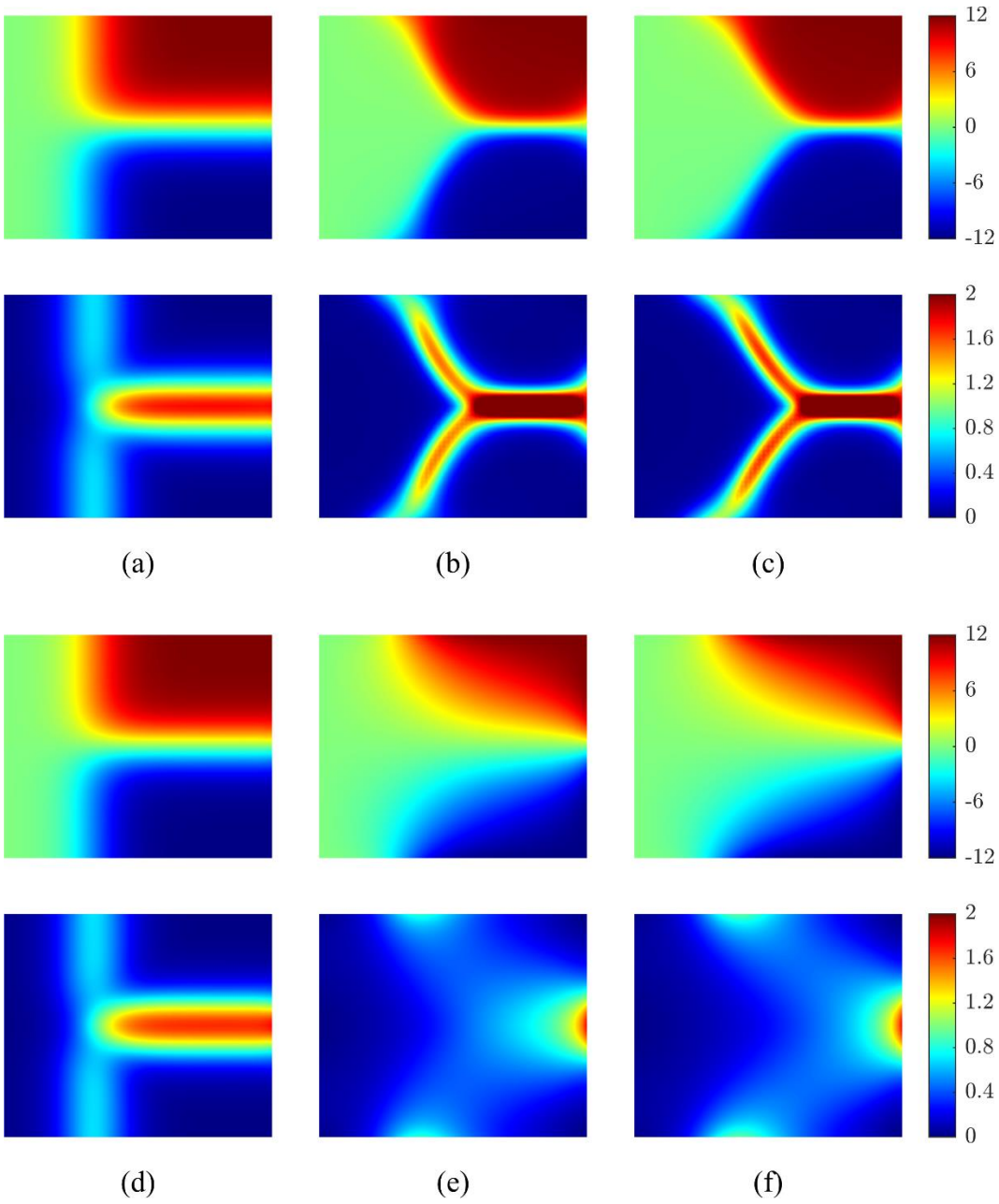

Figure 8.9. Comparison of simulations with and without the phase field for the case of $\Delta\theta = 24°$. θ and $|H\nabla\theta|$ are shown on top and bottom of each subfigure, respectively. Results of the simulation with phase field are given at times of (a) 0, (b) 0.25, (c) 0.5 μs. Results of the simulation without phase field are given at times of (d) 0, (e) 0.25, (f) 0.5 μs.

Next, we solve the same problem using NN-RKPM proposed in Chapter 7. For simplicity, in solving the problem, the displacement field is ignored to focus on investigating the capability

of NN-RK in capturing the sharp solution transition. For the RK approximation, the domain is discretized with the nodal spacing of 0.5 μm compared to 0.4 μm which is used for the pure RKPM case presented in this case. The linear RK basis is additionally used along with the cubic B-spline kernel with normalized support size of 2.0. For the NN approximation, we consider two models M1 and M2 of which the details are listed in Table 8.1. Note that more NN kernels are used for M2 than for M1, which leads to more unknowns. For both models, the weights and biases associated with the parametrization network are shared by the lattice orientation and phase field NN approximations. However, the other unknown parameters are independently calculated for both approximations. The sizes of the Gauss quadrature cells are 0.125 μm and 0.083μm for M1 and M2, respectively, and 2×2 Gauss points are used per cell. Additionally, $1-\eta$ is approximated only by the NN approximation as it has nonzero value only at the narrow band of the grain boundary, and θ is approximated by the combination of RK and NN approximations.

Table 8.1. NN approximation details for the triple junction problem

		Parametrization network					
Model	# Blocks	# Layers	# Neurons per layer	# NN kernels per layer	Order of basis	Total number of unknowns	# Gauss points
M1	4	1	22	9	1	920	25600
M2	4	1	22	16	1	1152	47488

The steady state solutions for the case of $\Delta\theta$=24° is plotted in Figure 8.10. The NN-RKPM models M1 (Figure 8.10(b)) and M2 (Figure 8.10(c)) present far sharper solution transitions at the grain boundaries and significantly thinner diffuse grain boundary widths than the pure RKPM solution. The high-gradient representation of the diffuse grain boundary is encouraging in that it

enables the model to more accurately captures complicated grain boundary morphology. Figure 8.11 shows how NN and RK approximations influences the orientation field. While the RK approximation captures the overall smooth solution transition, the NN approximation enriches the solution field so that the sharp orientation transition at the grain boundaries is accurately captured.

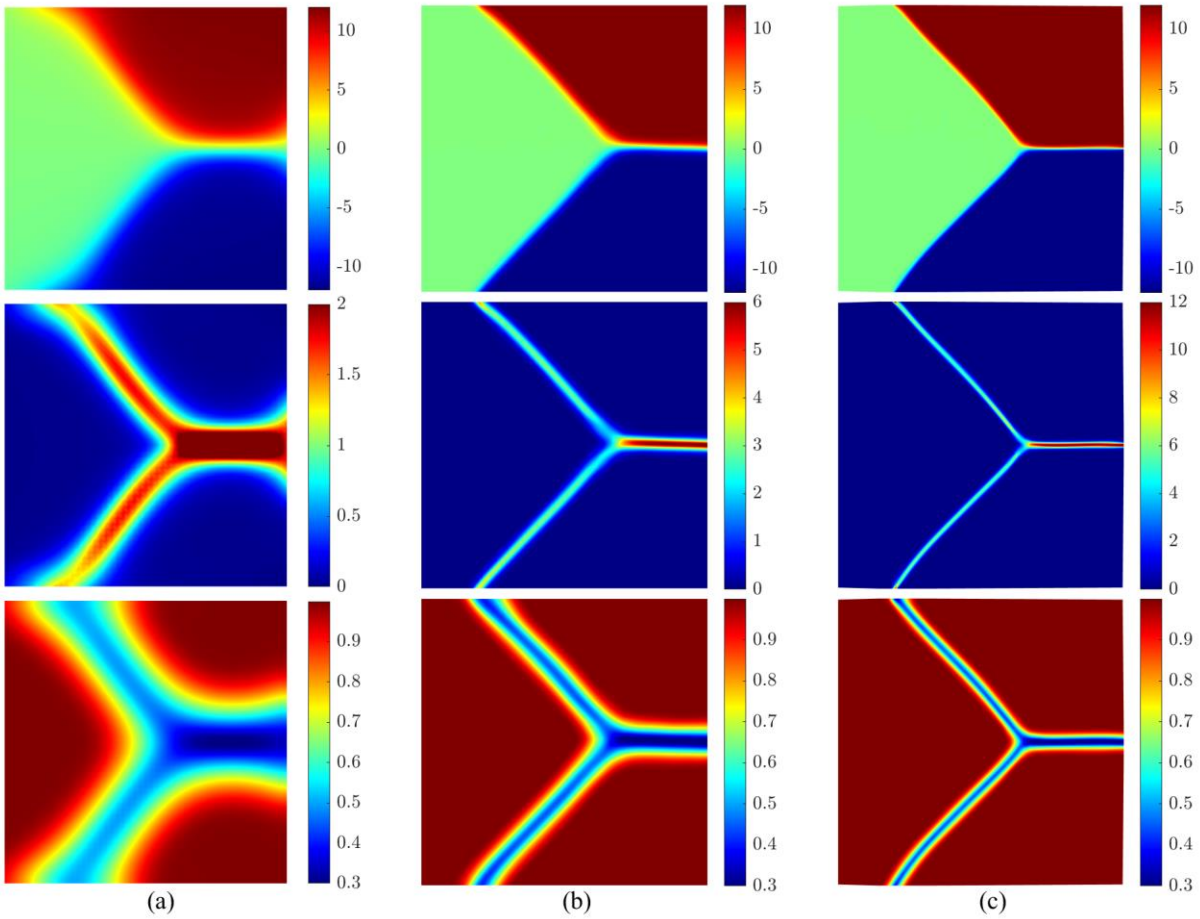

Figure 8.10. Steady state solutions predicted by various models: (a) pure RKPM, (b) NN-RKPM M1, (c) NN-RKPM M2. θ (top), $|H\nabla\theta|$ (middle), and η (bottom).

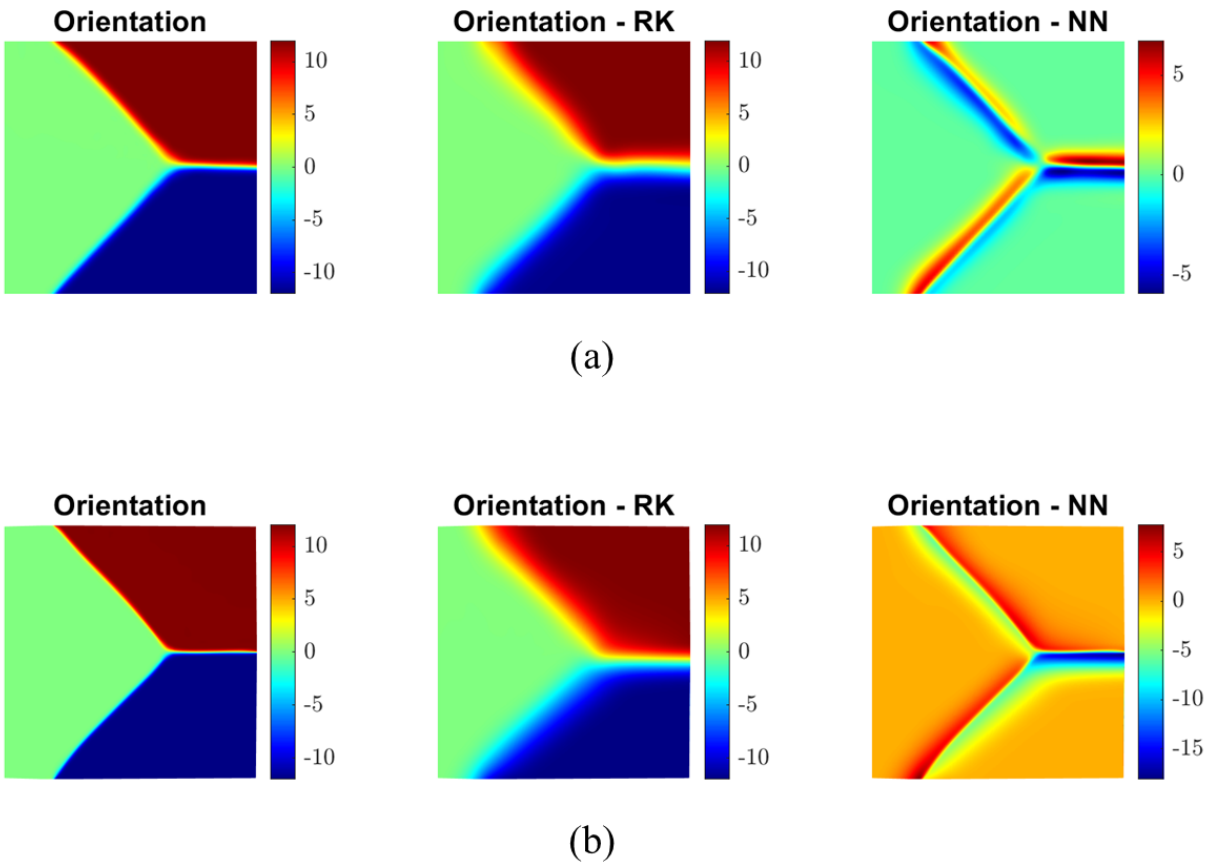

Figure 8.11. RK and NN approximations from M1 and M2

8.3. Band substructure formation in an FCC single crystal

A two-dimensional plane strain problem of uniaxial hot compression of an FCC single crystal aluminum is considered. The rotational recrystallization-induced grain refinement is facilitated when temperature $T \geq 0.4T_m$ where T_m is the melting point[25]. In this numerical example, $T = 0.7T_m$ is used as considered in Gourdet and Montheillet[33] for uniaxial hot compression experiments of single crystal aluminums. Also, it has been reported that the

nonstandard {110}<110> [1] slip systems dominate instead of the standard close-packed {111}<110> systems in the temperature range $T \geq 0.6T_m$[110]. Figure 8.12(a) describes the considered single crystal cube in the global coordinate. The crystallographic directions [100], [010], and [001] in Miller indices align with x_1, x_2, and x_3 directions, respectively. The compression axis is x_2. The slip system with $\mathbf{n} = \left(-1/\sqrt{2}, 1/\sqrt{2}, 0\right)$ and $\mathbf{s} = \left(1/\sqrt{2}, 1/\sqrt{2}, 0\right)$ is the activated system and the problem is reduced to the plane strain problem on $x_1 - x_2$ plane with $L = 1$ mm described in Figure 8.12(b). A set of periodic boundary conditions is introduced due to the fact that the problem domain is significantly smaller than the actual experiment specimen ($18 \times 12 \times 11.5$ mm^3)[33]. The compression of specimen is applied with the following Dirichlet boundary conditions: on the bottom edge,

$$\frac{1}{L}\int_{\Gamma^B} u_2 \, d\Gamma = 0, \tag{8.6}$$

and on the top edge,

$$\frac{1}{L}\int_{\Gamma^T} u_2 \, d\Gamma = -\dot{\epsilon}t, \tag{8.7}$$

[1] Herein, the Miller indices are used to describe planes and directions[112]. $[hkl]$ denotes a direction $h\mathbf{a}_1 + k\mathbf{a}_2 + l\mathbf{a}_3$ where $\mathbf{a}_i$'s are lattice basis vectors. (hkl) denotes a plane perpendicular to a direction $h\mathbf{b}_1 + k\mathbf{b}_2 + l\mathbf{b}_3$ where $\mathbf{b}_i$'s are the reciprocal lattice vectors of $\mathbf{a}_i$'s. For cubic crystals, the set of $\mathbf{a}_i$'s and the set of $\mathbf{b}_i$'s are identical. <hkl> and {hkl} refer to the set of directions of the same type and the set of planes of the same type due to the symmetry of the crystalline structures, respectively.

where Γ^b and Γ^T denote the bottom and top boundaries and the loading rate $\dot{\bar{\epsilon}} = 0.1L\ \mathrm{s}^{-1}$ is used. A penalty method is used to apply the boundary conditions with the penalty constant of 100μ.

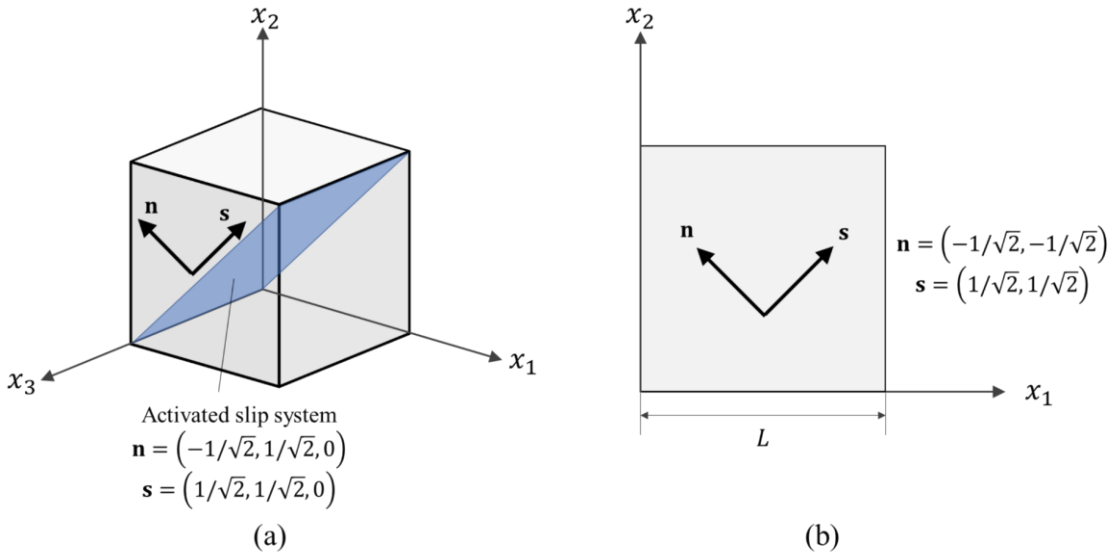

Figure 8.12. Three dimensional and plane strain description of the considered FCC single crystal

The constitutive equation (3.34) is implemented with $K_v = 0.15r$ MPa, $r = 0.73$, and $n = 3.6$. The model constants are calibrated such that the relation between the plastic slip and the resolved shear stress matches the constitutive behavior provided in Abrivard et al.[90]. The critical resolved shear stress is given as $R = 0.3r\mu b\sqrt{\rho_{SSD}}$ with $b = 0.286$ nm. The statistically stored dislocation (SSD) density ρ_{SSD} is randomly distributed with the normal distribution $\mathcal{N}(2 \times 10^{11}\ \mathrm{m}^{-2}, 0.5 \times 10^{11}\ \mathrm{m}^{-2})$ to initiate inhomogeneous deformation. The shear modulus of 20.6 GPa at $T = 0.7T_m$ [33] and Poisson's ratio of 0.35 are used. The Cosserat and phase field parameters $f_0 = 30$ MPa, $\ell_\beta = 0.1$ mm, $g_0 = 10^{-6}f_0$ and $\ell_\eta = 0.0875$ mm are chosen such that the phase field has a sufficiently large value at low angle grain boundaries and it maintains the

diffuse grain boundary width of approximately $0.1L$. For numerical simulations, the domain is uniformly discretized by 441 RK particles.

The numerical results are shown in Figure 8.13. The figures clearly show banded sub-grain structure and the orientation of the bands is approximately 135° with respect to the horizontal axis which is perpendicular to the slip direction **s**. This implies that the localized lattice curvature (i.e. lattice reorientation) is formed by kink bands. Here kink band denotes a localized plastic deformation zone with an orientation perpendicular the slip direction[53] and the formation of kink bands is an important source of sub-grain formation[72]. The non-symmetric activation of slip system leads to inhomogeneous displacement and deformation as shown in Figure 8.13. The experimental observations are shown in Figure 8.14. The crystallographic orientation of the initial single crystal (Figure 8.14(a)) is consistent with Figure 8.12(a)[33]. Figure 8.14(b) and (c) are snapshots on the surfaces (001) and (100), respectively[111], that contain the slip traces, which implies the slip system depicted in Figure 8.12(a) was activated. Also, there is banded microstructure shown on surface (001) (Figure 8.14(a)) perpendicular to the slip direction, which qualitatively validates the numerical results. Although in-depth quantitative comparisons are not available due to the limited information about the material properties used in the experiment, the numerical simulation successfully captures the microstructural evolution including the formation of kink bands and the banded sub-grains.

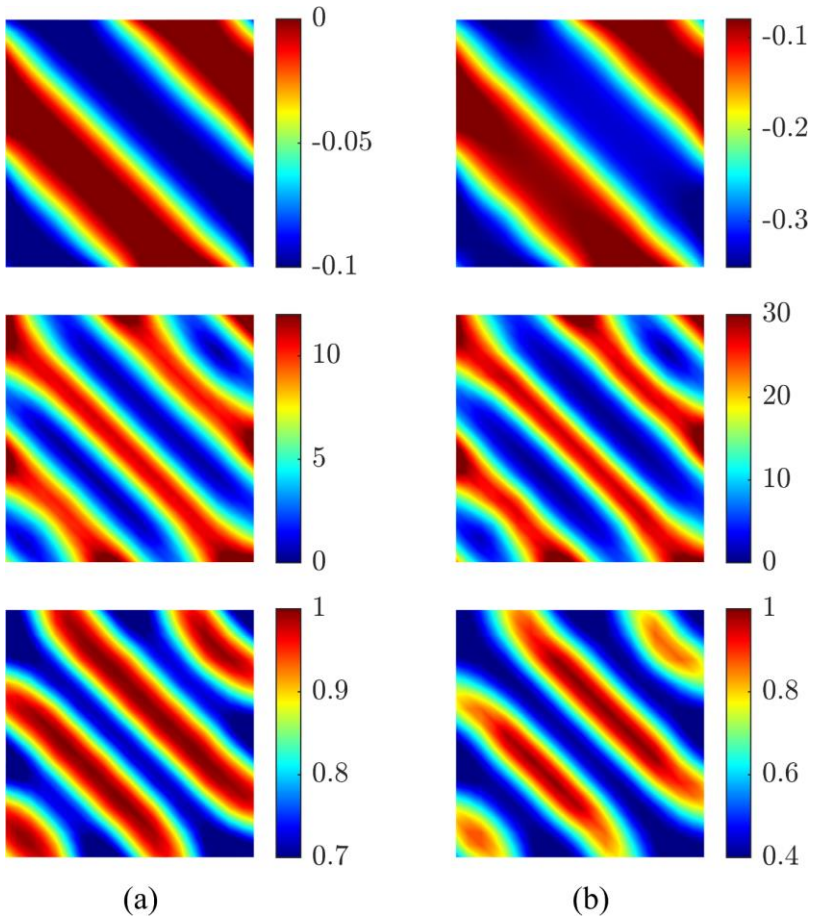

Figure 8.13. Numerical results: from top to bottom, θ^h, $|\nabla\theta^h|$, and η^h at times of (a) 0.26 ms and (b) 1 ms

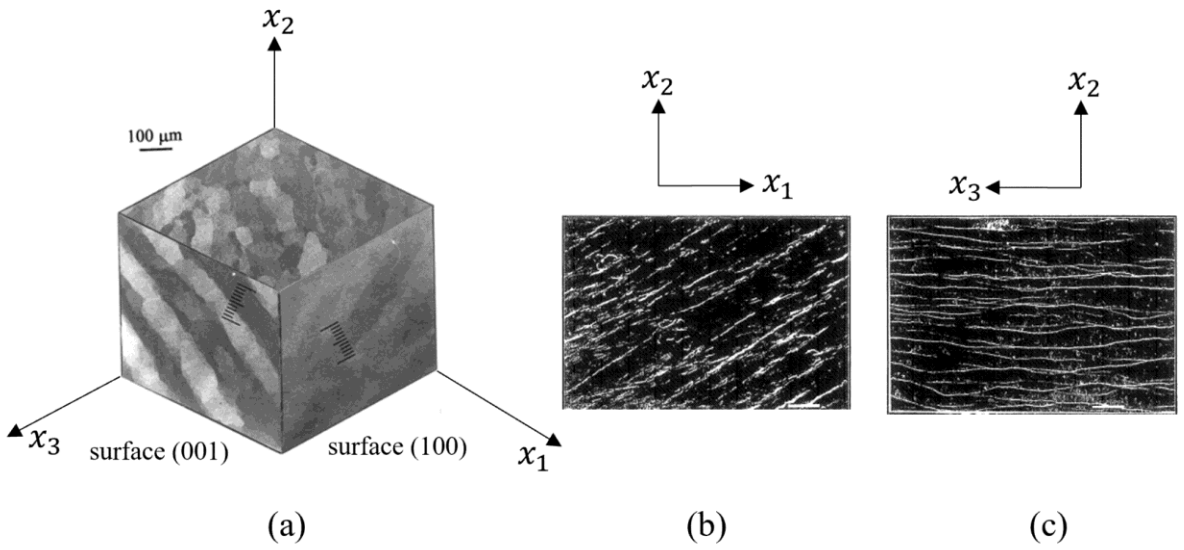

Figure 8.14. Experimental observation[33, 111]: (a) a cube cut out from the central part of the specimen, (b) slip traces on surface (001), and (c) slip traces on surface (100)

Acknowledgments

A portion of this chapter has been accepted for publication in Baek, J., Chen, J. S., Tupek, M., Beckwith, F., & Fang, H. E. "A Duality-based Coupling of Cosserat Crystal Plasticity and Phase Field Theories for Modeling Grain Refinement", International Journal for Numerical Methods in Engineering. The dissertation author was the primary investigator of this material.

A portion of this chapter is currently being prepared for submission for publication in Baek, J. & Chen, J. S. "Neural Network-enhanced Reproducing Kernel Particle Method for Modeling Grain Refinement". The dissertation author was the primary investigator of this material.

Chapter 9

Conclusions

9.1. Summary of this research

A duality-based Cosserat crystal plasticity formulation coupled with a phase field was proposed for modeling deformation-induced grain refinement. The independent lattice orientation field was introduced based on duality theory as a stability and accuracy enhancement of the classical penalty-based approach. In the proposed method, the kinematic constraints on the displacement-based and lattice orientation-based lattice curvatures were imposed with the energy conjugate couple stress derived in the dualization. To avoid spurious lattice rotation, least squares stabilization was introduced. A stability analysis was performed to derive the suitable range for the stabilization parameter to maintain the coercivity of the duality-based formulation. A projection-based stabilization was additionally employed for the duality-based formulation based on the weak inf-sup condition. The high order continuity requirement of the solution space was attained by the reproducing kernel approximation. The numerical results demonstrated that the equal order approximations for displacement, rotation, and phase field are stable, which allows efficient use of the same set of shape functions for all independent variables.

The proposed method yielded optimal convergence rates and superior solution accuracy over the penalty-based method. Also, the solution sensitivity to the stabilization parameter was shown to be much smaller than the sensitivity of the penalty method to the penalty parameter. The projection-based stabilization effectively suppressed oscillations in solution including the lattice curvature and couple stress divergence. The proposed method was successfully applied to

modeling key mechanisms of rotational recrystallization: evolution of block dislocation structures and rotation of grain boundaries. In the former example, the proposed method captured the lattice curvature localization induced by the anisotropic deformation due to the formation of kink bands, and the resulting banded sub-grains are formed perpendicular to the slip direction, which qualitatively agree with the experimental observation. In the latter example, the proposed method predicted the migration of grain boundaries with a triple junction, and the predicted steady state angle between grain boundaries agreed well with the analytical value.

In the conventional crystal plasticity formulation coupled with phase field, modeling the sharp transition in the phase field near the grain boundaries associated with the lattice orientation often requires highly refined discretization for sufficient accuracy, which significantly increases the computational cost. To this end, neural network-enhanced reproducing kernel particle method (NN-RKPM) has been proposed, where the location and orientation of strain localizations were automatically captured by the NN algorithms, and the distribution of solution transition was constructed with the NN approximations via the minimization of total potential energy. The standard RK approximation is then utilized to approximate the smooth part of the solution to permit a much coarser discretization than the high-resolution discretization needed to capture sharp solution transition with the conventional methods. The proposed NN-RKPM was first verified by solving several damage evolution problems. The proposed computational framework was then applied to modeling grain refinement mechanisms, including the migration of grain boundaries at a triple junction and sub-grain formation of a material with activated slip systems, for validating the effectiveness of the proposed methods.

9.2. Recommendations for Future Work

The recommendations for future work are summarized as follows.

- Development of advanced nodal integration technique suitable for the duality-based Cosserat crystal plasticity – phase field formulation for additional computational efficiency. When high dimensional problems are of interest, employment of an efficient integration technique is essential. Since the proposed mixed formulation involves second derivative of the lattice orientation, a reduced integration such as a nodal integration scheme should be carefully designed to satisfy the variational consistency for optimal convergence.
- Extension of the proposed formulation to the large deformation framework. High-rate manufacturing processes produce extreme deformation that entails severe shear localizations where intense grain refinement occurs. To this end, the geometric nonlinearity should be considered.
- Dynamic formulation and development of shock algorithm for Cosserat – phase field theory. High-rate manufacturing processes often involve high velocity impact and this entails strong dynamic effects. Particularly, strong shock is often produced and numerical investigation into the effects of the shock on the microstructural evolution, such as grain refinement and phase change, would be beneficial. Also, numerical investigation into the effects of the generation and annihilation of dislocations under the adiabatic condition on the grain refinement would also be beneficial.
- Development of multiscale formulation. As the scale of the actual manufacturing product and the grain scale is several orders in difference, a robust multiscale method can be

developed to establish the linkage between the processing parameters and the microstructural evolution.

Acknowledgments

A portion of this chapter has been accepted for publication in Baek, J., Chen, J. S., Tupek, M., Beckwith, F., & Fang, H. E. "A Duality-based Coupling of Cosserat Crystal Plasticity and Phase Field Theories for Modeling Grain Refinement", International Journal for Numerical Methods in Engineering. The dissertation author was the primary investigator of this material.

A portion of this chapter is currently being prepared for submission for publication in Baek, J., Chen, J. S., & Susuki, K. "Neural Network-enhanced Reproducing Kernel Particle Method for Modeling Localizations". The dissertation author was the primary investigator of this material.

A portion of this chapter is currently being prepared for submission for publication in Baek, J., & Chen, J. S. "Neural Network-enhanced Reproducing Kernel Particle Method for Modeling Grain Refinement". The dissertation author was the primary investigator of this material.

BIBLIOGRAPHY

1. Carpenter SH, Wittman RH (1975) Explosion Welding. Annu Rev Mater Sci 5:177–199. https://doi.org/10.1146/annurev.ms.05.080175.001141

2. Cowan GR, Holtzman AH (1963) Flow configurations in colliding plates: Explosive bonding. J Appl Phys 34:928–939. https://doi.org/10.1063/1.1729565

3. Cowan GR, Bergmann OR, Holtzman AH (1971) Mechanism of bond zone wave formation in explosion-clad metals. Metall Mater Trans B 2:3145–3155. https://doi.org/10.1007/BF02814967

4. Bahrani AS, Crossland B (1964) Explosive welding and cladding: an introductory survey and preliminary results. Proc Inst Mech Eng 179:264–305. https://doi.org/10.1243/PIME_PROC_1964_179_023_02

5. Bahrani AS, Black TJ, Crossland B (1967) The Mechanics of Wave Formation in Explosive Welding. Proc R Soc A Math Phys Eng Sci 296:123–136. https://doi.org/10.1098/rspa.1967.0010

6. Manikandan P, Hokamoto K, Deribas AA, et al (2006) Explosive Welding of Titanium/Stainless Steel by Controlling Energetic Conditions. Mater Trans 47:2049–2055. https://doi.org/10.2320/matertrans.47.2049

7. Vivek A, Liu BC, Hansen SR, Daehn GS (2014) Accessing collision welding process window for titanium/copper welds with vaporizing foil actuators and grooved targets. J Mater Process Technol 214:1583–1589. https://doi.org/10.1016/j.jmatprotec.2014.03.007

8. Arnett K (2019) Explosive Welding of Aluminum Plates: Experiments, Evaluation, and Modeling. University of California, San Diego

9. Grignon F, Benson D, Vecchio KS, Meyers MA (2004) Explosive welding of aluminum to aluminum: Analysis, computations and experiments. Int J Impact Eng 30:1333–1351.

https://doi.org/10.1016/j.ijimpeng.2003.09.049

10. Nassiri A, Chini G, Vivek A, et al (2015) Arbitrary Lagrangian-Eulerian finite element simulation and experimental investigation of wavy interfacial morphology during high velocity impact welding. Mater Des 88:345–358. https://doi.org/10.1016/j.matdes.2015.09.005

11. Baek J, Chen J-S, Zhou G, et al (2021) A semi-Lagrangian reproducing kernel particle method with particle-based shock algorithm for explosive welding simulation. Comput Mech 67:1601–1627. https://doi.org/10.1007/s00466-021-02008-2

12. Li XJ, Mo F, Wang XH, et al (2012) Numerical study on mechanism of explosive welding. Sci Technol Weld Join 17:36–41. https://doi.org/10.1179/1362171811Y.0000000071

13. Nassiri A, Vivek A, Abke T, et al (2017) Depiction of interfacial morphology in impact welded Ti/Cu bimetallic systems using smoothed particle hydrodynamics. Appl Phys Lett 110:. https://doi.org/10.1063/1.4984742

14. Liu MB, Zhang ZL, Feng DL (2017) A density-adaptive SPH method with kernel gradient correction for modeling explosive welding. Comput Mech 60:513–529. https://doi.org/10.1007/s00466-017-1420-5

15. Bataev IA, Tanaka S, Zhou Q, et al (2019) Towards better understanding of explosive welding by combination of numerical simulation and experimental study. Mater Des 169:. https://doi.org/10.1016/j.matdes.2019.107649

16. Chen JS, Wu Y (2007) Stability in Lagrangian and Semi-Lagrangian reproducing kernel discretizations using nodal integration in nonlinear solid mechanics. In: Leitão VMA, Alves CJS, Armando Duarte C (eds) Advances in Meshfree Techniques. Computational Methods in Applied Sciences, vol 5. Springer, Dordrecht, pp 55–76

17. Guan PC, Chen JS, Wu Y, et al (2009) Semi-Lagrangian reproducing kernel formulation and application to modeling earth moving operations. Mech Mater 41:670–683. https://doi.org/10.1016/j.mechmat.2009.01.030

18. Guan PC, Chi SW, Chen JS, et al (2011) Semi-Lagrangian reproducing kernel particle method for fragment-impact problems. Int J Impact Eng 38:1033–1047. https://doi.org/10.1016/j.ijimpeng.2011.08.001

19. Acarer M, Gülenç B, Findik F (2003) Investigation of explosive welding parameters and their effects on microhardness and shear strength. Mater Des 24:659–664. https://doi.org/10.1016/S0261-3069(03)00066-9

20. Kim K, Watanabe M, Kawakita J, Kuroda S (2008) Grain refinement in a single titanium powder particle impacted at high velocity. Scr Mater 59:768–771. https://doi.org/https://doi.org/10.1016/j.scriptamat.2008.06.020

21. Rokni MR, Nutt SR, Widener CA, et al (2017) Review of Relationship Between Particle Deformation, Coating Microstructure, and Properties in High-Pressure Cold Spray. J Therm Spray Technol 26:1308–1355. https://doi.org/10.1007/s11666-017-0575-0

22. Chu Q, Zhang M, Li J, Yan C (2017) Experimental and numerical investigation of microstructure and mechanical behavior of titanium/steel interfaces prepared by explosive welding. Mater Sci Eng A 689:323–331. https://doi.org/10.1016/j.msea.2017.02.075

23. Walker M (2018) Microstructure and bonding mechanisms in cold spray coatings. Mater Sci Technol (United Kingdom) 34:2057–2077. https://doi.org/10.1080/02670836.2018.1475444

24. Liu BC, Palazotto AN, Nassiri A, et al (2019) Experimental and numerical investigation of interfacial microstructure in fully age-hardened 15-5 PH stainless steel during impact welding. J Mater Sci 54:9824–9842. https://doi.org/10.1007/s10853-019-03546-0

25. Meyers MA, Nesterenko VF, LaSalvia JC, Xue Q (2001) Shear localization in dynamic deformation of materials: microstructural evolution and self-organization. Mater Sci Eng A 317:204–225. https://doi.org/https://doi.org/10.1016/S0921-5093(01)01160-1

26. Meyers MA, Xu YB, Xue Q, et al (2003) Microstructural evolution in adiabatic shear localization in stainless steel. Acta Mater 51:1307–1325. https://doi.org/10.1016/S1359-6454(02)00526-8

27. Zou Y, Qin W, Irissou E, et al (2009) Dynamic recrystallization in the particle/particle interfacial region of cold-sprayed nickel coating: Electron backscatter diffraction characterization. Scr Mater 61:899–902. https://doi.org/https://doi.org/10.1016/j.scriptamat.2009.07.020

28. Lee C, Kim J (2015) Microstructure of Kinetic Spray Coatings: A Review. J Therm Spray Technol 24:592–610. https://doi.org/10.1007/s11666-015-0223-5

29. Li Z, Wang B, Zhao S, et al (2017) Dynamic deformation and failure of ultra fine-grained titanium. Acta Mater 125:210–218. https://doi.org/10.1016/j.actamat.2016.11.041

30. Lins JFC, Sandim HRZ, Kestenbach HJ, et al (2007) A microstructural investigation of adiabatic shear bands in an interstitial free steel. Mater Sci Eng A 457:205–218. https://doi.org/10.1016/j.msea.2006.12.019

31. Gao H, Huang Y (2003) Geometrically necessary dislocation and size-dependent plasticity. Scr Mater 48:113–118. https://doi.org/https://doi.org/10.1016/S1359-6462(02)00329-9

32. Huang K, Logé RE (2016) A review of dynamic recrystallization phenomena in metallic materials. Mater Des 111:548–574. https://doi.org/https://doi.org/10.1016/j.matdes.2016.09.012

33. Gourdet S, Montheillet F (2000) An experimental study of the recrystallization mechanism during hot deformation of aluminium. Mater Sci Eng A 283:274–288. https://doi.org/https://doi.org/10.1016/S0921-5093(00)00733-4

34. Yanushkevich Z, Belyakov A, Kaibyshev R (2015) Microstructural evolution of a 304-type austenitic stainless steel during rolling at temperatures of 773–1273K. Acta Mater 82:244–254. https://doi.org/https://doi.org/10.1016/j.actamat.2014.09.023

35. Kelchner CL, Plimpton SJ, Hamilton JC (1998) Dislocation nucleation and defect structure during surface indentation. Phys Rev B 58:11085–11088. https://doi.org/10.1103/PhysRevB.58.11085

36. Yamakov V, Wolf D, Phillpot SR, Gleiter H (2002) Deformation twinning in nanocrystalline Al by molecular-dynamics simulation. Acta Mater 50:5005–5020. https://doi.org/https://doi.org/10.1016/S1359-6454(02)00318-X

37. Li J, Van Vliet KJ, Zhu T, et al (2002) Atomistic mechanisms governing elastic limit and incipient plasticity in crystals. Nature 418:307–310. https://doi.org/10.1038/nature00865

38. Zbib HM, Diaz de la Rubia T (2002) A multiscale model of plasticity. Int J Plast 18:1133–1163. https://doi.org/https://doi.org/10.1016/S0749-6419(01)00044-4

39. Bulatov V V, Hsiung LL, Tang M, et al (2006) Dislocation multi-junctions and strain hardening. Nature 440:1174–1178. https://doi.org/10.1038/nature04658

40. McDowell DL (2008) Viscoplasticity of heterogeneous metallic materials. Mater Sci Eng R Reports 62:67–123. https://doi.org/https://doi.org/10.1016/j.mser.2008.04.003

41. Gurtin ME (2000) On the plasticity of single crystals: free energy, microforces, plastic-strain gradients. J Mech Phys Solids 48:989–1036. https://doi.org/https://doi.org/10.1016/S0022-5096(99)00059-9

42. Cermelli P, Gurtin ME (2001) On the characterization of geometrically necessary dislocations in finite plasticity. J Mech Phys Solids 49:1539–1568. https://doi.org/10.1016/S0022-5096(00)00084-3

43. Gurtin ME (2002) A gradient theory of single-crystal viscoplasticity that accounts for geometrically necessary dislocations. J Mech Phys Solids 50:5–32. https://doi.org/10.1016/S0022-5096(01)00104-1

44. Borg U (2007) Strain gradient crystal plasticity effects on flow localization. Int J Plast 23:1400–1416. https://doi.org/https://doi.org/10.1016/j.ijplas.2007.01.003

45. Yalcinkaya T, Brekelmans WAM, Geers MGD (2011) Deformation patterning driven by rate dependent non-convex strain gradient plasticity. J Mech Phys Solids 59:1–17. https://doi.org/https://doi.org/10.1016/j.jmps.2010.10.002

46. Forest S (1997) A cosserat theory for elastoviscoplastic single crystals at finite deformation.pdf. Arch Mech 49:705–736

47. Nye JF (1953) Some geometrical relations in dislocated crystals. Acta Metall 1:153–162. https://doi.org/https://doi.org/10.1016/0001-6160(53)90054-6

48. Kröner E (1963) On the physical reality of torque stresses in continuum mechanics. Int J Eng Sci 1:261–278. https://doi.org/https://doi.org/10.1016/0020-7225(63)90037-5

49. Forest S, Barbe F, Cailletaud G (2000) Cosserat modelling of size effects in the mechanical behaviour of polycrystals and multi-phase materials. Int J Solids Struct 37:7105–7126. https://doi.org/https://doi.org/10.1016/S0020-7683(99)00330-3

50. Mayeur JR, McDowell DL (2011) Bending of single crystal thin films modeled with micropolar crystal plasticity. Int J Eng Sci 49:1357–1366. https://doi.org/https://doi.org/10.1016/j.ijengsci.2011.05.018

51. Mayeur JR, McDowell DL (2014) A comparison of Gurtin type and micropolar theories of generalized single crystal plasticity. Int J Plast 57:29–51. https://doi.org/10.1016/j.ijplas.2014.01.010

52. Klusemann B, Yalçinkaya T (2013) Plastic deformation induced microstructure evolution through gradient enhanced crystal plasticity based on a non-convex Helmholtz energy. Int J Plast 48:168–188. https://doi.org/https://doi.org/10.1016/j.ijplas.2013.02.012

53. Forest S (1998) Modeling slip, kink and shear banding in classical and generalized single crystal plasticity. Acta Mater 46:3265–3281. https://doi.org/https://doi.org/10.1016/S1359-6454(98)00012-3

54. Hallberg H (2011) Approaches to Modeling of Recrystallization. Metals (Basel) 1:16–48. https://doi.org/10.3390/met1010016

55. Eiken J, Böttger B, Steinbach I (2006) Multiphase-field approach for multicomponent alloys with extrapolation scheme for numerical application. Phys Rev E - Stat Nonlinear, Soft Matter Phys 73:1–9. https://doi.org/10.1103/PhysRevE.73.066122

56. Takaki T, Hirouchi T, Hisakuni Y, et al (2008) Multi-phase-field model to simulate microstructure evolutions during dynamic recrystallization. Mater Trans 49:2559–2565. https://doi.org/10.2320/matertrans.MB200805

57. Kobayashi R, Giga Y (1999) Equations with singular diffusivity. J Stat Phys 95:1187–1220. https://doi.org/10.1023/a:1004570921372

58. Kobayashi R, Warren JA, Carter WC (2000) A continuum model of grain boundaries. Phys D Nonlinear Phenom 140:141–150. https://doi.org/10.1016/S0167-2789(00)00023-3

59. Zhang X, Chen J-S, Osher S (2008) A multiple level set method for modeling grain boundary evolution of polycrystalline materials. Interact multiscale Mech 1:178–191

60. Logé R, Bernacki M, Resk H, et al (2008) Linking plastic deformation to recrystallization in metals using digital microstructures. Philos Mag 88:3691–3712. https://doi.org/10.1080/14786430802502575

61. Hallberg H (2013) A modified level set approach to 2D modeling of dynamic recrystallization. Model Simul Mater Sci Eng 21:85012. https://doi.org/10.1088/0965-0393/21/8/085012

62. Blesgen T (2017) A variational model for dynamic recrystallization based on Cosserat plasticity. Compos Part B Eng 115:236–243. https://doi.org/https://doi.org/10.1016/j.compositesb.2016.10.005

63. Hesselbarth HW, Göbel IR (1991) Simulation of recrystallization by cellular automata. Acta Metall Mater 39:2135–2143. https://doi.org/https://doi.org/10.1016/0956-7151(91)90183-2

64. Raabe D, Becker RC (2000) Coupling of a crystal plasticity finite-element model with a probabilistic cellular automaton for simulating primary static recrystallization in aluminium. Model Simul Mater Sci Eng 8:445–462. https://doi.org/10.1088/0965-0393/8/4/304

65. Popova E, Staraselski Y, Brahme A, et al (2015) Coupled crystal plasticity – Probabilistic cellular automata approach to model dynamic recrystallization in magnesium alloys. Int J Plast 66:85–102. https://doi.org/https://doi.org/10.1016/j.ijplas.2014.04.008

66. Chen JS, Kotta V, Lu H, et al (2004) A variational formulation and a double-grid method for meso-scale modeling of stressed grain growth in polycrystalline materials. Comput Methods Appl Mech Eng 193:1277–1303.

https://doi.org/https://doi.org/10.1016/j.cma.2003.12.020

67. Chen J-S, Mehraeen S (2004) Variationally consistent multi-scale modeling and homogenization of stressed grain growth. Comput Methods Appl Mech Eng 193:1825–1848. https://doi.org/https://doi.org/10.1016/j.cma.2003.12.038

68. Ask A, Forest S, Appolaire B, et al (2018) A Cosserat crystal plasticity and phase field theory for grain boundary migration. J Mech Phys Solids 115:167–194. https://doi.org/10.1016/j.jmps.2018.03.006

69. Ask A, Forest S, Appolaire B, Ammar K (2019) A Cosserat–phase-field theory of crystal plasticity and grain boundary migration at finite deformation. Contin Mech Thermodyn 31:1109–1141. https://doi.org/10.1007/s00161-018-0727-6

70. Admal NC, Po G, Marian J (2018) A unified framework for polycrystal plasticity with grain boundary evolution. Int J Plast 106:1–30. https://doi.org/10.1016/j.ijplas.2018.01.014

71. Mikula J, Joshi SP, Tay T-E, et al (2019) A phase field model of grain boundary migration and grain rotation under elasto–plastic anisotropies. Int J Solids Struct 178–179:1–18. https://doi.org/https://doi.org/10.1016/j.ijsolstr.2019.06.014

72. Ask A, Forest S, Appolaire B, Ammar K (2020) Microstructure evolution in deformed polycrystals predicted by a diffuse interface Cosserat approach. Adv Model Simul Eng Sci 7:9. https://doi.org/10.1186/s40323-020-00146-5

73. Borst R de (2001) Some recent issues in computational failure mechanics. Int J Numer Methods Eng 52:63–95. https://doi.org/https://doi.org/10.1002/nme.272

74. P. BZ, Milan J (2002) Nonlocal Integral Formulations of Plasticity and Damage: Survey of Progress. J Eng Mech 128:1119–1149. https://doi.org/10.1061/(ASCE)0733-9399(2002)128:11(1119)

75. Mindlin RD (1965) Second gradient of strain and surface-tension in linear elasticity. Int J Solids Struct 1:417–438. https://doi.org/https://doi.org/10.1016/0020-7683(65)90006-5

76. Aifantis EC (1984) On the Microstructural Origin of Certain Inelastic Models. J Eng Mater Technol 106:326–330. https://doi.org/10.1115/1.3225725

77. De Borst R, Mühlhaus H-B (1992) Gradient-dependent plasticity: Formulation and algorithmic aspects. Int J Numer Methods Eng 35:521–539. https://doi.org/https://doi.org/10.1002/nme.1620350307

78. Chen J-S, Zhang X, Belytschko T (2004) An implicit gradient model by a reproducing

kernel strain regularization in strain localization problems. Comput Methods Appl Mech Eng 193:2827–2844. https://doi.org/https://doi.org/10.1016/j.cma.2003.12.057

79. Reedlunn B, Moutsanidis G, Baek J, et al (2020) Initial Simulations of Empty Room Collapse and Reconsolidation at the Waste Isolation Pilot Plant. In: 54th US Rock Mechanics/Geomechanics Symposium. American Rock Mechanics Association

80. Ambrosio L, Tortorelli VM (1990) Approximation of functional depending on jumps by elliptic functional via t-convergence. Commun Pure Appl Math 43:999–1036. https://doi.org/https://doi.org/10.1002/cpa.3160430805

81. Steinbach I (2009) Phase-field models in materials science. Model Simul Mater Sci Eng 17:73001. https://doi.org/10.1088/0965-0393/17/7/073001

82. He X, He Q, Chen J-S (2021) Deep autoencoders for physics-constrained data-driven nonlinear materials modeling. Comput Methods Appl Mech Eng 385:114034. https://doi.org/https://doi.org/10.1016/j.cma.2021.114034

83. He Q, Chen J-S (2020) A physics-constrained data-driven approach based on locally convex reconstruction for noisy database. Comput Methods Appl Mech Eng 363:112791. https://doi.org/https://doi.org/10.1016/j.cma.2019.112791

84. Lee K, Carlberg KT (2020) Model reduction of dynamical systems on nonlinear manifolds using deep convolutional autoencoders. J Comput Phys 404:108973. https://doi.org/https://doi.org/10.1016/j.jcp.2019.108973

85. Raissi M, Perdikaris P, Karniadakis GE (2019) Physics-informed neural networks: A deep learning framework for solving forward and inverse problems involving nonlinear partial differential equations. J Comput Phys 378:686–707. https://doi.org/10.1016/j.jcp.2018.10.045

86. Haghighat E, Juanes R (2021) SciANN: A Keras/TensorFlow wrapper for scientific computations and physics-informed deep learning using artificial neural networks. Comput Methods Appl Mech Eng 373:113552. https://doi.org/10.1016/j.cma.2020.113552

87. Samaniego E, Anitescu C, Goswami S, et al (2020) An energy approach to the solution of partial differential equations in computational mechanics via machine learning: Concepts, implementation and applications. Comput Methods Appl Mech Eng 362:112790. https://doi.org/10.1016/j.cma.2019.112790

88. Zhang L, Cheng L, Li H, et al (2021) Hierarchical deep-learning neural networks: finite elements and beyond. Comput Mech 67:207–230. https://doi.org/10.1007/s00466-020-01928-9

89. Lee K, Trask NA, Patel RG, et al (2021) Partition of unity networks: deep hp-approximation

90. Abrivard G, Busso EP, Forest S, Appolaire B (2012) Phase field modelling of grain boundary motion driven by curvature and stored energy gradients. Part I: theory and numerical implementation. Philos Mag 92:3618–3642. https://doi.org/10.1080/14786435.2012.713135

91. Geelen RJM, Liu Y, Hu T, et al (2019) A phase-field formulation for dynamic cohesive fracture. Comput Methods Appl Mech Eng 348:680–711. https://doi.org/https://doi.org/10.1016/j.cma.2019.01.026

92. Cailletaud G (1992) A micromechanical approach to inelastic behaviour of metals. Int J Plast 8:55–73. https://doi.org/https://doi.org/10.1016/0749-6419(92)90038-E

93. Ask A, Forest S, Appolaire B, Ammar K (2018) Cosserat crystal plasticity with dislocation-driven grain boundary migration. J Micromechanics Mol Phys 03:1840009. https://doi.org/10.1142/S242491301840009X

94. Lobkovsky AE, Warren JA (2001) Sharp interface limit of a phase-field model of crystal grains. Phys Rev E 63:51605. https://doi.org/10.1103/PhysRevE.63.051605

95. Lobkovsky AE, Warren JA (2001) Phase-field model of crystal grains. J Cryst Growth 225:282–288. https://doi.org/https://doi.org/10.1016/S0022-0248(01)00867-3

96. Wolf D (1990) Structure-energy correlation for grain boundaries in F.C.C. metals—III. Symmetrical tilt boundaries. Acta Metall Mater 38:781–790. https://doi.org/https://doi.org/10.1016/0956-7151(90)90030-K

97. Tschopp MA, Coleman SP, McDowell DL (2015) Symmetric and asymmetric tilt grain boundary structure and energy in Cu and Al (and transferability to other fcc metals). Integr Mater Manuf Innov 4:176–189. https://doi.org/10.1186/s40192-015-0040-1

98. Liu WK, Jun S, Zhang YF (1995) Reproducing kernel particle methods. Int J Numer methods fluids 20:1081–1106. https://doi.org/10.1002/fld.1650200824

99. Chen JS, Pan C, Wu C-T, Liu WK (1996) Reproducing Kernel Particle Methods for large deformation analysis of non-linear structures. Comput Methods Appl Mech Engrg 139:195–227. https://doi.org/10.1016/S0045-7825(96)01083-3

100. Bochev PB, Dohrmann CR, Gunzburger MD (2006) Stabilization of Low-order Mixed Finite Elements for the Stokes Equations. SIAM J Numer Anal 44:82–101. https://doi.org/10.1137/S0036142905444482

101. Miehe C, Welschinger F, Hofacker M (2010) Thermodynamically consistent phase-field models of fracture: Variational principles and multi-field FE implementations. Int J Numer Methods Eng 83:1273–1311. https://doi.org/https://doi.org/10.1002/nme.2861

102. Borden MJ, Verhoosel C V, Scott MA, et al (2012) A phase-field description of dynamic brittle fracture. Comput Methods Appl Mech Eng 217–220:77–95. https://doi.org/https://doi.org/10.1016/j.cma.2012.01.008

103. Abrivard G, Busso EP, Forest S, Appolaire B (2012) Phase field modelling of grain boundary motion driven by curvature and stored energy gradients. Part II: Application to recrystallisation. Philos Mag 92:3643–3664. https://doi.org/10.1080/14786435.2012.717726

104. Chen JS, Wu CT, Yoon S (2001) A stabilized conforming nodal integration for Galerkin mesh-free methods. Int J Numer Meth Eng 0207:435–466. https://doi.org/10.1002/1097-0207(20010120)50

105. Chen JS, Yoon S, Wu CT (2002) Non-linear version of stabilized conforming nodal integration for Galerkin mesh-free methods. Int J Numer Methods Eng 53:2587–2615. https://doi.org/10.1002/nme.338

106. Chen JS, Hillman M, Rüter M (2013) An arbitrary order variationally consistent integration for Galerkin meshfree methods. Int J Numer Methods Eng 95:387–418. https://doi.org/10.1002/nme.4512

107. Kingma DP, Ba J (2015) Adam: A Method for Stochastic Optimization. BT - 3rd International Conference on Learning Representations, ICLR 2015, San Diego, CA, USA, May 7-9, 2015, Conference Track Proceedings

108. Miehe C, Hofacker M, Welschinger F (2010) A phase field model for rate-independent crack propagation: Robust algorithmic implementation based on operator splits. Comput Methods Appl Mech Eng 199:2765–2778. https://doi.org/https://doi.org/10.1016/j.cma.2010.04.011

109. Herring C (1951) Some Theorems on the Free Energies of Crystal Surfaces. Phys Rev 82:87–93. https://doi.org/10.1103/PhysRev.82.87

110. Le Hazif R, Dorizzi Et P, Poirier JP (1973) Glissement {110} 〈110〉 dans les metaux de structure cubique a faces centrees. Acta Metall 21:903–911. https://doi.org/https://doi.org/10.1016/0001-6160(73)90148-X

111. Gourdet S (1997) Étude des mécanismes de recristallisation au cours de la déformation a chaud de l'aluminium. Ecole Nationale Supérieure des Mines de Saint-Etienne

112. Hull D, Bacon DJ (2011) Chapter 1 - Defects in Crystals. In: Hull D, Bacon DJBT-I to D (Fifth E (eds) Introduction to Dislocations. 5th ed. Butterworth-Heinemann, Oxford, pp 1–20